GROWTH AND OPTIMIZATION OF PIEZOELECTRIC SINGLE CRYSTAL TRANSDUCERS FOR ENERGY HARVESTING FROM ACOUSTIC SOURCES

By

ROMIT DHAR

A dissertation submitted in partial fulfillment of
the requirements for the degree of

DOCTOR OF PHILOSOPHY

WASHINGTON STATE UNIVERSITY
School of Mechanical and Materials Engineering

MAY 2009

To the Faculty of Washington State University:

The members of the Committee appointed to examine the dissertation of ROMIT DHAR find it satisfactory and recommend that it be accepted.

_____

Dr. Kelvin G. Lynn, PhD., Chair

_____

Dr. David F. Bahr, PhD.

_____

Dr. Konstantin Matveev, Ph.D.

_____

Dr. Philip L. Marston, PhD.

ACKNOWLEDGEMENT

I express my deepest gratitude to Dr. Kelvin G. Lynn for providing direction, advice and encouragement for this research. I thank him for sharing his knowledge on various subjects during the course of this work. I would like to thank Dr. David F. Bahr, Dr. Philip L. Marston and Dr. Konstantin Matveev, my committee members for their suggestions. I would also like to thank Dr. Leon J. Radziemski and Mr. Bill Andre for providing insight on various issues during the course of this research.

I am grateful to all the people at Center for Materials Research at WSU for their contribution during my research. I would especially like to thank Russell Tjossem for sharing his knowledge and views. I would also like to thank Kelly Jones, Llyod Pilant, Diego Rodriguez, Lenny Swanson, Matthew Thurber, Russell Follet, Robert Peterson and Alys Hugo for helping me with different experiments. I would also like to thank Rebecca Griswold, Roger Saunders and office staff for their help and support.

I would like to thank my parents and sister, and without their support I couldn't have accomplished whatever I have. I have missed them dearly, while staying away from home all these years. Lastly, I would like to thank all my friends here in Pullman, especially Jagan Padbidri and Sreekanth Akarapu, who really made my stay enjoyable and worthwhile.

I would like to thank the sponsors, Department of Energy for the Thermo-acoustic Piezoelectric Energy Conversion project (Grant No. BAA W9113M-05-0009) and the Space Missile Defense Command P3 Power Generation project (Grant No.

DASG60020084) for supporting research presented in this work. I also acknowledge II-VI Inc. and Piezo Partners Inc. for their background in the HPB growth technology.

GROWTH AND OPTIMIZATION OF PIEZOELECTRIC SINGLE CRYSTAL TRANSDUCERS FOR ENERGY HARVESTING FROM ACOUSTIC SOURCES

Abstract

by Romit Dhar, Ph.D.
Washington State University
May 2009

Chair: Kelvin G. Lynn

Low power requirements of modern sensors and electronics have led to the examination of the feasibility of several energy harvesting schemes. This thesis describes the fabrication and performance of an acoustic energy harvester with single crystal piezoelectric unimorph. The unimorphs were fabricated from single crystal relaxor ferroelectric *(1-x)*PMN - *x*PT grown with $x = 0.3$ and 0.32 as the starting composition. It is demonstrated that significant power can be harvested using unimorph structures from an acoustic field at resonance. Passive circuit components were used for output circuit with a resistive load in series with a tunable inductor. A tuning capacitor connected in parallel to the device further increased the power output by matching the impedance of the unimorph. The power harvested can be either used directly for running low-power devices or can be stored in a rechargeable battery. A comparison of the performance of PMN-PT and PZT unimorphs at the resonance of the coupled structure under identical excitation conditions was done. For a certain optimized thickness ratio and circuit parameters, the single crystal PMN-PT unimorph generated 30 mW of power while a PZT unimorph generated 7.5 mW at resonance and room temperature. The harvested

output power from the single crystal PMN-PT unimorphs depends on several material properties, physical and ambient parameters and an effort has been made to study their effect on the performance.

A self-seeding high pressure Bridgman (HPB) technique was used to grow the PMN-PT single crystal ingots in a cost-effective way in our laboratories. Several techniques of material processing were developed to fabricate the PMN-PT single crystal unimorphs from as grown bulk ingots. This growth technique produced good quality single crystals for our experiments, with a $k_{33} = 0.91$ for a <001> oriented bar.

TABLE OF CONTENTS

CHAPTERS

LIST OF TABLES

Table

LIST OF FIGURES

Figure

Dedication

Dedicated to my parents B.C. Dhar and Chinu Dhar, my sister Romila Dhar

and

Esha Adhya

CHAPTER – 1

INTRODUCTION

1.1 Background

The process of extracting unused energy from the ambient environment and converting it into a usable form of electrical energy is known as *Energy Harvesting*. Energy harvesters using piezoelectric materials are not a new concept and their generation capability for creating a steady and reliable source of energy is the current focus of research. They can be incorporated into low power portable devices (typically of the order of 10 - 100 mW) as a battery-less power supply. For portable electronics, use of chemical batteries is problematic and requires constant monitoring as the electronics could cease at any time. The problem intensifies in the case of wireless sensors as they can be remotely located and replacement of the battery can be troublesome. Hence, there is an urge of reclaiming power from various sources, e.g. heat, acoustic and mechanical vibrations, and converting it into useful electrical power. The current trends in technology have led to a decrease in both size and power consumption of digital electronic systems and integrated circuits and thus have made energy harvesting an attractive prospect.

In the past, researchers have surveyed several ambient sources for energy reclamation and converting into usable electrical energy [1, 2]. The choice of the source depends primarily on the specification of the power requirement for an application and design feasibility [3, 4]. The common sources for energy harvesting systems are:

1) Solar Energy – Light captured through solar panels, photo diodes etc.
2) Mechanical Energy – Stress and strain generated from various sources of vibration, both natural and industrial.

3) Thermal Energy – Waste heat from furnaces, industrial equipments and exhausts.

4) Human Body – Thermal energy from body metabolism, mechanical energy from ambulatory motion and other activities.

5) Acoustic Energy – Industrial noise, monochromatic sound sources and thermo-acoustic converters.

6) Other forms of Energy – Wind, water flow, ocean waves and biological.

The above choice of energy sources when coupled with various transducer technologies can lead to a whole gamut of energy harvesting schemes. The feasibility of these schemes poses all sorts of design and implementation challenges based on the application need. The energy scavenging scheme of choice is decided based on the overall energy audit, i.e. the efficiency. The block diagram shown in Figure 1.1 lists the several technologies for energy harvesting schemes.

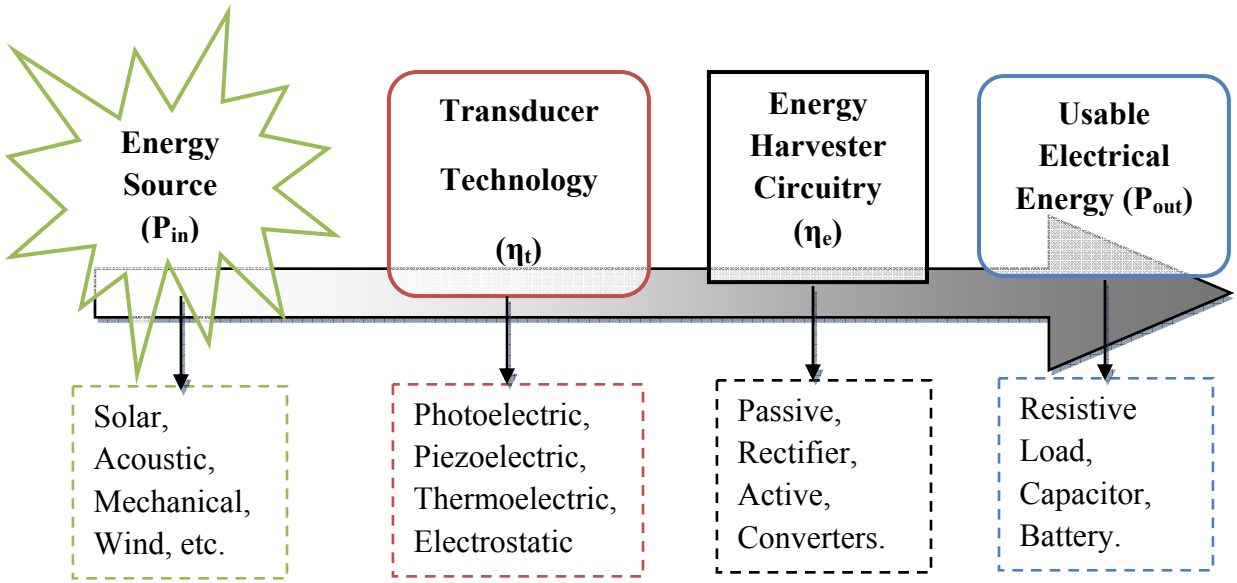

Figure 1.1: Energy harvesting block diagram

Based on the application, the overall efficiency (η) of energy harvesting is the ratio of output power (P_{out}) realized at the load to the input power (P_{in}) from the source. It depends on two broad parameters. They are: 1) the transducer efficiency (η_t) and 2) the power conversion efficiency (η_e). The transducer efficiency depends on the coupling of the medium from which energy is harnessed to the transducer. The power conversion efficiency depends on the circuitry involved for supplying power to the electrical end load.

$$\eta = \frac{P_{out}}{P_{in}} \tag{1.1}$$

$$\eta = \eta_t * \eta_e \tag{1.2}$$

1.2 Energy Harvesting – Literature Review

1.2.1 Energy Sources

Generally, all of the energy harvesting sources discussed above has advantages and disadvantages. The disadvantages could be mainly due to the limitations of energy density of the source or effective transducer efficiency. Table 1.1 below lists the energy density of the source based on certain specific conditions [7 - 12]. The oldest technology is solar energy harvesting by solar cells but the solar insolation is dependent on geography and time of day. It has been also seen that solar energy harvesting has a 50% better performance for stationary mounted panels rather than mobile panels [5]. Vibrations from large industrial machines, buildings and automobile motion can provide ample power for powering remote sensors. Gonzalez et al. also discussed a few portable applications and the power requirements for each device [6]. The power required for communication devices such as Bluetooth and GSM range typically between 12–18

mW. Low frequency acoustic noise has a very low power density distributed over a broad spectrum of frequency while monochromatic sound source at a given frequency can achieve much higher power densities and can be used for energy harvesting effectively.

Table 1.1 Comparisons of Power Densities of Various Sources for Energy Harvesting

Energy Source	**Power Density**	**Comments**
Solar Energy – Outdoors	10 mW/cm^2 to 15 mW/cm^2	Varies with geographic position, Time of day, Incidence angle and environmental factors [9, 10]
Solar Energy – Indoors	0.01 mW/cm^2	Varies with indoor lighting and distance from source.
Thermoelectric	0.015 mW/cm^3 from 10 ºC ΔT	Seebeck effect on 10 ºC temperature differential [9]
Thermo Life® Energy Corp	0.035 mW/cm^3 from 5 ºC ΔT	Small temperature difference, body or waste heat, series of thermocouples [12]
Vibrations	0.116 mW/cm^3	Microwave oven, [11].
	0.2 mW/cm^3	Steel head ($8m/s^2$ at 50 Hz), [7].
Acoustic Noise	0.00096 mW/cm^3	Low frequency noise at 100 dB, [8]
Acoustic Monochromatic (plane-wave tube)	200 mW/cm^2	147 dB, 1 kHz and 100 cm from source
	0.2 mW/cm^2	117 dB, 1 kHz and 100 cm from source

1.2.2 Transducer Technologies

The transducer is the key component of the energy harvesting technology as it converts the available energy from ambient sources into electrical energy. Lot of research is being done in developing new and improving existing transducer technologies. It should be noted that not all of the transducers are suitable candidates for energy harvesting application based on the effective coupling with source excitation and their corresponding response.

1) Mechanical transduction
    a. Piezoelectric effect
    b. Electrostatic effect
    c. Piezoresistive effect
2) Thermal transduction
    a. Seebeck effect
    b. Pyroelectric effect
3) Magnetic transduction
    a. Hall effect
    b. Magnetostrictive effect
4) Radiation
    a. Photovoltaic effect
    b. Photoconductive effect

The most mature and stable technology is the use of photovoltaic cells for harvesting solar energy. The variation of ambient solar intensity based on time and location, however, makes it unreliable as a constant source of power to a device. The other most promising

technology for energy harvesting lies in the use of piezoelectric transducers which are commonly used for conversion of mechanical energy into electrical energy. Table 1.2 lists a brief summary of technologies used for energy harvesting applications and their approximate efficiencies.

Table 1.2 Transducer Technologies Available for Energy Harvesting [2, 4, 13 - 15]

Transducer Type	**Excitation Source**	**Materials**	**Efficiency (%)**	**Attributes**
Photovoltaic Cells (PV)	Solar / Visible spectrum (Outdoor / Indoor)	Crystalline Silicon	10% - 20%	- High cost of materials - Low light absorptivity of silicon - Low power density
		GaAs	25% - 30%	
		Amorphous Silicon / CdTe	5% - 9%	
		$CuInSe_2$	~ 17%	
Thermoelectric	Temperature Gradient (Waste Heat)	Doped Bi_2Te_3 (both p and n doped), Pb_2Te_3, Si-Ge, $YbAl_3$	Less than 5%	- Limited by Carnot efficiency and operating temperature - Material selection based on operating temperature
Electrostatic	Vibrations	MEMS scale Capacitor	~ 13.33 % (5.6 μW)	- Active system requiring capacitor excitation voltage
Piezoelectric	Vibrations, Pressure variations	Ceramics, Single crystals, Polymer	~ 5 - 30%	- Depends on source excitation - Piezoelectric material property

1.2.3 Piezoelectric Energy Harvesting

Energy harvesting from piezoelectric materials has been investigated for a wide range of applications. The source of vibration and the choice of piezoelectric material used have varied depending on the nature of application and availability of the material. Several experimental setups have been studied with different excitation in order to increase the efficiency and the power density of the energy harvesting systems. Different types of piezoelectric materials have also been used as the transducer and it has a major influence on the performance of the device. Table 1.3 summarizes some energy harvesting experiments and the power densities achieved. The different source frequencies are also listed with the excitation source for the energy harvesting experiments.

Nearly two decades ago, Hauser et al. generated about 17 μW using a Polyvinylidene Fluoride (PVDF) film [16]. The source of vibration was the expansion and contraction of lungs of a mongrel dog and the energy harvester was placed inside the dog. This sparked a lot of interest in parasitic energy harvesting from human activities and motion. Kymisis et al. demonstrated they can harvest energy lost during walking using a combination of PVDF laminate structure and a Thunder actuator, pre-stressed Lead Zirconium Titanate (PZT) composite in a shoe [17]. The average power generated with PVDF was 1.1 mW and with PZT it was 1.2 mW with the inserts placed in the heel and the sole of a shoe.

Umeda et al. used the kinetic energy of a steel ball impacting against a thick PZT film to produce power and store it in a capacitor [18]. The steel ball was initially 5*mm* above a bronze disk (27*mm* in diameter and 0.*25mm* thick). The ball struck the center of the disk producing a bending vibration and bounced on the disk till it came to rest. The piezo patch converted the kinetic energy of the bouncing ball to electrical energy and stored a voltage in a capacitor. They

also found that the efficiency of energy harvested can be increased by reducing the effective capacitance of the system.

Sodano et al. demonstrated harvesting energy with a PZT cantilever beam when attached to an automobile compressor as the source of vibration [19, 20]. The 60 x 63 mm PZT patch bonded to aluminum plate was able to charge a 40 mA-h rechargeable battery in one hour. The vibration of a car compressor was also modeled as a chirp signal from 0 – 250 Hz. Roundy et al. also studied low level vibrations and realized about 1 mW/cm^3 power density using a PZT patch structure [8]. Several other researchers have used MEMS based PZT cantilever structures to harvest energy from random and periodic vibrating sources [21, 22].

Circular unimorph structures have also been used to harvest energy in a transverse mode of excitation and can be more efficient than cantilever structures. Ericka et al. used a PZT on brass unimorph and generated 1.8 mW with 2g acceleration from a periodic shaker [23]. Kashyap et al. also fabricated an acoustic energy harvester of a PZT unimorph coupled to the backplate of a Helmholtz resonator [24]. The 2.5 x 2.5 cm^2 square PZT membranes produced 7.4 mW with 157 dB SPL acoustic excitation at 2.18 kHz. All of these methods used mostly PZT, a readily available and less expensive piezo-ceramic, as the piezoelectric transducer material. The piezoelectric PZT layer has been bonded to either brass or stainless steel substrates as the non-piezoelectric layer for fabrication of the devices.

Table 1.3: Review of Piezoelectric Energy Harvesting

Author	Piezoelectric Material	Excitation Source	Excitation Condition	Power Harvested	Power Density
Hausler et al. [16]	PVDF	Motion of Lungs (0.25 Hz)	~ 24 kPa	17 μW	0.236 mW/cc
Kymisis et al. [17]	PVDF laminate	Human walk motion (1 Hz)	0.11 - 0.15 MPa	1.1 mW	0.377 mW/cc
Kymisis et al. [17]	PZT unimorph Thunder 6 ™	Human walk motion (1 Hz)	0.11 - 0.15 MPa	1.8 mW	1.889 mW/cc
Shenck et al. [26]	PZT bimorph Thunder 6 ™	Human walk motion (0.9 – 1.0 Hz)	0.11 - 0.15 MPa	8.4 mW	4.409 mW/cc
Kashyap et al. [24]	PZT unimorph	Acoustic resonator at (2.18 kHz)	157 dB (≡ 1.415 kPa)	7.4 mW	118.4 mW/cc
Roundy et al. [8]	PZT patch	Vibration in car tire (10 – 200Hz)	~ 5g acceleration	80 μW	1 mW/cc
Ottman et al. [25]	PZT patch	Mechanical shaker (54 Hz)	Not mentioned	30.66 mW	78.9 mW/cc
Ericka et al. [23]	PZT unimorph	Shaker (2.58 kHz)	2g acceleration	1.8 mW	50.08 mW/cc
Moon et al. [27]	PMN-PT single crystal	Shaker (190 Hz)	50 μm Tip displacement	65 μW	54.17 mW/cc
Ren et al. [28]	PMN-PT and Epoxy composite	Compression Test machine (4-10 Hz)	88 MPa Compressive force		96.2 mW/cc

Moon et al, for the first time used a cantilever beam with Lead Magnesium Niobate – Lead Titanate (PMN-PT) single crystal for energy harvesting [27]. PMN-PT is a novel piezoelectric single crystal with better piezoelectric properties and higher strain to voltage conversion than conventional piezo-ceramics. It will be discussed in further detail in Chapter 2. Their prototype PMN-PT single crystal harvester 10 mm x 1.2 mm x 0.1mm produced about 65 μW from a displacement of 50 μm at 190 Hz. Ren et al. prepared a multilayer PMN-PT single crystal and epoxy composite and a volume fraction close to 50 % of PMN-PT generated 96 mW/cc with 88 MPa of axial stress [28]. The samples were stressed in a longitudinal excitation mode. A major focus of ongoing research is investigating the use of excellent piezoelectric properties of PMN-PT in different coupling modes for energy harvesting applications.

Recent theoretical studies by Clark et al. provided a fair comparison of the performance of PZT and PMN-PT unimorphs under similar low frequency excitation [29]. It was shown the power output was a proportional to the deflection under applied stress. Although many researchers over the last two decades have used PZT as the primary material for energy harvesting, a novel material like single crystal PMN-PT holds much promise for future.

1.3 Motivation: Energy harvesting with PMN-PT

Larger piezoelectric response and better electromechanical coupling of the PMN-PT single crystals than conventional PZT ceramics have resulted in improved sensitivity, broader bandwidth and higher source levels in transducers. At present, PMN-PT single crystals is being used for manufacturing ultrasound transducers for most medical and industrial applications. The 3-5 times improvement in bandwidth led to the development of better ultrasound transducer heads with multiple transmit and receive channels for enhanced images [30, 31]. In the medical

ultrasound imaging industry, use of PMN-PT resulted in higher resolution image and colored flow images enabling early and better diagnosis for patients.

We hypothesize that the use of PMN-PT single crystals as a choice of piezoelectric medium will enhance the power generation for energy harvesting. The study of PMN-PT for energy harvesting has been limited primarily due to the availability of good crystals and to the limited knowledge of the property dependence on performance. The use of PMN-PT single crystals for an application is dependent on its composition and crystallographic orientation. Hence, the optimum composition and material properties needs to be investigated for maximizing power generation for energy harvesting.

Moreover, for an acoustic excitation and resonant mode operation, a high sound pressure level (SPL) at a single frequency is desired. Symko et al. developed and demonstrated thermo-acoustic engine prototypes which were capable of generating high sound pressure levels at a narrow-band frequency [32, 33]. The quality factor, Q, of these engines which produced sound from a temperature difference across a heat exchanger is comparable to that of the single crystal piezoelectric at lower frequencies and hence both could be coupled to a single operating resonance frequency. The sound source when coupled with the unimorph will operate at the transverse resonant mode of the piezoelectric device. This combined with an efficient passive circuit on the output of energy harvesting system can be used directly to run low power devices or store energy in a capacitor.

In this study, effort was made to successfully grow single crystal PMN-PT ingots by high pressure Bridgman technique and develop techniques for fabrication of PMN-PT unimorph devices for energy harvesting. The resonant frequency and output electrical circuitry was also

investigated to maximize energy output from the piezoelectric element. The scope of this work is summarized below:

- Optimization of PMN-PT single crystal unimorph fabrication. The relation of different electro-mechanical properties of these anisotropic crystals towards performance was investigated for the transducer fabrication.
- Investigating the coupling of PMN-PT unimorph with acoustic resonator cavity for maximizing power output at resonance.
- Tuning for optimal power transfer from the piezoelectric element by impedance matching of the output of piezoelectric device using passive circuit components.
- Determining the effect of various parameters that affect the performance of single crystal PMN-PT unimorphs in transverse mode of operation.
- Investigation and growth of PMN-PT using a self-seeding high pressure Bridgman technique at different starting compositions for producing good quality single crystals.

Chapter 2 presents a brief description of piezoelectric theory including the single crystal piezoelectric class of materials and the PMN-PT material system. Chapter 3 presents the single crystal PMN-PT transducer fabrication and its characterization via dielectric and impedance studies. Chapter 4 presents the experimental setup and energy harvesting results from an acoustic source. Chapter 5 discusses the several optimization parameters and their effect on the performance of the PMN-PT based power generation. The growth of the single crystal PMN-PT material is presented in Chapter 6. Composition variation and other attributes of the growth technique are also discussed briefly.

References:

[1] Glynne-Jones P. and White N.M., "Self-powered systems: A review of energy systems", Sensor Review, 21 (2), 2001, pp. 91-97.

[2] Paradiso J.A. and Starner T., "Energy scavenging for mobile and wireless electronics", IEEE Pervasive Computing, 4, 2005, pp. 18-27.

[3] Roundy S., Steingart D., Frechette L., Wright P. and Rabaey J., "Power sources for wireless sensor networks", 1st European Workshop on Wireless Sensor Networks, Jan. 19 – 21, 2004, Berlin, pp. 1-17.

[4] Mateu L. and Moll F., "Review of Energy Harvesting Techniques and Applications for microelectronics", Proceedings of SPIE, Vol. 5837, 2005, pp. 359-373.

[5] Veefkind M., "Industrial design and PV-power, challenges and barriers", ISES Solar World congress proceedings, June 14 – 19, 2003, Gotthenberg.

[6] Gonzalez J.L., Rubio A. and Moll F., "Human powered piezoelectric batteries to supply power of wearables electronic devices", International Journal of Society for Materials Engineering Resources, 10(1), 2002, pp. 34–40.

[7] Roundy S.J., Wright P.K. and Pister K.S.J., "Micro-Electrostatic Vibration-to-Electricity Converters", 2002 ASME IMECE, Nov. 17-22, 2002, New Orleans, Louisiana

[8] Roundy S.J. and Wright P.K., "A Piezoelectric Vibration Based Generator for Wireless Electronics", Smart Materials and Structures, 13, 2004, pp. 1131–1142.

[9] Roundy S.J., "Energy Scavenging for Wireless Sensor Nodes with a Focus on Vibration to Electricity Conversion", Ph.D. Dissertation, Department of Mechanical Engineering, 2003, University of California, Berkeley.

[10] Reinders A., "Options for Photovoltaic Solar Energy Systems in Portable Products", Proceedings of TMCE, Fourth International symposium April 22-26, 2002, Wuhan, P.R. China.

[11] Raghunathan V., Kansal A., Hsu J., Friedman J. and Srivastava M.B., "Design Considerations for Solar Energy Harvesting Wireless Embedded Systems", IEEE International Conference on Information Processing in Sensor Networks (IPSN), 2005, Los Angeles, California, USA.

[12] Stark I., "Thermal Energy Harvesting with Thermo Life® ", Proceedings of the International Workshop on Wearable and Implantable Body Sensor Networks, April 3-5, 2006, Cambridge, Massachusetts, USA.

[13] Weber E.R., "Efficiency Improvement of Crystalline Solar Cells", Technical Report – NREL/SR-520-37578, February 2005.

[14] Keith F. and Goswami D.Y., "Handbook of Energy Efficiency and Renewable Energy", CRC Press, 2007.

[15] Meninger S., Mur-Miranda J.O., Amirtharajah R., Chandrakasan A.P. and Lang J.H., "Vibration-to-Electric energy conversion", IEEE Transactions on Very Large Scale Integration (VLSI) Systems, 9(1), 2001, pp. 64-76.

[16] Hausler E. and Stein E., "Implantable Physiological Power Supply with PVDF Film", Ferroelectrics, 60, 1984, pp. 277–282.

[17] Kymissis J., Kendall C., Paradiso J. and Gershenfeld N., "Parasitic Power Harvesting in Shoes", Proceedings of 2nd IEEE International Symposium on Wearable Computers, October 19–20th, 1998, Pittsburg, PA, pp. 132–139.

[18] Umeda M., Nakamura K. and Ueha S., “Analysis of Transformation of Mechanical Impact Energy to Electrical Energy Using a Piezoelectric Vibrator”, Japanese Journal of Applied Physics, 35, 1996, pp. 3267–3273.

[19] Sodano H.A., Inman D.J. and Park G., “Comparison of Piezoelectric Energy Harvesting Devices for Recharging Batteries”, Journal of Intelligent Material Systems and Structures, 16, 2005, pp. 799–807.

[20] Sodano H.A., Park G. and Inman D.J., “Estimation of Electric Charge Output for Piezoelectric Energy Harvesting”, Strain, 40, 2004, pp. 49–58.

[21] Sohn J.W., Choi S.B. and Lee D.Y., “An Investigation on Piezoelectric Energy Harvesting for MEMS Power Sources”, Proceedings of the Institution of Mechanical Engineers, Part C—Journal of Mechanical Engineering Science, 219, 2005, pp. 429–436.

[22] Cho J.H., Raupp J.C., Hayenga P.D., Richards R.F., Bahr D.F., Richards C.D. and Anderson M.J., “Efficiency Characterization of Piezoelectrics for Power”, Proceedings of IMECE, November 13-20, 2004, Anaheim, California USA.

[23] Ericka M., Vasic D., Costa F., Poulin G. and Tliba S., “Energy harvesting from vibration using a piezoelectric membrane”, Journal de Physique IV France, 128, 2005, pp. 187–193.

[24] Horowitz S., Kashyap K.A., Liu F., Johnson D., Nishida T., Ngo K., Sheplak M. and Cattafesta L., “Technology Development for Self-Powered Sensors”, Proceedings of 1st Flow Control Conference, AIAA-2022-2702, 2002.

[25] Ottman G.K., Hofmann H.F., Bhatt A.C. and Lesieutre G.A., “Adaptive Piezoelectric Energy Harvesting Circuit for Wireless Remote Power Supply”, IEEE Transactions on Power Electronics, 17 (5), 2002, pp. 669-676.

[26] Shenck N.S. and Paradiso J.A., "Energy Scavenging with Shoe-Mounted Piezoelectrics", IEEE Micro, 21 (3), 2001, pp. 30-42.

[27] Hong Y.K. and Moon K.S., "Single Crystal Piezoelectric Transducers to Harvest Vibration Energy", Proceedings of SPIE, 6048, 2005, pp. E.1–E.7.

[28] Ren K., Liu Y., Geng X., Hofmann H.F. and Zhang Q.M., "Single Crystal PMN-PT/Epoxy 1-3 Composite for Energy-Harvesting Application", IEEE Transactions on Ultrasonics, Ferroelectrics, and Frequency control, 53 (3), 2006, pp. 631-638.

[29] Mo C., Radziemski L.J. and Clark W.W., "Analysis of PMN-PT and PZT circular diaphragm energy harvesters for use in implantable medical devices", Proceedings of SPIE, 6525, 2007, pp. 652507-1:9.

[30] Chen J. and Panda R., "Review: Commercialization of Piezoelectric Single Crystals for Medical Imaging Applications", Proceedings of the IEEE Ultrasonics Symposium, 2005, pp. 235 – 240.

[31] Rehrig P.W., Hackenberger W.S., Jiang X., Shrout T.R., Zhang S. and Speyer R., "Status of Piezoelectric Single Crystal Growth for Medical Transducer Applications", Proceedings of IEEE Ultrasonics Symposium, 1, 2003, pp. 766-769.

[32] Symko O., Abdel-Rahman E., Kwon Y. and Behunin R., "Design & Development of High-Frequency Thermoacoustic Engines for Thermal Management in Microelectronics", Microelectronics Journal, 35, 2004, pp. 185-191.

[33] A sound way to turn heat to electricity, www.physorg.com/pdf100141616.pdf**.**

CHAPTER – 2

PIEZOELECTRIC SINGLE CRYSTALS

2.1 Piezoelectric Theory

The *piezoelectric effect* was discovered by Jacques and Pierre Curie in 1880 in Rochelle salt. It was observed that if certain materials were subjected to mechanical strain they became electrically polarized while the degree of polarization was proportional to the applied strain, also known as direct piezoelectric effect. They also showed deformation when subjected to an external electric field, known as the inverse piezoelectric effect**.** Piezoelectric phenomena has been extensively utilized in the fabrication of various devices such as transducers, actuators, surface acoustic wave devices, frequency control, etc. [1, 2]. Applied stresses (tensile or compressive) results in a displacement of existing dipoles and create a net polarization, P, within the crystal. The polarization and amount of electric charge varies with the magnitude of applied stress and compressive and tensile stresses generate electric fields and voltages of opposite polarity across the crystals, as shown in Figure 2.1.

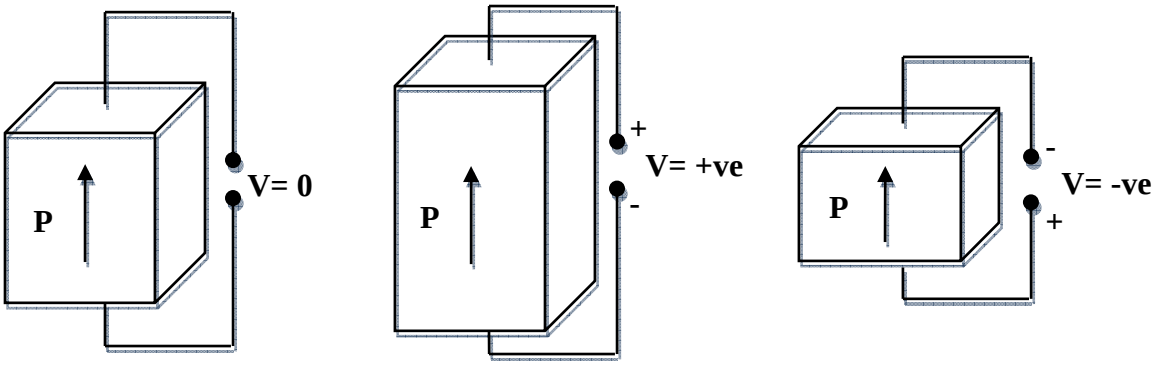

No Stress Tensile Stress Compressive Stress

Figure 2.1: Voltage (V) due to tensile and compressive stress on piezoelectric material

The piezoelectric effect is exhibited by a wide range of materials. These include naturally occurring minerals, polymers, ceramics and single crystals. Table 2.1 lists some examples of different types of piezoelectric materials commonly used.

Table 2.1: Examples of Common Piezoelectric Materials

Single Crystals	**Ceramics**	**Polymers**	**Naturally occurring**
- Quartz	- $BaTiO_3$	- PVDF	- Rochelle salt
- PMN-PT	- PZT	- PTFE	- Human bone/HAP
- PZN-PT	- $PbTiO_3$		- Cane sugar
- ZnO	- PLZT		

The piezoelectric effect can be expressed by the following electro-mechanical constitutive equations:

$$D = d.T + \varepsilon^T.E \qquad \text{(Direct effect)} \qquad (2.1)$$

$$S = s^E.T + d.E \qquad \text{(Inverse effect)} \qquad (2.2)$$

where, D is the dielectric displacement or polarization, T is stress, E is electric field, S is mechanical strain, d is piezoelectric coefficient, ε is dielectric constant and s is compliance. The superscripts indicate a constant quantity, i.e. s^E indicates compliance when electric field is kept constant. All these quantities have directional dependence and are represented as tensors of different degrees. The direction of positive polarization is usually chosen to coincide with the Z-axis of a rectangular system of crystallographic axes X, Y and Z. The directions of X, Y and Z are represented by 1, 2 and 3 respectively and the shear about these axes by 4, 5 and 6

respectively. The standard co-ordinate notation is shown in Figure 2.2 and they are used as subscripts to the above mentioned quantities.

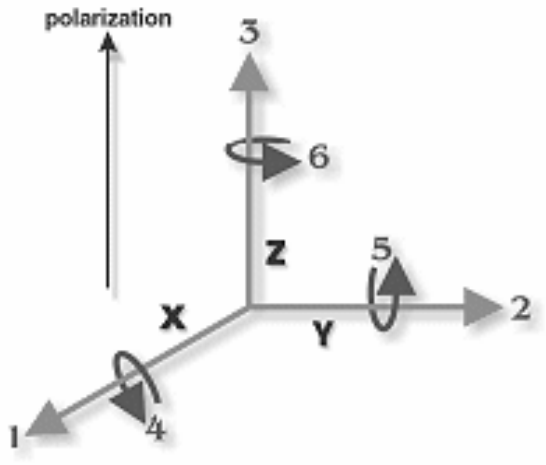

Figure 2.2: Standard co-ordinate notation (Adapted from APC International Ltd. [2])

The above constitutive equations in (2.1) and (2.2) can then be written in standard tensor notation as shown below [3]. Compliance s is a 4th rank tensor, stress T and strain S are both 2nd rank tensors and dielectric and piezoelectric quantities are 3rd rank tensors.

$$D_i = d_{iq}.T_q + \varepsilon_{ik}^T.E_k \tag{2.3}$$

$$S_{ij} = s_{pq}^E.T_q + d_{kp}.E_k \tag{2.4}$$

where, i, j, k □ [1, 2, 3] and p, q □ [1, 2, 3, 4, 5, 6] and based on the following governing rule.

$$S_{ij} = S_p \; ; \qquad p = 1, 2, 3 \text{ for } i = j \text{ and } p = 4, 5, 6 \text{ for } i \neq j \tag{2.5}$$

The piezoelectric effect of a material is the result of coupled interaction between electrical and mechanical systems and is expressed by a set of piezoelectric and dielectric constants. Table 2.2 describes some of the piezoelectric constants as defined in the standard [32].

Table 2.2 List of Piezoelectric Constants and Definition

Notation	Type	Description	Unit
d_{33}	Charge constant	Polarization in 3 per unit applied stress in 3 (Strain induced in 3 per unit electric field in 3)	pC/N (pm/V)
d_{31}	Charge constant	Polarization in 3 per unit applied stress in 1 (Strain induced in 1 per unit electric field in 3)	pC/N (pm/V)
g_{33}	Voltage constant	Induced electric field in 3 per applied stress in 3	V-m/N
g_{31}	Voltage constant	Induced electric field in 3 per applied stress in 1	V-m/N
ε_{33}	Dielectric constant	Dielectric constant for dielectric displacement and electric field in 3	-
k_{33}	Longitudinal coupling constant	Longitudinal vibrations in 3 of a bar shape with aspect ratio (l/w) > 10 for electric field in 3	-
k_{31}	Transverse coupling constant	Transverse vibrations in 1 of a bar shape for electric field in 3	-
k_p	Planar coupling constant	Radial vibrations in 1 and 2 of a disc for electric field in 3	-
k_t	Thickness coupling constant	Thickness mode vibrations for samples with large surface dimensions relative to thickness Vibration in 3 with electric field in 3	-

The electromechanical coupling constant's, k_{33}, k_{31}, k_p *and* k_t, are an indicator of the effectiveness of energy transduction by the type and shape of any piezoelectric material. The effective coupling factor, k_{eff}, is proportional to the measure of the efficiency with which electrical energy is converted to mechanical energy and vice versa as shown in (2.6)

$$k_{eff} = \sqrt{\frac{Energy \cdot Output}{Energy \cdot Input}} \tag{2.6}$$

2.2 PMN-PT Relaxor Ferroelectric System

In categorizing crystal systems based on symmetry, 11 of the 32 crystal classes are centrosymmetric. These 11 crystal classes or point groups have a center of symmetry and no net polarization and hence doesn't exhibit any piezoelectric and dielectric properties. Out of the remaining 21 point groups, all of them but one, '432' point group, exhibit piezoelectric properties along a unique direction. Among them, ten point groups are ferroelectric in nature and are polar crystals since they display spontaneous polarization [4]. Within this ferroelectric group, the perovskites are a specific class of ceramics which exhibit piezoelectric properties. The classification of ferroelectric perovskites is shown in Figure 2.3. They have an ABO_3 crystal structure where A and B are metal ions occupying the divalent and tetravalent sites respectively in an oxygen octahedral Figure 2.4. Most common piezoelectric ceramics and single crystals fall under the category of perovskites, e.g. $BaTiO_3$, $PbZrO_3$, $PbTiO_3$, PZT and PMN-PT.

A crystal is said to be ferroelectric when it has a spontaneous polarization below a phase transition temperature (also known as Curie temperature or T_c) and has two or more stable polarization orientation states. Ferroelectricity refers to the property that the spontaneous polarization can be switched between these states by application of an external electric field [5, 6]. In most cases, the spontaneous polarization in a ferroelectric crystal is not uniformly distributed throughout the whole crystal but rather forms small regions, called domains, with each domain having uniform polarization. The existence of the ferroelectric domains can be explained from the minimization of free energy from both electrical and mechanical constraints. The polarization direction of each domain is determined by the crystal symmetry of the ferroelectric crystal [7].

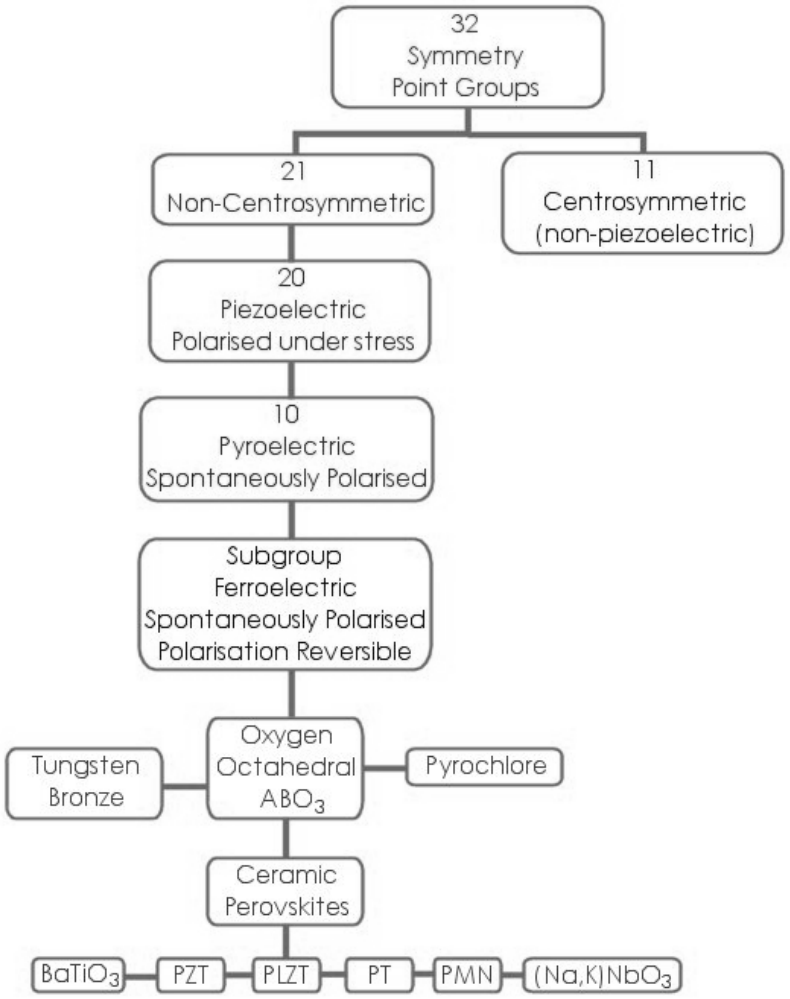

Figure 2.3: Categorization of perovskite-based piezoelectric materials

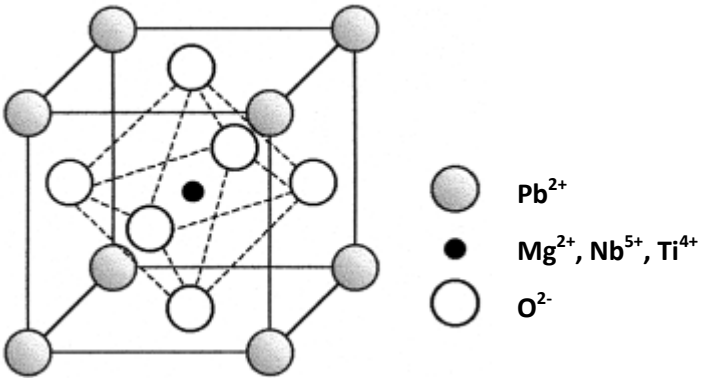

Figure 2.4: Perovskite structure ABO_3 type

The process of applying an electric field to orient the domains toward the field direction is termed “poling”. For a poled ferroelectric crystal, the switching of polarization direction to another orientation (or reverse) involves hysteresis due to resistance from polarization switching as schematically shown in Figure 2.5. The reversing electric field required to cancel all the polarization is known as the coercive field (E_c). The spontaneous polarization (P_s) is determined by extrapolating the linear saturating portion back to the polarization axis. The retained polarization after removal of the external poling field is called remnant polarization (P_r) which is always smaller than the spontaneous polarization. Most ferroelectrics lose spontaneous polarization ($P_s \approx 0$) above the Curie temperature [2]. The non-polar phase above T_c is the paraelectric phase and this temperature marks the ferroelectric - paraelectric phase transition which is signaled as a first order phase change in a dielectric constant peak.

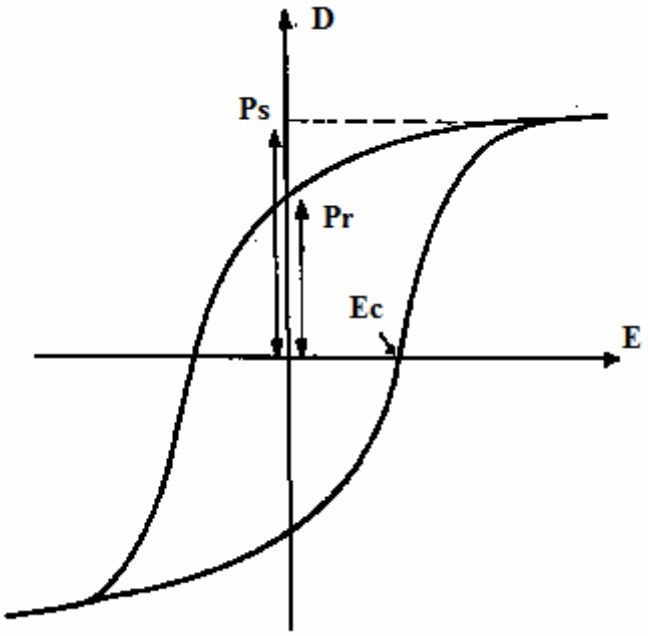

Figure 2.5: Typical dielectric polarization vs. electric field hysteresis for ferroelectrics

Relaxor ferroelectrics are a variant of ferroelectrics which exhibit good piezoelectric properties and differ from normal ferroelectrics in the following ways [1, 8]:

1) The relaxor ferroelectrics have a broader diffused phase transition from paraelectric to ferroelectric phase than normal ferroelectrics. Unlike the normal ferroelectrics, relaxor ferroelectrics have strong frequency dependence and the T_c shifts to a higher temperature and the maximum dielectric permittivity decreases with an increase in frequency.

2) Relaxor ferroelectrics have smaller remnant polarization (P_r) than normal ferroelectrics. This leads to lower area or energy stored under the hysteresis loop for a relaxor ferroelectric.

3) The relaxor ferroelectrics have no line splitting on diffraction of x-rays due to weak anisotropy in the diffused Curie phase transition. Normal ferroelectric, on the other hand, has strong anisotropy and hence line splitting on x-ray diffraction.

The strong diffused phase transition in relaxor ferroelectrics is explained by the existence of nano-polar domains in the vicinity of the Curie temperature, T_c [9]. However, the induced polarization in these materials can be lost at a far lower temperature known as the diffuse phase transition temperature or T_d, where $T_d < T_c$. This is due to the loss of induced macro polarization domains at T_d. Figure 2.6 shows the variation of typical dielectric constant with temperature for a relaxor ferroelectric material and a normal ferroelectric material. The lower phase transition temperature T_d also determines the range of operation for relaxor ferroelectrics.

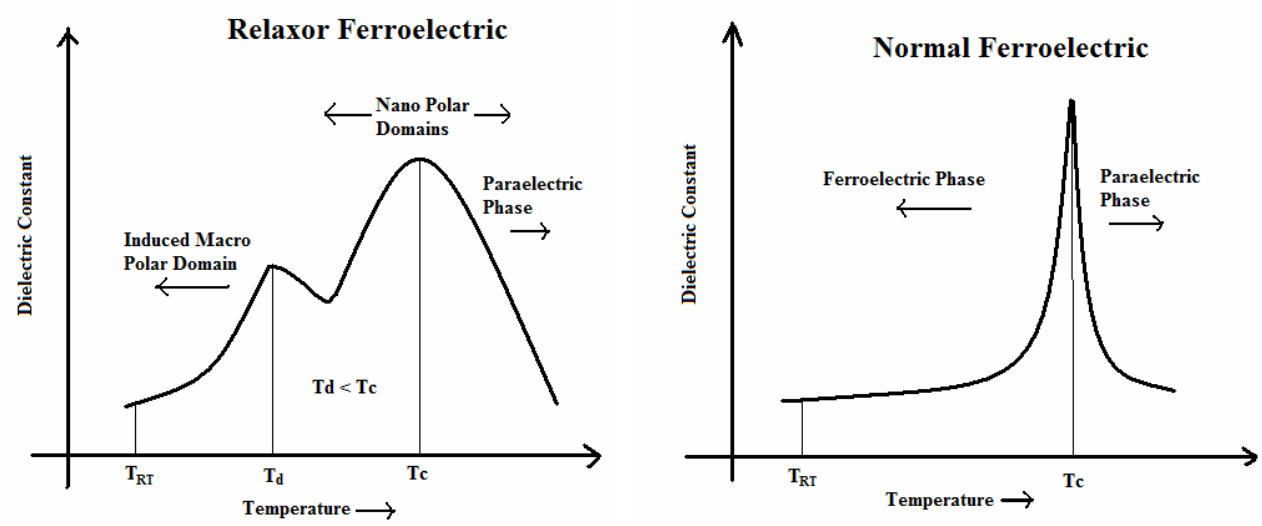

T_{RT} – Room temperature
T_d – Diffuse phase transition temperature
T_c – Curie temperature

Figure 2.6: Typical dielectric vs. temperature showing phase transition in relaxor and normal ferroelectrics

PMN-PT is a relaxor ferroelectric compound with the composition formula of *(1-x)*[Pb $(Mg_{1/3}Nb_{2/3})\ O_3$] – $x PbTiO_3$, with complex morphotropic phase boundaries in the region ($0.3 < x < 0.35$) at room temperature. PMN-PT is a solid solution of a relaxor ferroelectric $Pb(Mg_{1/3}Nb_{2/3})O_3$ or PMN and a normal ferroelectric $PbTiO_3$ or PT. It is stable at room temperature and exhibits excellent piezoelectric properties near the morphotropic phase boundary (MPB). The phase diagram of PMN-PT has been developed over the last decade by a number of researchers and different techniques. Shrout and Fielding introduced the phase diagram of PMN-PT in a general understanding of the behavior of complex relaxor ferroelectrics, as shown in Figure 2.7a. They also found that the polarization behavior of PMN-PT system depend on the local crystal composition which determines its use for a specific

application. Later, Noheda et al. performed high resolution synchrotron X-Ray experiments near the MPB compositions of PMN-PT and found the existence of a complex phase ordering with coexisting phases in the same crystal composition. This led to their modification of the existing phase diagram by the inclusion of an intermediate monoclinic (M_C) phase around 33% PT, Figure 2.7b. The phase diagram was further worked upon by Shrout et al. [10] and modified by Guo et al. [11] where he clearly distinguishes the two boundaries at 30% and 35% PT and also proposes the existence of intermediate orthorhombic phases in the MPB, as shown in Figure 2.7c. Although this rendition with the inclusion of orthorhombic phases demonstrated the complexity of PMN-PT system around the MPB, it is widely accepted in the community.

The addition of PT which has a high Curie, T_c (≈ 480 ºC) with PMN which is a low T_c (≈ -10 ºC) results in PMN-PT shifts to the T_c to higher temperatures (130 ºC – 180 ºC) for 28 – 35% PT. For the PMN-PT solid solution in paraelectric phase, i.e. above T_c, at all compositions, the crystal has a cubic phase with 'm3m' symmetry [12]. Below T_c and towards the left side of MPB with composition below 30% PT, it exists in a ferroelectric rhombohedral phase of '3m' symmetry. Towards the right side of MPB with composition above 35% PT, the macroscopic symmetry of the multidomain structure is a pure tetragonal phase with '4mm' symmetry. Within the MPB, the macroscopic symmetry is a mixture of the underlying microscopic domains. The monoclinic 'm' phase is formed across the MPB with 31 – 34% PT where the observed piezoelectric property is found to be at a maximum. The existence of orthorhombic phases with 'mm2' symmetry along the either side of MPB is still debated. It is believed to exist in a mixed phase with the underlying tetragonal or rhombohedral symmetry to relax the crystal into the intermediate monoclinic phase.

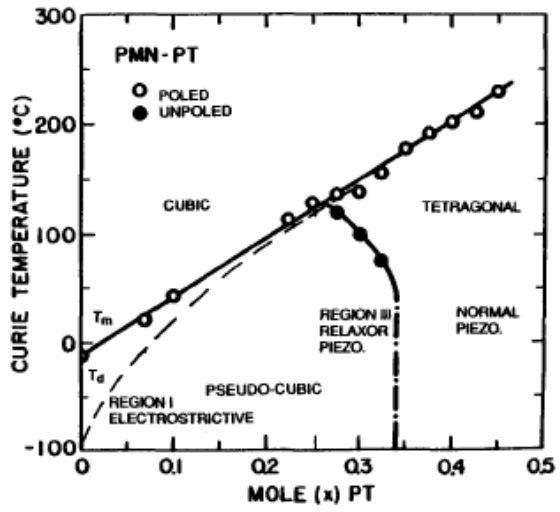

(a) Phase diagram proposed by Shrout and Fielding, [33]

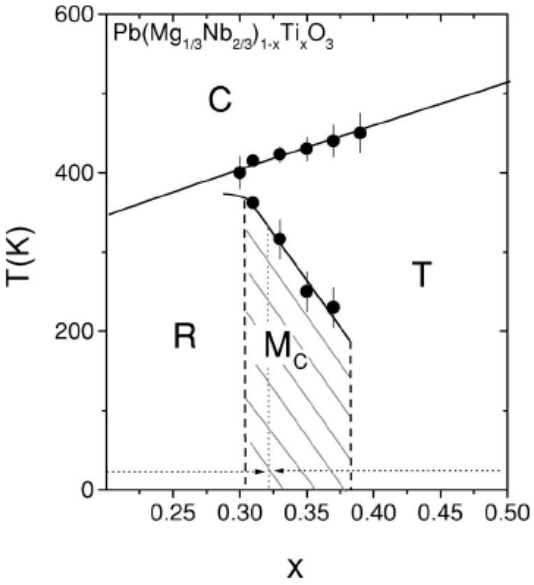

(b) Phase diagram as modified by Noheda et al., [34]

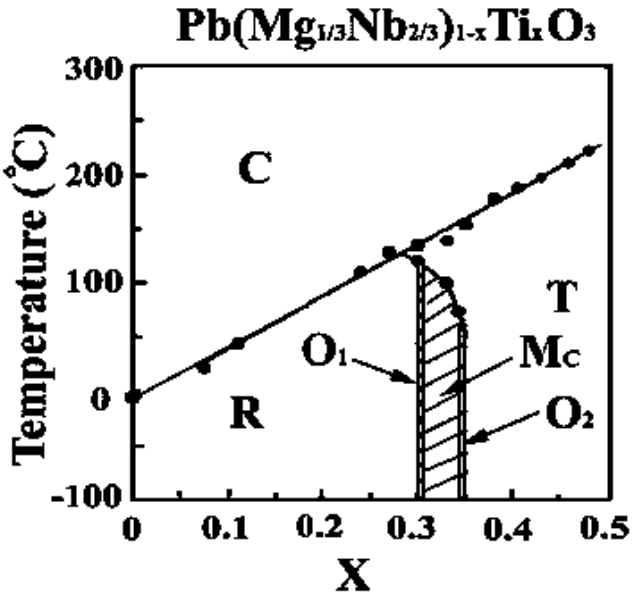

C – Cubic

R – Rhombohedral

O_1 & O_2 – Orthorhombic

M_C – Monoclinic

T – Tetragonal

(c) Phase diagram by Guo et al. [11]

Figure 2.7: Phase diagrams of PMN-PT relaxor ferroelectric showing MPB [10, 11, 33, 34]

The thermal, electrical and the mechanical properties of a crystal are related by a set of fundamental properties [3]. There are 7 fundamental constants which relate these three properties. They are the following: 1) elastic compliances, *s*; 2) piezoelectric charge constant, *d*; 3) thermal expansion; 4) dielectric constant, ε ; 5) pyroelectric coefficient; 6) heat capacity; and 7) absolute temperature. Neglecting the effect of a change in temperature the constitutive equations defined in (2.3) – (2.5) can be written as the crystal properties matrix:

	T	E	No. of terms
S	*s*	d_t	6
D	*d*	ε	3

Figure 2.8: Electro-mechanical properties matrix for a piezoelectric crystal

All the properties of a crystal can be presented in a single 9 x 9 matrix or in 81 constants [32]. The number of independent constants depends on the crystal symmetry of the point group. The set of properties matrix can be determined by a combination of experimental and computational methods. For PMN-PT in tetragonal phase above the MPB, the basic macroscopic symmetry is that of the '4mm' point group which reduces the number of independent constants to 11. Those are 6 elastic constants, 3 piezoelectric constants and 2 dielectric constants, [32]. This is demonstrated in Figure 2.9a. Similarly, the monoclinic phase along the MPB with point group symmetry 'm', the number of independent constants is 27. That includes 13 elastic constants, 10 piezoelectric constants and 4 dielectric constants (Figure 2.9b).

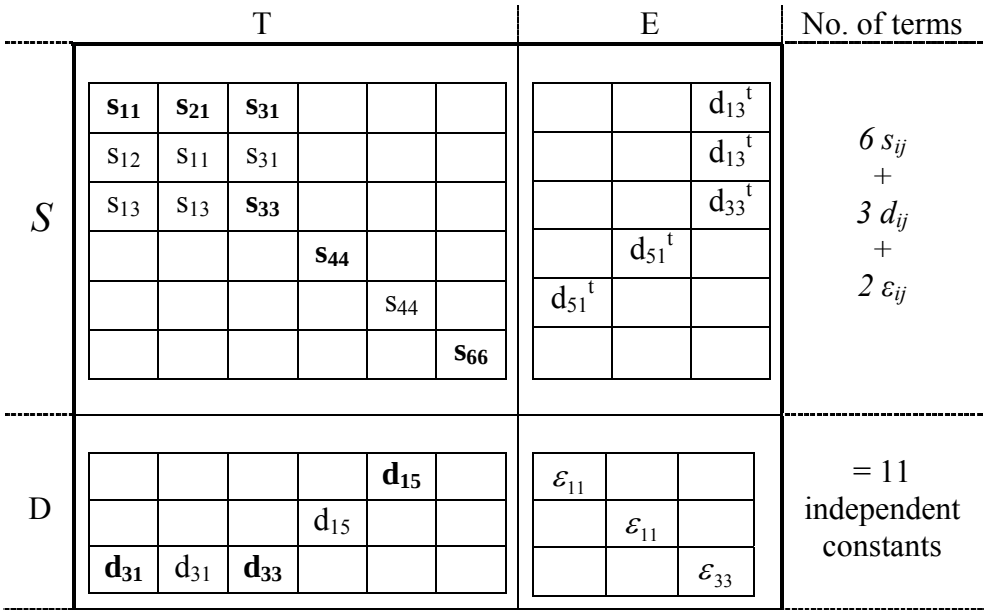

Figure 2.9a: Matrix representation for tetragonal '4mm' symmetry
($s_{11} = s_{22}$; $s_{13} = s_{23} = s_{13} = s_{31}$; $s_{44} = s_{55}$; $d_{31} = d_{32}$ and $k_{11} = k_{22}$)

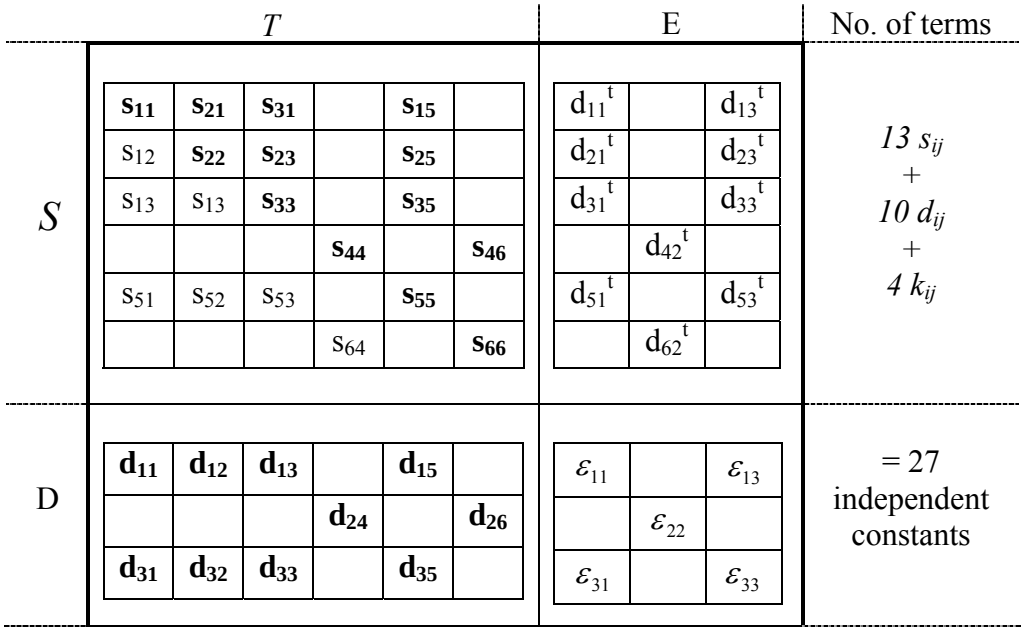

Figure 2.9b: Matrix representation for monoclinic 'm' symmetry

2.3 Properties of Single Crystal PMN-PT

A lot of research has been done in analyzing the properties of single crystal PMN-PT relaxor ferroelectric [12-16]. It exhibits complex behavior close to the MPB due to the simultaneous coexistence of different crystallographic phases. This leads to a non-linear variation of piezoelectric properties in these crystals depending on the combination of the following factors.

1) Composition of the single-crystal PMN-PT
2) Crystallographic orientation
3) Electric polarization
4) Defects and impurities

During crystal growth from solid solution, segregation of PT occurs and results in a change of morphotropy along the crystal when cooled to room temperature. This results in induced strain in the lattice due to size difference of the B-site cations, Ti^{+4}, Mg^{+2} and Nb^{+5}. With the variation of PT in the crystal, the lattice symmetry changes from rhombohedra to tetragonal via an intermediate monoclinic phase at MPB. Theoretical calculations of properties matrix by Cao et al. revealed extraordinarily large piezoelectric charge coefficients, *d*, for the crystals lying in the MPB and having a monoclinic type macroscopic symmetry. The crystals were oriented and poled in [001] pseudo-cubic notation which is also the Z or 3 axis as shown in Figure 2.2. Table 2.3 provides a comparison of the properties based on studies by Cao et al [17-19]. PMN-0.3PT will have a '3m' rhombohedral symmetry. PMN-0.33PT has an 'm' monoclinic macroscopic symmetry while PMN-0.42 PT has '4mm' tetragonal symmetry.

Table 2.3: Comparison of Properties of <001> Poled PMN-PT Crystals from Experimental and Theoretical Studies [17 – 19]

Properties	**PMN-0.3PT [18] rhombohedral**	**PMN-0.33PT [17] monoclinic**	**PMN-0.42PT [19] tetragonal**
Density, g/cc	8.03	8.06	8.1
Curie Temp., ºC	130 ºC	145 ºC	>180 ºC
d_{31}, pC/N	-921	-1330	-91
d_{33}, pC/N	1981	2820	260
d_{15}, pC/N	190	146	131
k_{31}	0.49	0.59	0.39
k_{33}	0.92	0.94	0.78
k_{15}	0.29	0.32	0.8
g_{31}, 10^{-3} V-m/N	-13.3	-18.4	-15.57
g_{33}, 10^{-3} V-m/N	28.7	38.8	44.5
g_{15}, 10^{-3} V-m/N	6.0	10.3	17.23

For the crystals poled along <001>, the longitudinal and transverse mode piezoelectric coefficients are lower in the tetragonal phase than the other two. However, compositions in rhombohedral phase has a wide bandwidth response in the longitudinal mode of operation and have enabled the use of single crystals for ultrasound transducer heads, [35]. Due to the high piezoelectric constants it is slowly replacing the widely used PZT ceramics which was the primary material of choice for more than 40 years.

Poling of the single crystal PMN-PT along a certain crystallographic direction induce a macroscopic domain symmetry. This is due to the alignment of the dipoles upon application of the electric field [20]. Figure 2.10 shows a schematic of the [001], [110] and [111] cuts of a pseudo-cubic crystal. Much of the early published literature had focused on the properties of [001] oriented and poled rhombohedral phase crystals due to their high electromechanical coupling coefficient (k_{33} > 90%) and high piezoelectric constant (d_{33} _ 2000 pC/N) [13, 21, 22]. The electromechanical properties of [111] cuts were found to be relatively low (k_{33} < 0.65). Chen et al. measured the electromechanical and dielectric properties of [110] oriented PMN-0.31PT single crystal slivers and reported a coupling constant k_{33} as high as 0.91 (Figure 2.11) [23]. Due to lower d_{33} coefficients, [110] cut single crystals were not used significantly for longitudinal mode operation for medical ultrasound devices and actuators.

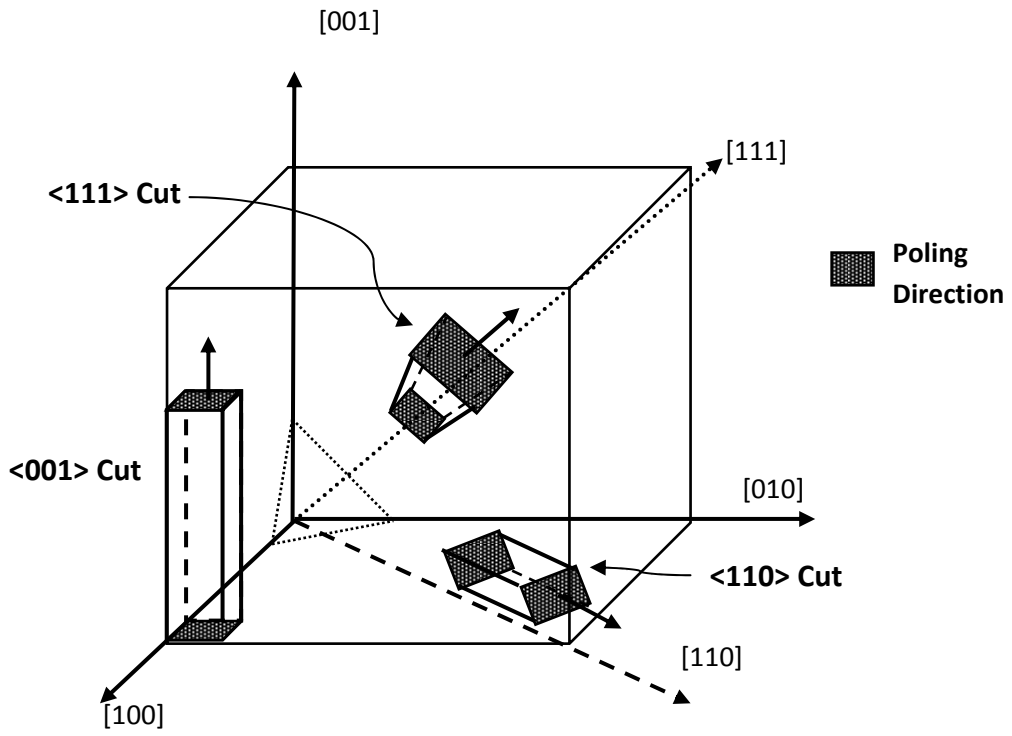

Figure 2.10: Schematic of <001>, <110> and <111> cuts of pseudo-cubic crystal

The effective coupling constants of PMN-PT 31% cuts at or near <001>, <011> orientations (Sample geometry: 2.4 mm × 0.8 mm × 0.8 mm)

PMN-PT 31% (bar, L:W = 3:1)	Effective Coupling Constant k'_{33}
<001> 0 degree	0.89
<001> 2.5 degree	0.87
<001> 5 degree	0.88
<001> 10 degree	0.87
<011> 15 degree	0.85
<011> 0 degree	0.88
<011> 2.5 degree	0.87
<011> 5 degree	0.86
<011> 10 degree	0.85
<011> 15 degree	0.83

Figure 2.11: Comparison of k_{33} for PMN-0.31PT bars with orientation along <001> and <011> direction. The k_{33} difference increased with the degree of disorientation (Adapted from [23]).

For the transverse mode sensing application, it was found that the d_{31} for <011> oriented PMN-PT was more than that in <001> direction. The d_{31} for <001> poled crystals are typically about 50% or less of the d_{33} coefficient. The crystals poled in <011> have an induced 'mm2' orthorhombic macroscopic symmetry and thus exhibits higher d_{31} coefficients in transverse mode and low d_{33} coefficients [14]. The <011> crystallographic orientation can be suitably used for realizing high piezoelectric output and higher sensitivity in transverse mode. Bending structures used in this work for energy harvesting utilized the transverse sensing mode of piezoelectric single crystals. It was hypothesized that an orientation of <011> or close (within 10-15 degrees) is ideal for an energy harvesting application and this will be emphasized further in this study. The variation of d_{31} and d_{33} with orientation and poling direction is presented in Table 2.4.

Table 2.4: Comparison of Piezoelectric Charge Coefficients for Single Crystal PMN-PT with Orientation and Poling Direction. The composition was between 0.27 - 0.33 PT [24].

Orientation and Poling direction	Transverse excitation mode, d_{31} and d_{32}	Longitudinal excitation mode, d_{33}
<001> poling	-800 to -1000 pC/N	2000 to 2500 pC/N
<011> poling	-1200 to -1800 pC/N	< 500 pC/N
<111> poling	< 150 pC/N	< 200 pC/N

The other two important factors that affect the properties of the PMN-PT relaxor single crystals are the strength of the poling field and presence of impurities or dopants [25, 26]. The magnitude of the electric field used to induce polarization of the domain structure depends on the composition of the single crystal or the underlying symmetry of the lattice. It has been observed that electric fields greater than 250 V/mm tend to deteriorate the properties in rhombohedral phase, i.e < 0.32 PT. Over poling leads to pinning of the domains and hence reduces the effective degree of polarization. However, in tetragonal phase or compositions greater than 0.35 PT, a higher electric field greater than 300 V/mm is required for poling. Similarly it has been observed, that the presence of dopants or impurities can also lead to distortion of the lattice symmetries and hence the properties of the crystals and is beyond the scope of work described in this thesis.

2.4 Choice of PMN-PT as a Material for Energy Harvesting

As seen in the previous section, the properties of PMN-PT are complex in nature and depend on several factors. However, they are better than other available ceramics and polymers and provide an attractive option for piezoelectric devices in various applications. Table 2.5 shows a comparison of [001] PMN-PT[a] single crystal available from a vendor with PMN ceramic (EC-98[b] from EDO Corp.), hard PZT ceramic (EC-69[c] from EDO Corp) and PVDF[d] polymer from Measurements Specialties Inc [28-30].

Table 2.5 Comparison of Properties of Different Piezoelectric Materials

Property	PMN Ceramic EC-98[b]	PZT Ceramic EC-69[c]	PVDF[d] Film	PMN-PT[a] Single Crystal [001] 0.3-0.32 PT
Density, g/cc	6.1	7.5	1.78	8.2
Modulus of Elasticity, GPa	61.0	99	2-4	20-25
Dielectric Constant (1 kHz)	5500	1050	12 – 13	4500-6000
Dissipation Factor	<2	0.3	0.02	<0.01
d_{31}, pc/N	-312	-95	23	-920
d_{33}, pc/N	730	220	33	1600
k_{31}	0.35	0.31	0.12	0.62
k_{33}	0.72	0.62	0.14	>0.85
Mechanical Q	70	60	10	30-70
g_{31}, 10^{-3} V-m/N	-6.4	-10.2	-216	
g_{33}, 10^-3 V-m/N	15.6	23.7	330	

The choice of piezoelectric material for any given application depends on many design parameters. But for a given excitation, a material with better piezoelectric coefficients will have a higher performance which can be resolved by a theoretical Figure of Merit (F.O.M.) calculation. Work done, *W*, by a piezoelectric element can be expressed as the following:

$$W = \frac{1}{2}.CV^2 = \frac{1}{2}.g_{ij}.d_{ij}.v.(\sigma_{ij}^{A})^2 \tag{2.7}$$

where, *W* is work done

C is effective open circuit capacitance

V is open circuit voltage produced

g_{ij} and d_{ij} are piezoelectric constants

v is effective volume of the piezoelectric transducer

and σ_{ij}^{A} is the applied stress field

A comparison of performance can be attempted for two transducers of different piezoelectric material having same dimensions operating under same stress field and same mode. The F.O.M. can be defined as proportional to the product, Π, of the piezoelectric charge constant, d_{ij}, and the piezoelectric voltage constant, g_{ij}. Table 2.6 shows the F.O.M. comparison for a two PZT and PMN-PT compositions [31].

$$\Pi_{ij} = d_{ij}.g_{ij} \tag{2.8}$$

Table 2.6: Figure of Merit Comparison for PZT and PMN-PT in Transverse Mode

F.O.M.		PZT-5H	PZT-5A	PMN-0.3PT [001]	PMN-0.33PT [011]
Transverse or 31 mode	d_{31} (pC/N)	-274	-171	-921	-1750
	g_{31} (10^{-3} V-m/N)	-9.11	-11.4	-13.3	~ -14.0
	Π_{31}	2496	1950	12250	24500

From the table above and for a typical PMN-0.33PT transducer, the F.O.M. is 10 times better than a typical PZT ceramic material, i.e. under identical stress field the theoretical power density achieved by PMN-PT can be a factor of 10 more. That would be a significant improvement for devices being used for low power energy harvesting.

References

[1] Cady W.G., "Piezoeletricity: An introduction to theory and Applications of electromechanical phenomena in Crystals", Vol. 1, Dover Publications.

[2] A.P.C. International Ltd., "Piezoelectric Ceramics: Principles and Applications", ISBN 13: 9780971874404.

[3] Nye J.F., "Physical Properties of Crystals: Their Representation by Tensors and Matrices", Oxford University Press, ISBN-13: 9780198511656.

[4] Xu Y.H., "Ferroelectric Materials and Their Applications", North-Holland, Amsterdam 1991, ISBN-13: 978-0-444-88354-4.

[5] Cohen R., "Origin of Ferroelectricity in Perovskite Oxides", Nature, 358, July 1992, pp. 136-138.

[6] Cross L.E., "Relaxor Ferroelectrics", Ferroelectrics, 76 (1), 1987, pp. 241-267.

[7] Hatch D. M. and Cao W., "Determination of Domain and Domain Wall Formation at Ferroic Transitions", Ferroelectric, 222, 1999, pp. 1-10.

[8] Ye Z.-G., "Relaxor Ferroelectric Complex Perovskies: Structures, Properties and Phase Transitions", in "Oxides: Phase Transitions, Non Stoichiometry and Superconductors", Key Engineering Materials, 155-156, Trans Tech Publication, 1998, pp. 81-122.

[9] Lebon A., Dammak H. and Calvarin G., "Tetragonal and rhombohedral induced polar order from the relaxor state of $PbZn_{1/3}Nb_{2/3}O_3$", Journal of Physics: Condensed Matter, 15, 2003, pp. 3069-3078.

[10] Shrout T.R., Chang Z.P., Kim N. and Markgraf S., Ferroelectric Letters, 12 (3), 1990, pp. 63-69.

[11] Guo Y., Luo H., Ling D., Xu H., He T. and Yin Z., "The phase transition sequence and the location of the morphotropic phase boundary region in $(1-x)[Pb(Mg_{1/3}Nb_{2/3})O_3]-xPbTiO_3$ single crystal", Journal of Physics: Condensed Matter, 15, 2003, pp. L77–L82.

[12] Zhang R., Jiang B. and Cao W., "Orientation dependence of piezoelectric properties of single domain $0.67Pb(Mg_{1/3}Nb_{2/3})O_3 - 0.33PbTiO_3$ crystals", Applied Physics Letters, 82 (21) 2003, pp. 3737-3739.

[13] Liu T. and Lynch C.S., "Ferroelectric properties of [110], [001] and [111] poled relaxor single crystals: measurements and modeling", Acta Materialia, 51, 2003, pp. 407–416.

[14] Han P.D., Yan W., Tian J., Huang X. and Pan H., "Cut directions for the optimization of piezoelectric coefficients of lead magnesium niobate–lead titanate ferroelectric crystals", Applied Physics Letters, 86, 2005, pp. 052902-1.

[15] Han P.D., "Progress in PMN-PT Crystal Growth", 2002 U.S. Navy workshop on acoustic transduction materials and devices, 13-15 May, 2002, Penn State University.

[16] Xu G., Luo H., Guo Y., Gao Y., Xu H., Qi Z., Zhong W. and Yin Z., "Growth and piezoelectric properties of $Pb(Mg_{1/3}Nb_{2/3})O_3 - PbTiO_3$ crystals by the modified Bridgman method", Solid State Communications, 120, 2001, pp. 321-324.

[17] Zhang R., Jiang B. and Cao W., "Elastic, piezoelectric, and dielectric properties of multidomain $0.67Pb(Mg_{1/3}Nb_{2/3})O_3 - 0.33PbTiO_3$ single crystals", Journal of Applied Physics, 90 (7), 2001, pp. 3471- 3475.

[18] Zhang R., Jiang W., Jiang B. and Cao W., "Elastic, Dielectric and Piezoelctric Coefficients of Domain Engineered $0.70Pb(Mg_{1/3}Nb_{2/3})O_3$-$0.30PbTiO_3$ Single Crystal", AIP Conference Proceedings, 626, 2002, pp. 188-197.

[19] Cao H., Schmidt V. H., Zhang R., Cao W. and Luo H., "Elastic, piezoelectric, and dielectric properties of $0.58Pb(Mg_{1/3}Nb_{2/3})O_3$-$0.42PbTiO_3$ single crystal", Journal of Applied Physics, 96 (1), 2004, pp. 549-554.

[20] Hatch D.M., Stokes H.T. and Cao W., "Allowed mesoscopic point group symmetries in domain average engineering of perovskite ferroelectric crystals", Journal of Applied Physics, 94 (8), 2003, pp. 5220-5227.

[21] Park S.E. and Shrout T.R., **"**Ultrahigh strain and piezoelectric behavior in relaxor based ferroelectric single crystals" Journal of Applied Physics, 82 (4), 1997, pp. 1804-1811.

[22] Yin Z.W., Luo H., Wang P.C. and Xu G.S., "Growth, characterization and properties of relaxor ferroelectric PMN-PT single crystals", Ferroelectrics, 229 (1), 1999, pp. 207-216.

[23] Chen J., Panda R.K., Gururaja T.R. and Beck H., "Single Crystal Thickness and Width Cuts for Enhanced Ultrasonic Transducers", U.S. Patent No. – US 6,465,937 B1, October 15 2002.

[24] H. C. Materials, Properties of PMN-PT Single Crystals, "www.hcmat.com/Pmn_Opportunities.html".

[25] Shanthi M., Chia S.M. and Lim L.C., "Overpoling resistance of [011]-poled $Pb(Mg_{1/3}Nb_{2/3})O_3$–$PbTiO_3$ single crystals", Applied Physics Letters, 87, 2005, pp. 202902.

[26] Kiat J.M., Uesu Y., Dkhil B., Matsuda MX., Malibert C. and Calvarin G., "Monoclinic structure of unpoled morphotropic high piezoelectric $(PbMg_{1/3}Nb_{2/3}O_3)_{0.65}$-$(PbTiO_3)_{0.35}$ and $(PbZn_{1/3}Nb_{2/3}O_3)_{0.91}$-$(PbTiO_3)_{0.09}$ compounds", Condensed Matter: Materials Science, 2001.

[27] Lee S.M., Kim D.H., Lee H.Y., Amin A., Zhang S.J. and Shrout T.R., "Piezoelectrically "Hard" Relaxor-PT Single Crystals", 2008 U.S. Navy workshop on acoustic transduction materials and devices, 12-15 May, 2008, Penn State University.

[28] Electro Ceramic Products, EDO Corporation. “www.edoceramics.com”.

[29] Measurement Specialities Inc., “www.meas-spec.com”.

[30] Morgan Electro Ceramics Inc., “www.morganelectroceramics.com”.

[31] Priya S., “Advances in energy harvesting using low profile piezoelectric transducers”, Journal of Electroceramics, 19 (1), 2007, pp. 167-184.

[32] IEEE Standard on Piezoelectricity, ANSI/IEEE Std. 176-1987.

[33] Shrout T. R. and Fielding J. Jr., “Relaxor Ferroelectric Materials”, IEEE Ultrasonics Symposium, 1990, pp. 711–720.

[34] Noheda B., Cox D.E., Shirane G., Gao J. and Ye Z.G., “Phase diagram of the ferroelectric relaxor *(1-x)*$PbMg_{1/3}Nb_{2/3}O_3 - x PbTiO_3$”, Physical Review B, 66, 2002, pp. 054104.

[35] Park S.E. and Shrout T.R., “Characteristics of relaxor-based piezoelectric single crystals for ultrasonic transducers”, IEEE Transactions of Ultrasonics, Ferroelectrics and Frequency Control, 44, 1997, pp. 1140-1147.

CHAPTER – 3

TRANSDUCER FABRICATION

For energy harvesting from acoustic sources, 1.5 kHz – 3.5 kHz, bending mode unimorph transducers were fabricated. A *unimorph* is a transducer that consists of one active layer bonded to an inactive layer. In this work, the active layer of the unimorph consisted of single crystal PMN-PT piezoelectric while the inactive layer was fabricated from brass. The relative magnitude of displacement from piezoelectric materials is very small typically on the order of a few μm. By bonding the thin piezoelectric disk to a metal plate, it is possible to produce a device capable of much larger displacement [1]. The unimorph structure also has a lower resonance frequency than the piezoelectric element alone. The deformation induced by the application of the sound pressure onto the non-piezoelectric back-plate induces a bending mode in the PMN-PT layer and results in an electrical charge.

The parameters for fabrication of the circular unimorphs depend primarily on the clamping and boundary conditions for an application. The use of anisotropic PMN-PT single crystals as active element of the unimorph increases the complexity and needs a thorough analytical analysis of the total system. This is beyond the scope of the work presented in this article. However, an analytical solution of energy conservation and force balance shows that there is an optimal thickness ratio of the piezoelectric material to the non-piezoelectric material which results in maximum power. There is also an optimal ratio of the diameter of the piezoelectric to the diameter of the circular non-piezoelectric plate [2]. Figure 3.1 shows a schematic of a unimorph. R_1 and R_2 are the radii of the

piezoelectric material and non-piezoelectric backplate respectively. The thickness of the PMN-PT wafer is shown as h_p while the thickness of the non-piezoelectric metallic substrate is h_m.

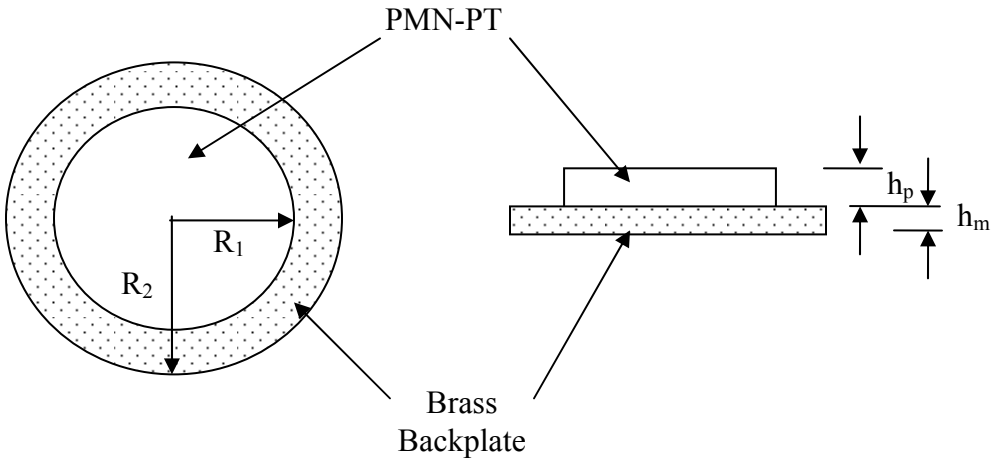

Figure 3.1: Schematic of a PMN-PT unimorph on a brass backplate

3.1 Design Parameters - Theory

Piezoelectric unimorphs are often designed as high displacement actuators by using the indirect piezoelectric effect. In this dissertation, the direct effect is used for generating electrical power from the vibrations from sound pressure in the backplate of the unimorph. It is imperative that reducing the thickness of the substrate, h_m, will increase the maximum induced stress in the unimorph and maximize deflection. Clark et al. did a comparative analysis based on theory of small deflections of a plate with PMN-PT on steel and brass substrates for very low frequency excitations [3]. It was demonstrated in their model that the brass and aluminum substrates yielded higher power

output than steel substrates under same design and excitation. Figure 3.2 shows the model used and the excitation. A brief summary of their test conditions and analytical results is presented.

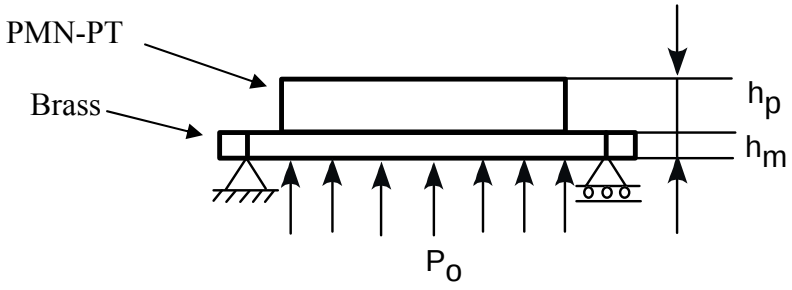

Figure 3.2: Schematic of the analytical model used by Clark et al. P_0 is the uniform excitation of the brass backplate [3]

Test condition:

1. 40mmHg uniform pressure applied to diaphragm
2. 1 Hz excitation frequency

Analytical results from the above model:

1. The thinner the PMN-PT, the higher the power that can be generated.
2. Optimal radius ratio of PMN-PT layer to substrate layer, $R_1/R_2 = 0.83$.
3. Optimal thickness ratio of PMN-PT layer to substrate layer relies on substrate material, $h_p/h_m = 1.41$ for brass, $h_p/h_m = 1.56$ for aluminum, and $h_p/h_m = 1.85$ for steel.

The above results indicate for a given excitation and test condition there is an optimal design for maximizing power output from the unimorphs. The compliance of the non-piezoelectric substrate layer should be less than or equal to the compliance of the

active layer for being able to limit the induced stress on the active layer below the fracture limit at all times. It was observed for a given thickness of the active layer, h_p, the optimal thickness of the substrate, h_m, decreases as the compliance of the substrate material decreases. The limiting factor depends on the amplitude of deflection or strain (%) of the active layer of piezoelectric single crystal due to the induced stress. Table 3.1 lists the compliances of some common substrates and piezoelectric materials. Brass and aluminum are more compliant than stainless steel and would serve as a better substrate for PMN-PT single crystals. In the following sections of this chapter, the fabrication technique of PMN-PT single crystal unimorphs at Washington State University (WSU) is presented with an aim of finding an optimal geometry of the device for energy harvesting from acoustic source.

Table 3.1: Compliances of Some Substrates and Piezoelectric Materials

	Material	**Compliance, s_{11}^E or s_m^E (m^2/N)**
Substrate Layer Non-piezoelectric	Brass	9.52×10^{-12}
	Aluminum	14.28×10^{-12}
	Stainless Steel	5.0×10^{-12}
Active Layer Piezoelectric (un-poled)	PMN – 0.33 PT	12.5×10^{-12}
	PMN – 0.35 PT	10.2×10^{-12}
	PZT – 5H	16.13×10^{-12}
	PZT – 4	15.5×10^{-12}

3.2 Wafering PMN-PT Ingot

*(1-x)*PMN – *x*PT single crystal boules have been grown at Center for Materials Research (CMR) laboratory at WSU with $x = \%PT$ ranging from 29% - 32%. A self seeding High Pressure Bridgman (HPB) growth technique has been used for the single crystal growth [4]. Final diameters of recent growths were 89.0 - 120.0 mm in diameter, thicknesses ranging from 19.0 - 38.0 mm and weighing up to 1.9 kg.

The single crystal can be oriented to a desired crystallographic direction using either an Electron Back-Scatter Diffraction (EBSD) technique or X-Ray Laue Diffraction technique. The most preferred crystallographic orientations of the samples are either <001> or <011>. The piezoelectric properties in transverse mode (d_{31} and k_{31}) is better in <011> oriented samples than in <001> orientation as discussed in an earlier section. Figure 3.3 shows the bottom face of an as grown ingot in the HPB furnace. The ingot was held in front of bright white light to inspect cracks and imperfections resulting from the growth. The growth direction is normal to the plane of the picture going into the page.

For preparing samples, the single crystal ingots were cut using wire saws in preferred directions. The following two types of wire saws have been used and a brief comparison of their cutting techniques is listed in Table 3.2.

1) Single-wire Millennium saw from Diamond Wire Technology, LLC.
2) Multi-wire Saw from Takatori Corporation. (courtesy: Hoffman Materials, LLC) [5].

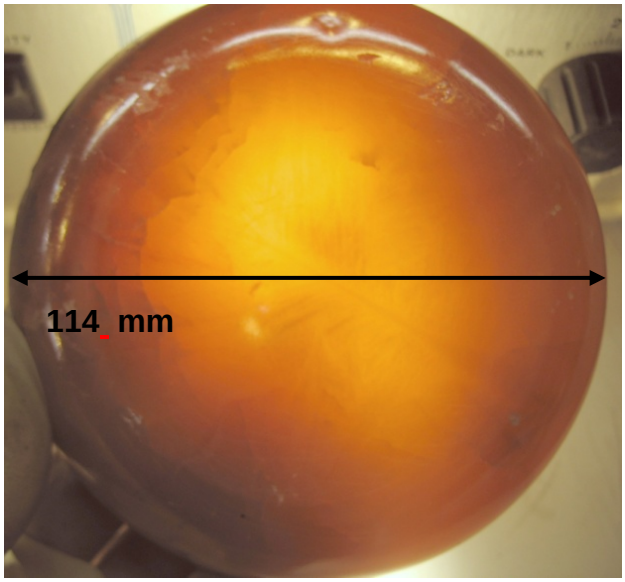

Figure 3.3: Bottom face of a single crystal PMN-PT ingot grown using HPB growth technique

Table 3.2: Comparison of Single-wire Saw vs. Multi-wire Saw

Attributes	**Single-wire saw**	**Multi-wire saw**
Source	Diamond Wire Technology	Hoffman Materials, LLC
Type of wire	Diamond impregnated on Steel core	Stainless steel wire
Slurry	No slurry, but continuous water for cooling	Abrasive slurry (proprietary)
Usage	For bulk sample cuts (bars, squares of variable dimensions)	For thin wafers
Damage	More damaging to the cut PMN-PT surface	Less damaging to the cut PMN-PT surfaces

The single-wire diamond saw caused more damage to the PMN-PT surfaces than the multi-wire saw even at the slowest permitted cutting speed of 0.00635 mm/sec. This is due to the more aggressive cutting nature of the diamond impregnated wire. Figure 3.4 shows a comparison of the cuts made from the two different saws. The parallel lines evident on the left image are the residual saw marks after a cut by the single-wire saw. However, the sample on the right hand side was cut by the multi-wire saw using slurry and it inflicts less damage on the PMN-PT crystal. Surface damage due to the single-wire saw creates stress in the PMN-PT material and can cause cracking or propagation of existing cracks. The cut PMN-PT samples using the multi-wire saw also require much less or no lapping for a better surface finish.

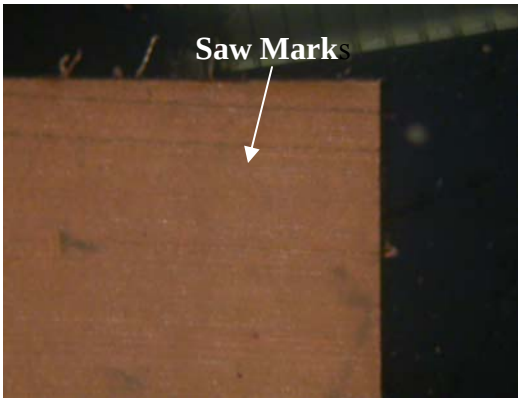

Single-wire diamond saw cut PMN-PT single crystal surface

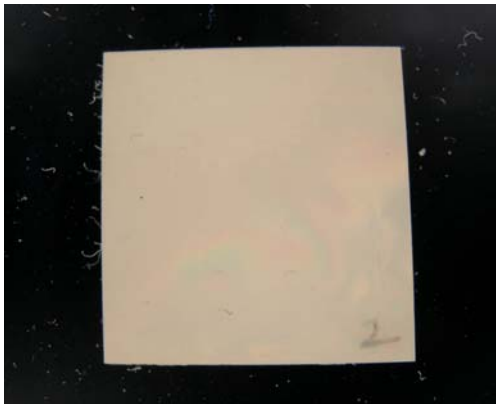

Multi-wire saw cut PMN-PT surface

Figure 3.4: Comparison of the saw cuts on single crystal PMN-PT surface

(Photograph taken at arbitrary magnification)

The single crystal PMN-PT samples used for fabrication of unimorphs were cut by the Multi-wire saw. The as grown single crystal PMN-PT ingots were sliced into 0.19 ±0.01 mm thickness wafers perpendicular to the growth direction which was 12º – 20º off <011> direction. Figure 3.5 shows a schematic of an ingot grown using the HPB growth technique and slicing direction while Figure 3.6 shows some cut PMN-PT wafers.

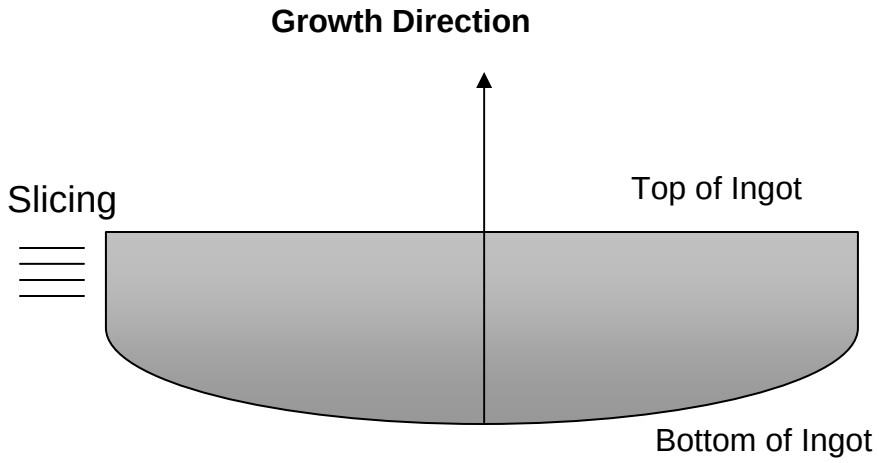

Figure 3.5: Schematic of PMN-PT ingot and slicing direction

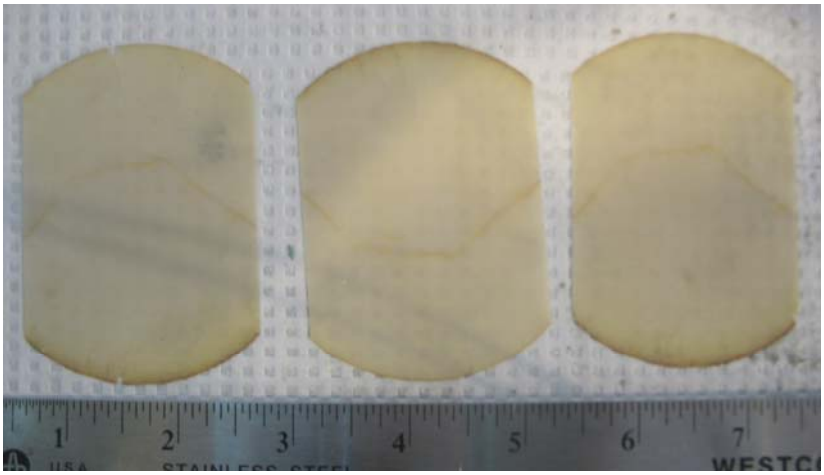

Figure 3.6 PMN-PT single crystal wafers cut by multi-wire saw

3.3 Unimorph Fabrication

After the PMN-PT single crystal ingot was sliced, each wafer was separated and cleaned using ethyl alcohol. The wafers were categorically numbered from top to the bottom of the ingot which enabled tracking of the relative position as it originated from the crystal boule. After cleaning the slurry, the wafers were placed on a light table and cracks and imperfections were marked using a Sharpie marking pen. A region free of cracks and cells was marked where a desired sample was to be cut. Figure 3.7 shows a PMN-PT wafer with the cracks marked. The cracks were marked with a green marker while the circular samples were marked with a red marker. These marks can be erased by dipping the wafer in a beaker containing ethyl alcohol. Two different techniques were used to core circular samples for unimorphs from PMN-PT wafers.

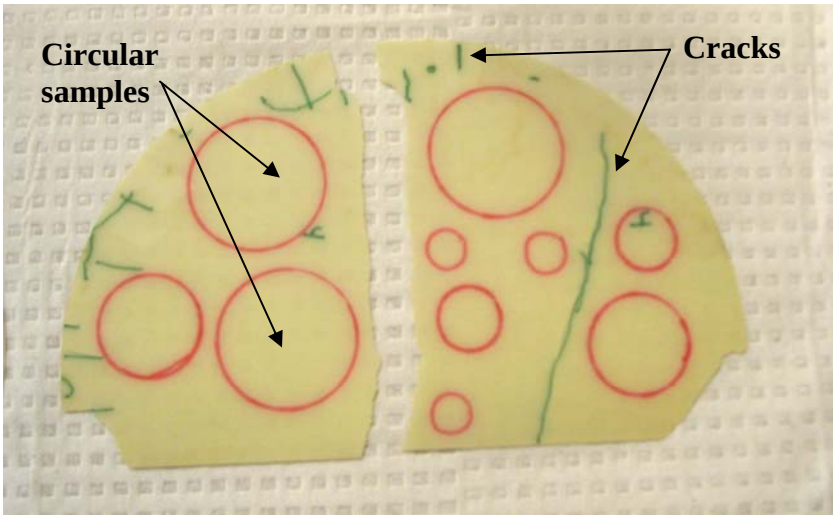

Figure 3.7: Marking of PMN-PT wafer before coring samples

The first technique for coring circular samples was by using a thin-walled diamond coated coring bit in a regular drill press with flowing water as coolant. The PMN-PT wafer was mounted on a graphite block sandwiched between two microscope glass slides. A low temperature Unibond 5.0 wax was used for bonding the wafer in between the glass slides. The glass protects the PMN-PT wafers from a direct impact of core-drill bit. This method was economical but caused chipping on the edges of the PMN-PT sample due to the abrasive diamond core-bit.

The other method consisted of using a UV Laser Micro Drill, Model 5330, from ESI Inc. (courtesy: Microconnex Inc.) [6]. The micro laser drill operates at a wavelength of 355 nm (frequency tripled Nd-YAG) with a spot size of 25 um and spatial resolution in the um range. The samples cored using the Laser had much less chipping on the edges. Two important parameters were monitored while using the laser: The Laser power and Pulse Width. Figure 3.8 shows the chipping on edge of PMN-PT circular sample cut by a diamond coring bit while Figure 3.9 shows the edge of a sample cut using UV Laser.

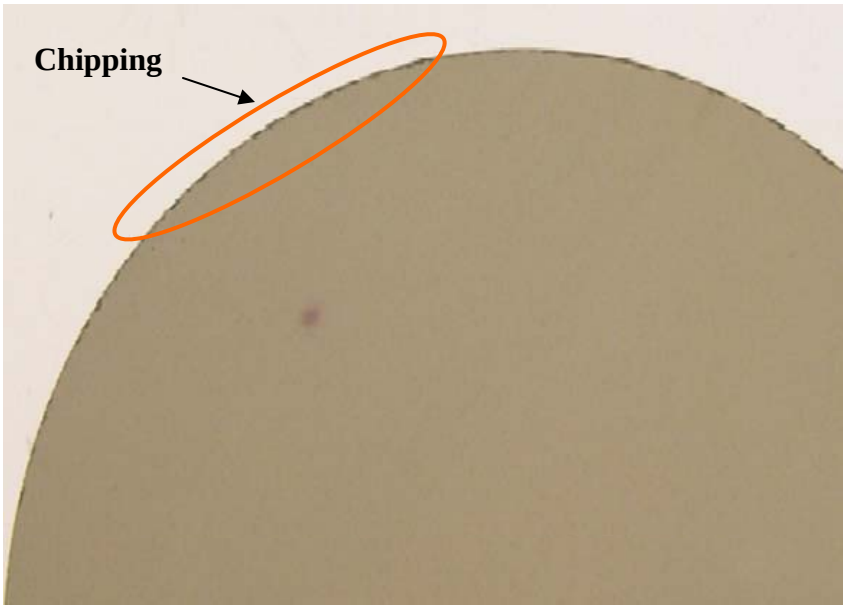

Figure 3.8: Edge of circular PMN-PT sample cut using a diamond coated core-drill bit

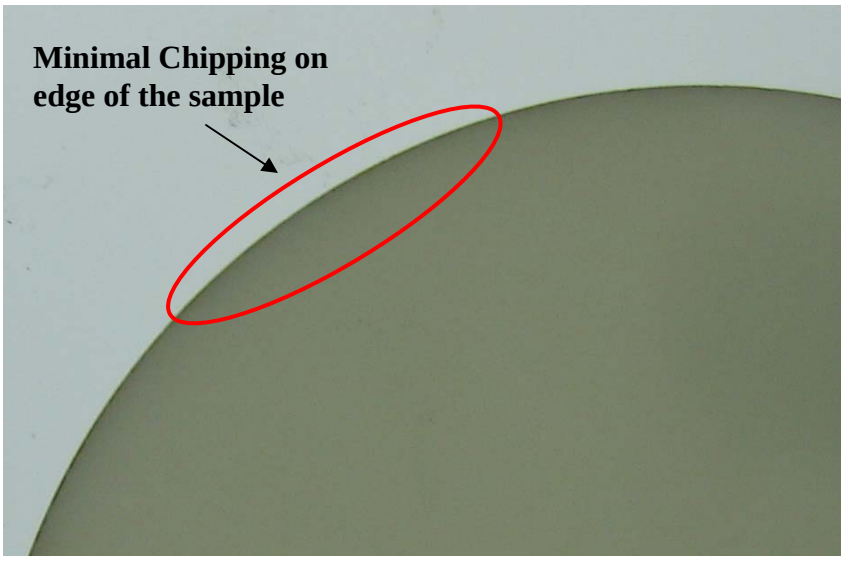

Figure 3.9: Edge of a circular PMN-PT sample cut using a UV Laser drill

The UV laser drill is a viable option for fabricating circular samples from thin PMN-PT wafers since it causes less damage to the samples. However, this is an expensive process and is most economical only when samples are prepared in batch as in a production facility. The flexibility rendered for fabricating samples of any desired shape and size also makes it an excellent option over mechanical coring drill bits.

After the PMN-PT discs were cored from wafers, a fine layer of gold (approximately – 100 nm) was deposited on the PMN-PT discs for contacts. The samples were then poled with electric fields of 250-350 V/mm. The poling field was dependent on the composition and phase of the PMN-PT samples. The dielectric constant of the poled samples was measured using a 7600 QuadTech precision LCR meter. The variation of dielectric constant and poling fields with the composition of the PMN-PT samples will be discussed in more detail in a later chapter.

Circular brass shims of different thicknesses were used as the non-piezoelectric substrate layer for PMN-PT unimorphs. The surface of the brass shims was roughened on

one side using a 600 grit SiC abrasive paper. The brass shims were then rinsed with ethyl alcohol. The PMN-PT discs were bonded to the brass substrate using a thin layer (approximately – 50 μm) of silver epoxy H20E from EPO-TEK. The PMN-PT epoxied to brass was placed between two glass slides and pressed with a force of approximately 0.3 psi. The epoxy bond was cured by heating it to 60-70 C for 10 hours. Lead wires were attached to the brass and the PMN-PT ends using a fast curing silver epoxy or cold solder (M.G. Chemicals: Cat. No. 8331-14G). The unimorphs fabricated were then analyzed using an impedance analyzer to study the resonance modes. The Figure 3.10a shows a fabricated PMN-PT unimorph on brass substrate while Figure 3.10b shows a batch unimorphs being fabricated. The steps for fabrication of PMN-PT unimorphs was optimized upon numerous investigations and is summarized in a flowchart in Figure 3.11.

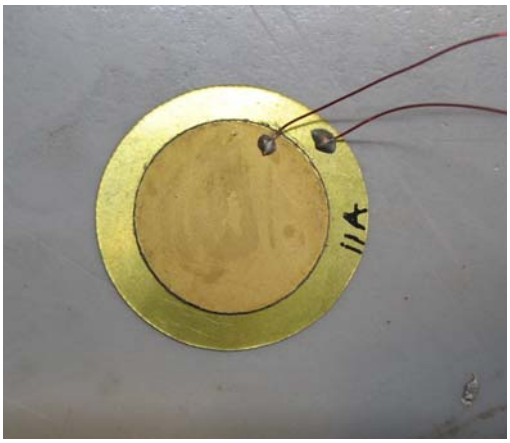

a) PMN-PT unimorph on brass substrate with lead wires

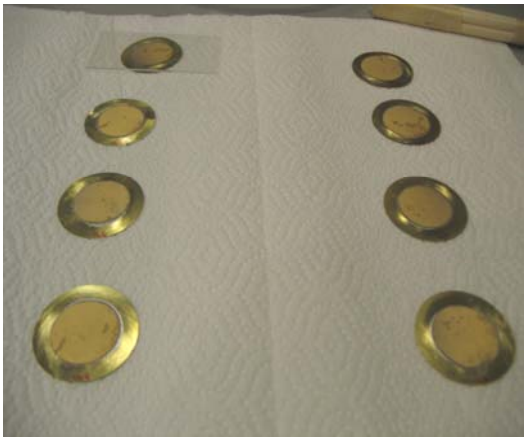

b) Batch of PMN-PT on brass unimorph being prepared

Figure 3.10: Fabricated PMN-PT on brass unimorphs.

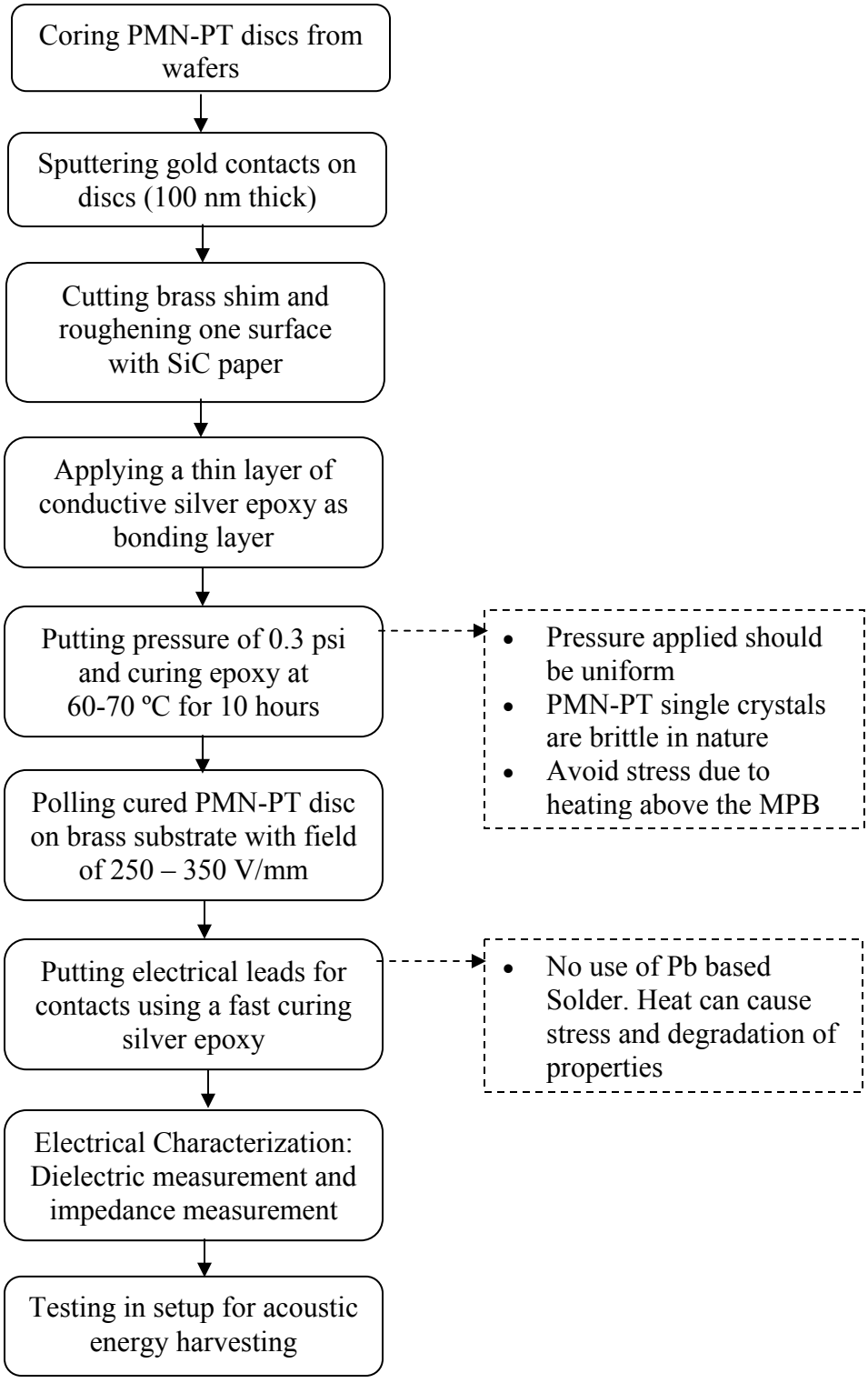

Figure 3.11: Flowchart for fabrication of PMN-PT unimorphs

3.4 Characterization Processes

In this section, the experimental methods for characterization of the PMN-PT unimorphs are presented. As discussed earlier, the material exhibits piezoelectric behavior once it is poled with a suitable electrical field. The dielectric constant at room temperature undergoes a change upon poling due to the re-alignment of the existing dipoles. The degree of piezoelectric behavior and the coupling constants of the samples can be determined by resonance mode impedance measurements on the sample.

3.4.1 Dielectric Measurement

Dielectric Constant, K, is used to determine the ability of a material to store electrical energy and is the ratio of the permittivity of the material, ε^*, to that of vacuum, ε°, as shown in equation 3.1. For anisotropic crystals like *(1-x)*PMN – *x*PT, the dielectric constant depends on both the composition phase and the orientation of the crystal [7, 8]. The dissipation factor, *DF*, is defined as the reciprocal of the ratio between the material's capacitive reactance to its resistance at any specified frequency. It measures the inefficiency or loss of energy in the material and *(1-x)*PMN – *x*PT has a very low dielectric loss than conventional piezoelectric ceramics.

$$\mathrm{K} = \frac{\varepsilon^*}{\varepsilon^\circ} \tag{3.1}$$

The permittivity of the material is a complex quantity and has a real and an imaginary part, see equation 3.2. The dissipation factor or dielectric loss is defined as the ratio of the imaginary to the real part, see equation 3.3.

$$\varepsilon^* = \varepsilon' - j\varepsilon'' \tag{3.2}$$

$$DF = \tan\delta = \frac{\varepsilon''}{\varepsilon'} \tag{3.3}$$

The dielectric constant was determined by a QuadTech 7600 Precision LCR meter. The temperature dependence of dielectric constant was also studied to determine the Curie temperature (T_c) of the *(1-x)*PMN – *x*PT samples. The temperature was controlled in a Tenney Environmental chamber with a working range of -60 ºC to 200º C. The metalized crystal surface area and thickness are paramount to the determination of the numerical dielectric constant.

The evolution of the phase diagram of *(1-x)*PMN – *x*PT has been discussed in an earlier section 2.2. The Curie temperature of *(1-x)*PMN – *x*PT or the paraelectric to ferroelectric transition varied linearly with the composition variation or %PT in the single crystal sample as shown in Figure 3.12. The fitted curve to the phase diagram shown in the plot was used for determining the approximate crystal composition from the Curie temperature. Figure 3.13 shows a typical plot of the variation of dielectric constant with temperature for two samples taken from different part of the ingot. The Curie temperature, T_C, is determined by the peak position of the ferroelectric to paraelectric phase transition curve on the temperature scale. There is another phase transition T_R (rhombohedral to tetragonal) at a much lower temperature due to the curved shape around MPB composition. This is due to the reorientation of polarization domains into a different macroscopic symmetry at the lower temperature phase transition. The low temperature phase transition is shown as a bend in the dielectric curve, see Figure 3.13. The dielectric constant measurement and corresponding composition of *(1-x)*PMN – *x*PT unimorphs are presented in detail in later sections.

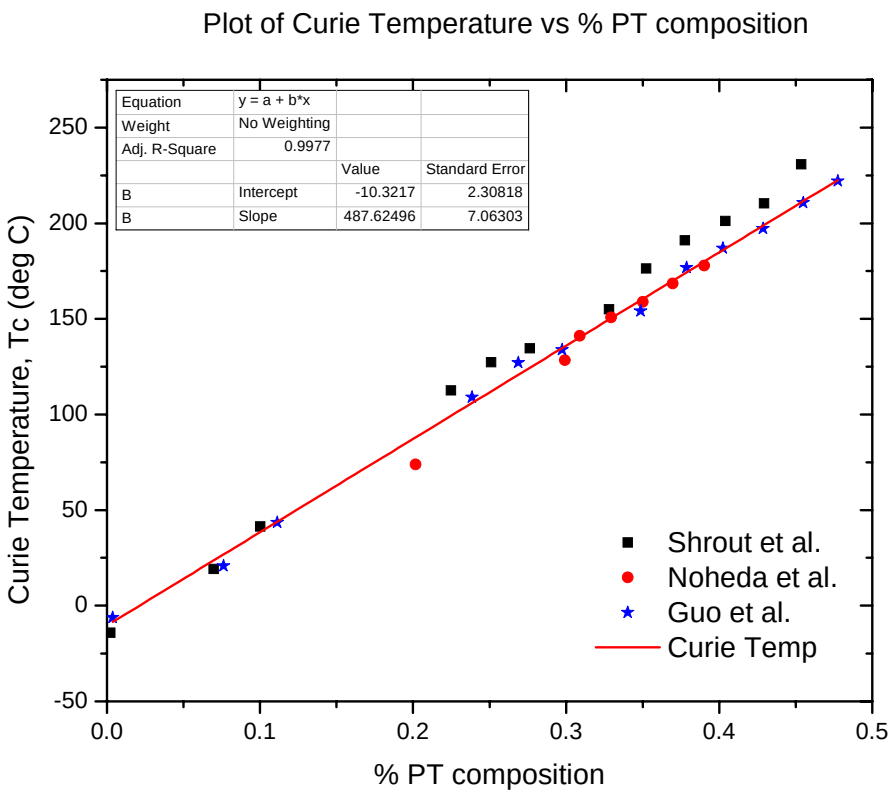

Figure 3.12: Variation of Curie temperature with x = %PT in *(1-x)*PMN – xPT

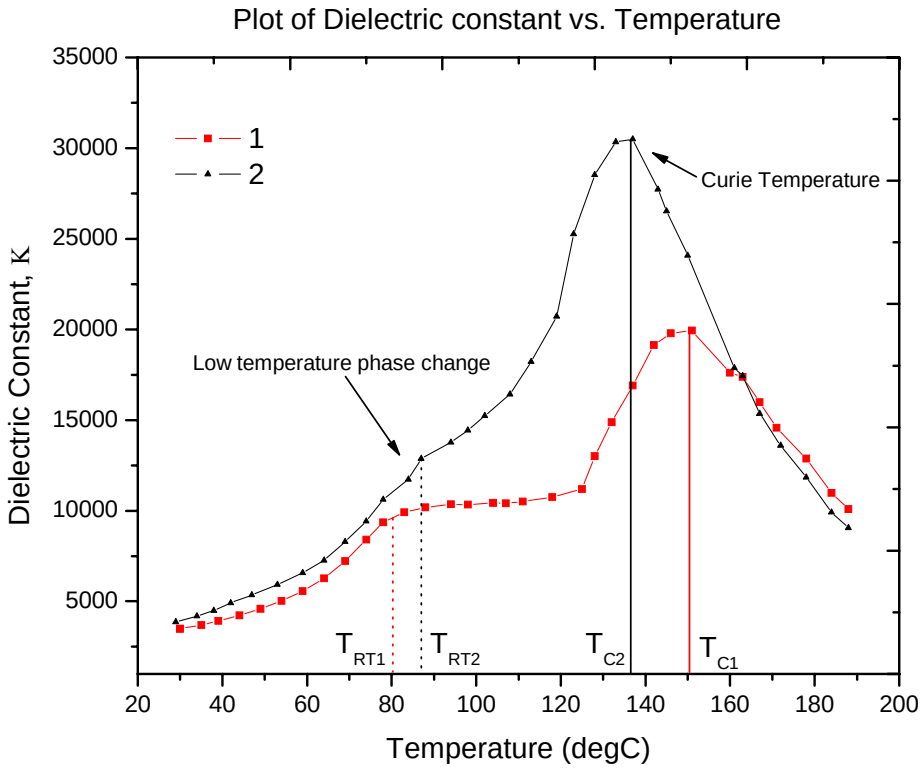

Figure 3.13: Typical plot of dielectric constant with temperature for two *(1-x)*PMN – *x*PT crystal samples. The x = %PT can be determined from their respective Curie temperatures. The low temperature phase transition is shown by the bend in the dielectric curve.

Sample – 1: T_{C1} = 152 ºC; x = 34.3 % PT

Sample – 2: T_{C2} = 137 ºC; x = 31.1 % PT

(Both samples are from same PMN-PT ingot and are discs of 25.4 mm diameter and 0.2 ± 0.01 mm thickness)

3.4.2 Poling of PMN-PT Crystals

Below the Curie temperature, dipoles are created in the PMN-PT relaxor ferroelectrics due to formation of non-centrosymmetric crystal phases depending on the segregation of PT in the ingot. These spontaneously created dipoles are randomly oriented within the various single crystal phases. The process of poling involves aligning or rotation of the individual dipoles resulting in a net dipole moment of the macroscopic crystal. By applying a constant DC electric field across the PMN-PT crystals, the dipoles align to a preferred direction and hence the crystal shows a net polarization even after the electric field has been removed. Figure 3.14 shows a schematic of the poling process.

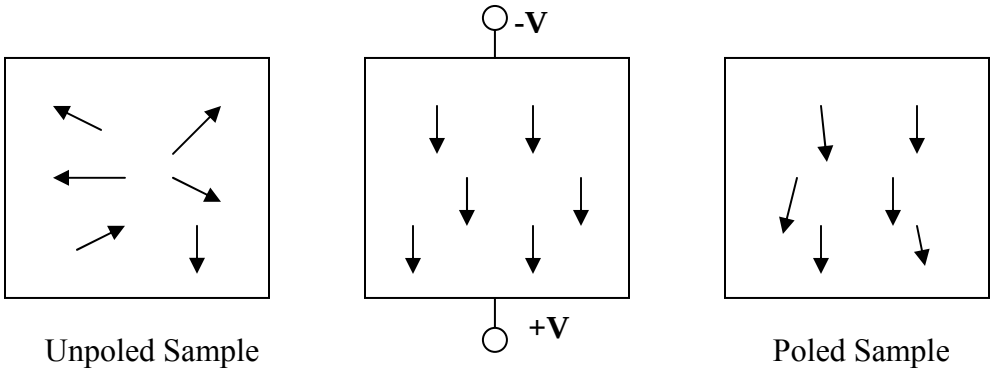

Figure 3.14: Schematic of the poling process of a piezoelectric sample

The setup used for poling the crystals consisted of a horizontal sample holder stage connected by two probes. A BERTRAN Series 225 power supply was connected in series to the sample with a KEITHLEY 486 pico-ammeter for measuring the current through the sample. The DC poling field was calculated by the voltage applied from the power supply over the thickness of the sample. The poling field was increased in steps and the voltage and current measurements were collected using a GPIB interface

connected to a workstation. During poling the sample was immersed in an insulating fluid bath which acted as a heat sink. This prevented the sample from cracking due to the thermal stress generated upon poling. Figure 3.15 shows the setup used for poling PMN-PT samples.

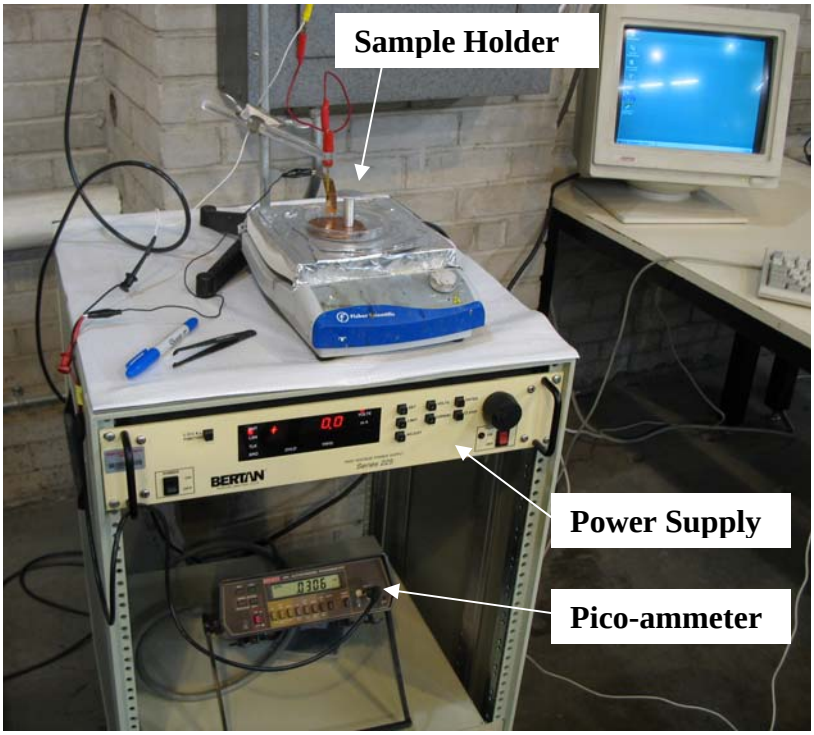

Figure 3.15: Poling setup used for poling PMN-PT samples

3.4.3 Impedance Measurement

Impedance measurement is important for active devices and this technique is used to determine the resonant frequency, bandwidth and the electromechanical coupling factors of piezoelectric materials. Impedance, *Z*, is generally defined as the total opposition a device or circuit offers to the flow of a small signal alternating current (AC) at a given frequency. Impedance consists of a real part, *R*, and an imaginary part, *X*, while admittance is defined as the inverse of impedance. The unit of impedance is ohms (Ω) while the unit of admittance is Siemen (S). The relations are shown in equation 3.4.

$$Z = \frac{1}{Y} = R + jX = \frac{1}{G + jB} \tag{3.4}$$

where, Y = Admittance, G = Conductance and B = Susceptance

The phase angle, theta θ, between the impedance and its real part is given as:

$$\theta = \tan^{-1}\left(\frac{X}{R}\right) \tag{3.5}$$

A HP 4194A impedance analyzer instrument was used for measuring impedance of the sample. A small value A.C. signal with zero bias was used for measuring the impedance, *Z*, or the admittance, *Y*, along with the phase angle, *θ*. for the single crystals

A *(1-x)*PMN – *x*PT piezoelectric element when exposed to an AC field changes dimensions cyclically over a certain frequency range. The frequency at which the element vibrates most readily in response to the electrical input and most efficiently converts the electrical energy input into mechanical energy is called the *resonance frequency,* f_r. It is determined by a combination of several parameters such as the composition of the *(1-x)*PMN - *x*PT material and the shape and dimensions of the sample. During a frequency sweep of the small signal AC field, the impedance is minimum (maximum admittance) at

the resonant frequency. At a slightly higher frequency, the impedance increases to a maximum (minimum admittance) which also is known as the *anti-resonance frequency,* f_a. The values for minimum impedance frequency and maximum impedance frequency can be used to calculate the *electromechanical coupling factor*, *k*, which depends on the mode of vibration and the shape of the sample. Equations 3.6 – 3.8 lists the different formulas used for calculating the electromechanical coupling factors from the resonance of the single crystals without a substrate. In Figure 3.16 a typical admittance plot with frequency is shown for a PMN-PT crystal mounted on brass. The resonant frequency was 2.28 kHz while the anti-resonant frequency was 2.52 kHz. More details about the derivation and constraints of the coupling coefficient can be found in IEEE Standard [10].

For planar discs,

$$k_p = \sqrt{\frac{2.51(f_a - f_r)}{f_a} - \left(\frac{f_a - f_r}{f_a}\right)^2} \tag{3.6}$$

For plates,

$$k_{31} = \sqrt{\frac{(\pi/2)(\frac{f_a}{f_r}) * \tan\left[(\pi/2)\left(\frac{f_a - f_r}{f_r}\right)\right]}{1 + (\pi/2)(\frac{f_a}{f_r}) * \tan\left[(\pi/2)\left(\frac{f_a - f_r}{f_r}\right)\right]}} \tag{3.7}$$

For bars and rods,

$$k_{33} = \sqrt{(\pi/2)(\frac{f_r}{f_a}) * \tan\left[(\pi/2)\left(\frac{f_a - f_r}{f_a}\right)\right]} \tag{3.8}$$

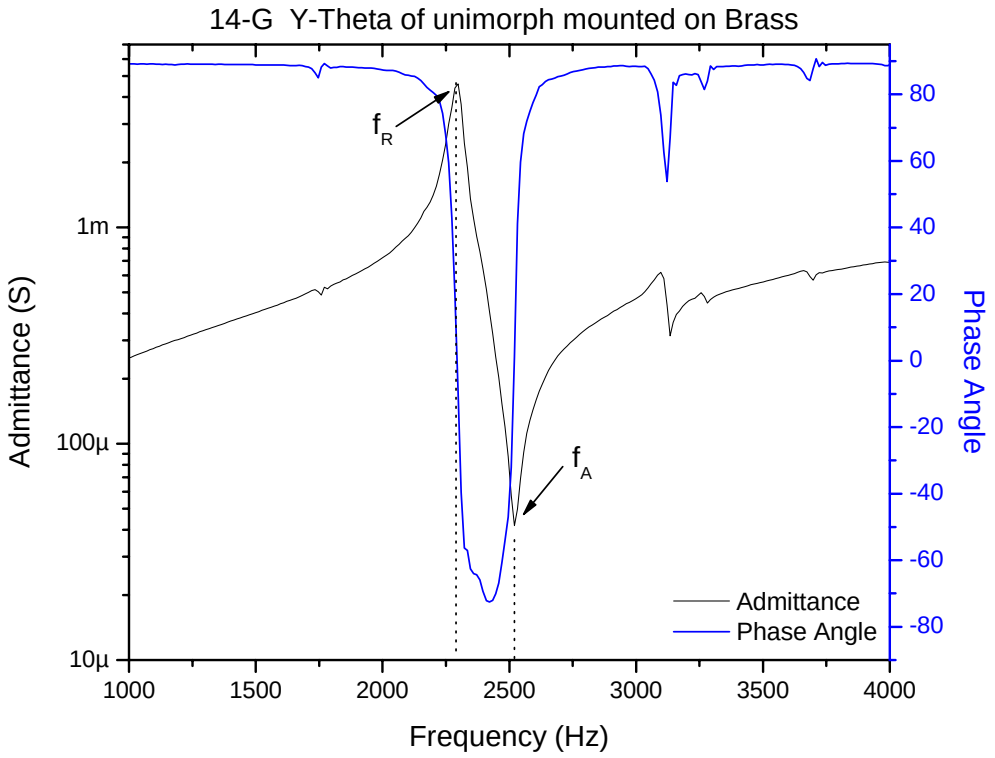

Figure 3.16: Typical impedance plot of admittance (Y) and phase angle with a frequency sweep for a unimorph mounted on brass.

Diameter of unimorph – 25.4 mm

Thickness of PMN-PT – 0.19 ± 0.01 mm

3.4.4 Orientation Imaging Microscopy

Orientation imaging microscopy (OIM) was used extensively to investigate the crystal orientation of single crystal material [11]. For *(1-x)*PMN – *x*PT, the material properties vary with orientation of different crystal phases. OIM is done by indexing the electron back-scatter diffraction or EBSD patterns which are produced when an electron beam interacts with the sample surface. In a FESEM, an electron beam sets up an omni-directional source of scattered electrons within a specimen. Diffraction of these electrons occur simultaneously on all lattice planes in the sample and the back-scattered electrons (BSE) which escape from the sample form diffraction patterns that can be imaged on a phosphor screen. This is the basis of the EBSD technique which is used to obtain the crystallographic orientation of materials. Details of the EBSD procedure can be found in literature elsewhere.

At room temperature, the morphotropy of the *(1-x)*PMN – *x*PT depends on the composition or "*x*". However, the non-centro symmetric phases at room temperature have pseudocubic structure and can be oriented with a cubic lattice to a fair degree of accuracy. For using the OIM imaging technique effectively a smooth and polished crystal surface (polished down to 0.3 μm alumina suspensions) is required for a good diffraction pattern [12]. Often the errors of the magnitude of 2-4 degrees can originate from improper mounting of the sample or reference or improper beam parameters and imaging technique. The collection of EBSD pattern in the SEM is done using a phorphor screen detector. The mounted sample is tilted to a relatively high angle (typically 70°) inside the SEM. The electron beam is then focused at the point of inspection on the sample surface. The initial elastic scattering of the incident beam causes the electrons to diverge from a

point just below the sample surface and to impinge upon crystal planes in all directions. Figure 3.17 shows a schematic of backscatter electron diffraction. The pole figure plot showing the orientation for some unimorph samples would be presented in the next chapter.

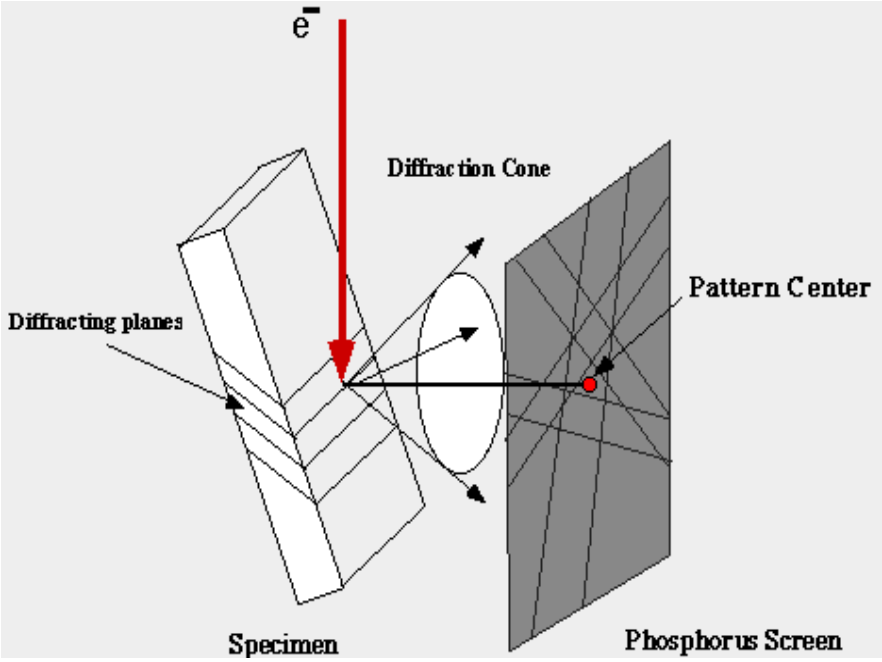

Figure 3.17: Schematic of EBSD technique

(The red line shows the incident electron beam. The lines formed on the phosphor screen are called the Kikuchi bands)

References

[1] Uchino K., Yoshizaki M., Kasai K., Yamamura H., Sakai N. and Asakura H., "Monomorph Actuators: Using semiconductive ferroelectrics", Japanese Journal of Applied Physics, 26 (7), 1987, pp. 1046-1049.

[2] Mo C., Wright R., Slaughter W. S. and Clark W. W., "Behavior of a Unimorph Circular Piezoelectric Actuator", Journal of Smart Materials and Structures, 15, 2006, pp. 1094-1102.

[3] C. Mo, Radziemski L. J. and Clark W. W., "Analysis of PMN-PT and PZT circular diaphragm energy harvesters for use in implantable medical devices," Proceedings of SPIE on Active and Passive Smart Structures and Integrated Systems, 6525, 2007, pp. 652507-1:9.

[4] Soundararajan R., Das R.N., Tjossem R., Bandyopadhyay A., Lynn K.G., Eissler E.E. and Lazaroff J., "Growth and characterization of single-crystal PMN–PT via HPVB method", Journal of Materials Research, 19(2), 2004, pp. 609-615.

[5] Hoffman Materials LLC., http://www.hoffmanmaterials.com, Carlisle, PA, USA.

[6] Microconnex, http://www.microconnex.com, Snoqualmie, WA, USA.

[7] Benayad A., Sebald G., Guiffard B., Lebrun L., Guyomar D. and Pleska E., "Temperature dependence of piezoelectric properties of PMN-PT and PZN-PT single crystals", Journal de Physique IV France, 126**,** 2005, pp. 53–57.

[8] Colla E.V., Yushin N.K. and Viehland D., "Dielectric properties of $PMN_{(1-x)}$-PT_x single crystals for various electrical and thermal histories", Journal of Applied Physics, 83 (6), 1998, pp. 3298-3304.

[9] Choi S.W., Shrout T.R., Jang S. J. and Bhalla A. S., "Dielectric and pyroelectric properties in the $Pb(Mg_{1/3}Nb_{2/3})O_3$-$PbTiO_3$ system", Ferroelectrics, 100 (1), 1989, pp. 29-38.

[10] IEEE Standard on Piezoelectricity, ANSI/IEEE Std. 176-1987, Page – 46.

[11] Adam Schwartz, Mukul Kumar, David Field and Brent Adams, "Electron Backscatter Diffraction in materials Science", ISBN 0-306-46487-X.

[12] Specimen preparation for EBSD analysis, http://new.ametek.com/content-manager/files/EDX/specimenpreparation.pdf, EDAX Inc.

CHAPTER – 4

ACOUSTIC EXCITATION

Acoustic excitation is the process of inducing mechanical vibrations to a structure by incident sound waves in the audible frequency range. Piezoelectric materials are used both for sound generation e.g. piezoelectric buzzers and active noise cancellation and sound pickup e.g. electric guitar, microphone elements [1]. In this work, research was focused on an application where sound energy from a source in the bandwidth of 1.5 – 3.5 kHz was converted to electric power in near resonant mode operation. The sound excitation could be derived from a thermo-acoustic engine driven from waste heat or can be acoustic noised filter device modulated to a suitable frequency. The experimental setups used and the resulting power output are presented in this chapter.

4.1 Piezoelectric-Acoustic Coupling

There are distinctly three different ways to mount a piezoelectric unimorph element on a resonator cavity:

1) Center mount
2) Nodal mount
3) Edge mount

The edge mounting can also have two possible clamping scenarios: a) rigid clamping on the edge of the unimorph and b) a flexible mounting on the edge. The different types of mounts are presented in a schematic in Figure 4.1. The typical deflection patterns of the fundamental tone are shown by the dotted line for each of the cases. It should be noted that the deflections and the unimorphs are not to scale.

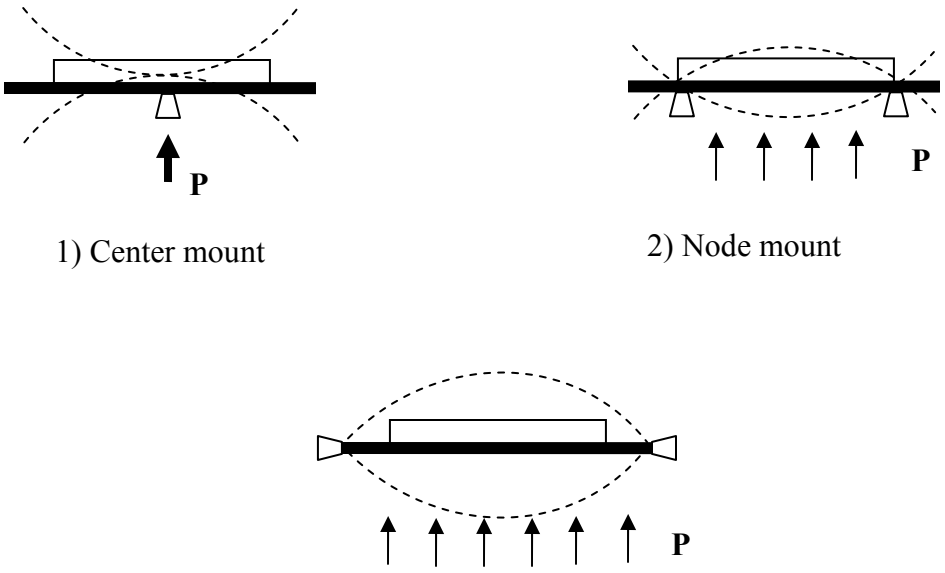

1) Center mount

2) Node mount

3) Edge mount

Figure 4.1: Types of scenarios for mounting a unimorph on a resonator (**P** is the acoustic loading of the unimorph structure)

The center mount permits the outer rim of the unimorph to vibrate while the edge mount permits the whole unimorph to vibrate. Reports in the literature suggest that the nodal mount performs best at near resonant frequency loud tone of acoustic loading [2, 3]. The edge mount is difficult to achieve as rigid mounting on edge dampens the unimorph vibration and hence the performance. In the experiments presented in this thesis, we have tested the performance of the fabricated *(1-x)*PMN – *x*PT unimorphs on both the center mounting and nodal mounting scenarios. The experimental setups are presented in the following sections.

4.2 Center Mounting Experiment

A set of *(1-x)*PMN – *x*PT unimorphs was tested with a center mounting setup where the acoustic excitation was provided by a speaker. The current set of unimorphs were fabricated with different brass thickness for determining the optimum thickness ratio and tested with the setup.

4.2.1 Setup with Cone

A high performance speaker from JBL (model no. 2426) was used as a monochromatic sound source for the acoustic excitation experiments. The speaker had a stable output (SPL) in the higher frequency range (> 1500 Hz) and was driven by a sine wave input from a bi-polar amplifier connected to an arbitrary function generator. Experiments were performed in the audible frequency range (1.0 – 3.5 kHz) to determine the resonant frequency of the structure. The unimorphs were center mounted on a paper cone and then the maximum power output at resonance was investigated. The unimorphs were glued to paper cones by a double sided adhesive copper tape and then centered over the speaker. Adhesive Scotch tape was used to hold the paper cone in a fixed position over the speaker. Figure 4.2 shows the schematic of the setup and the dimensions in greater detail. The paper cones directed the sound energy to the center of the unimorph structure as in the center mount schematic shown in Figure 4.1. The unimorph was facing downward towards the excitation source in this set of experiments. The JBL speaker had a D.C. resistance of 3.3 ± 0.3 ohms at 25 ºC and has a crossover 12 dB per octave below 800 Hz. The detailed specification is listed in Appendix 2.1.

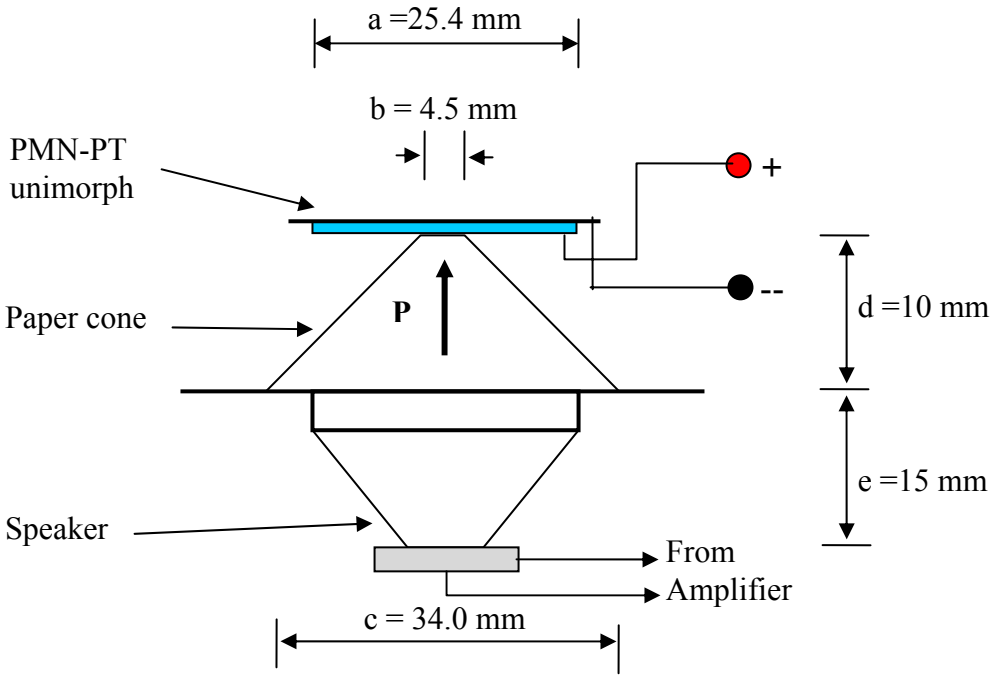

Figure 4.2**:** Schematic of the center mount energy harvesting setup

a = diameter of unimorph;

b = inner diameter of paper cone;

c = outer diameter of paper cone;

d = depth of paper cone;

e = depth of the speaker cone from voice coil;

4.2.2 Unimorphs for Center Mounting – Set-1

A total of 9 unimorphs were fabricated and tested for the power output. The nomenclature would be described as U-x, 'x' being an alpha-numeric identifier for a specific PMN – PT unimorph.

4.2.2.1 PMN-PT Ingot – P150

The *(1-x)*PMN – *x*PT ingot was grown by HPB technique at WSU with a starting composition of x = 0.3, i.e. 30% PT concentration. The ingot will be referred as P150 henceforth. The ingot was semi-round in shape: the diameter towards the top was 86 ± 1 mm and weighing 601 grams. Figure 4.3 shows the picture of the as grown P150 ingot. A vertical slice was taken on one edge of the ingot and the composition variation from growth was studied via the Curie temperature. Five rectangular samples were prepared from the regions as marked in Figure 4.4 and dielectric constant vs. the temperature was measured. The rectangular samples were coated with gold contacts and tested in the dielectric fixture. The samples were heated to 180 ºC first and cooled down to 25 ºC in steps of 5 ºC. Dielectric constant was measures at the various temperature set points. The plots of dielectric constant at 1.0 kHz for the samples S-1 to S-5 is shown in Figure 4.5.

The maximum composition variation is from the bottom-center of the ingot to the top-edge, approximately 13.5% PT for this specific ingot. But, the composition variation from top to the bottom at the center of the ingot was 5 – 6% PT. The samples for fabricating the unimorphs were taken from a crack free region marked within the red square in the slice in Figure 4.4.

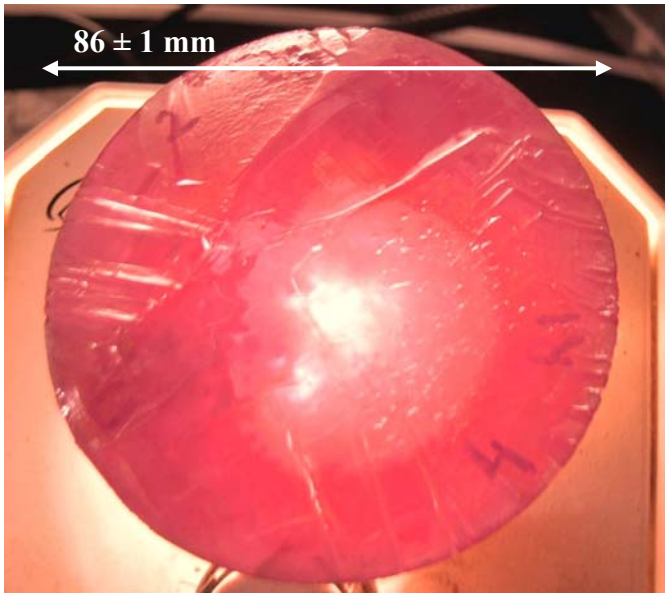

Figure 4.3: Top view of P150 ingot when held against bright white light

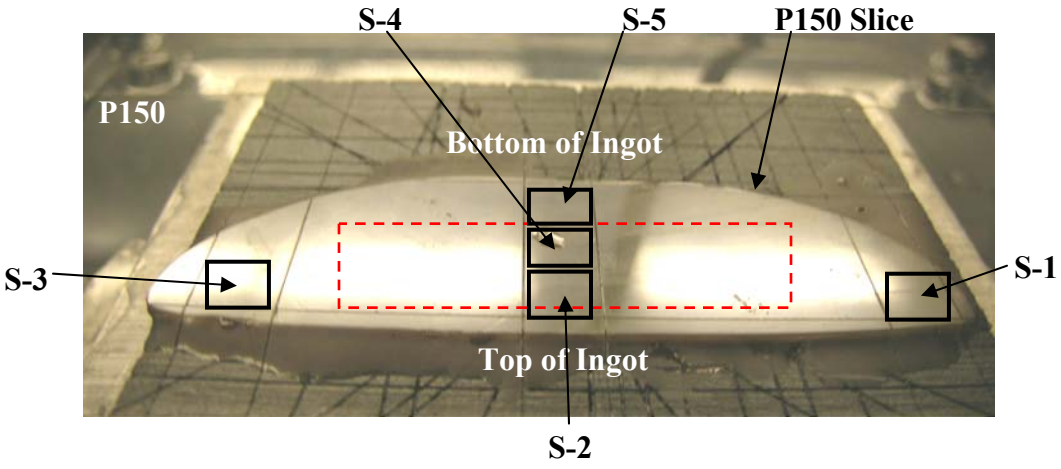

Figure 4.4: Layout of P150 slice for dielectric test

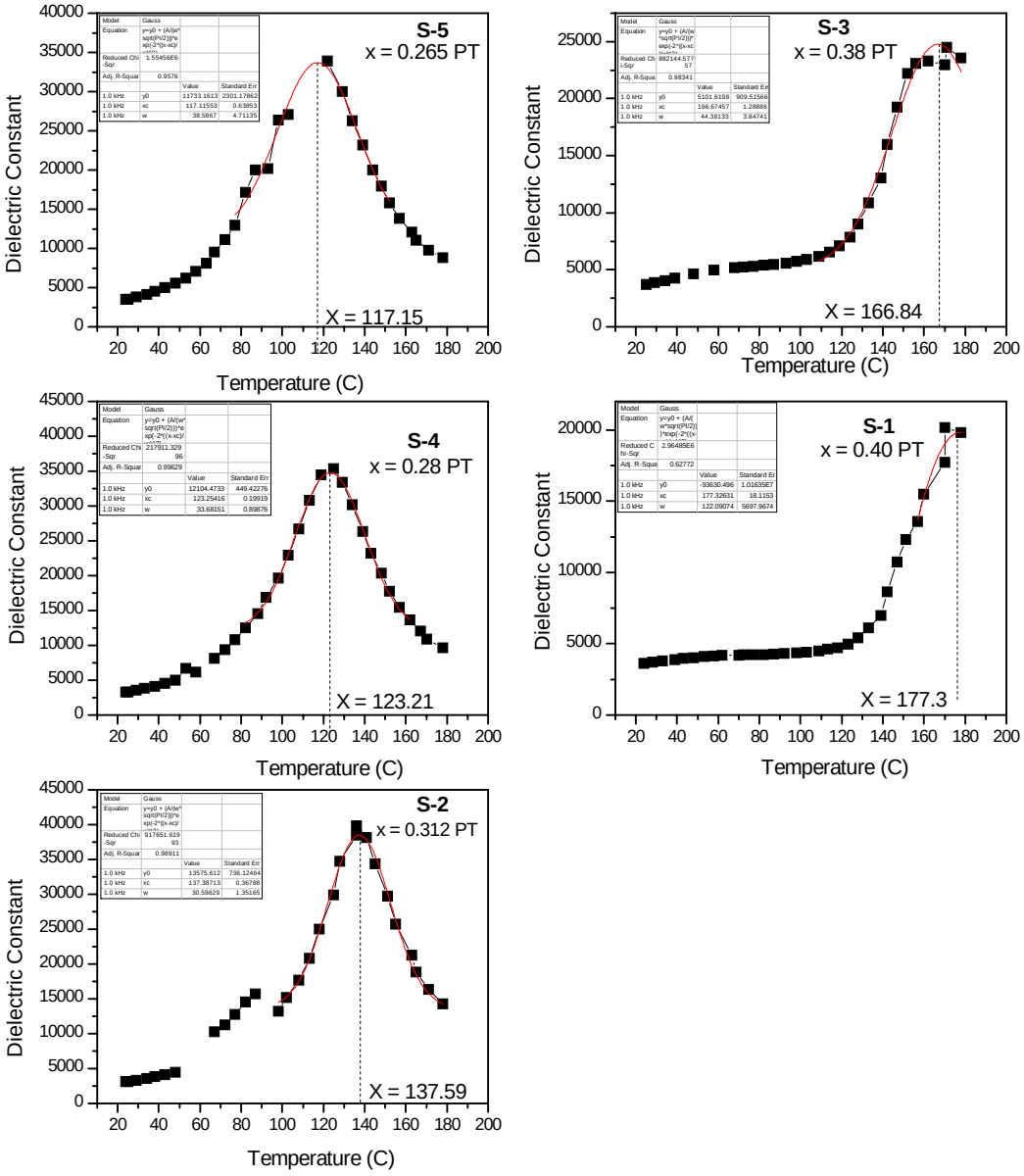

Figure 4.5: Curie temperature plots of samples from a vertical slice in ingot P150

4.2.2.2 Unimorph Parameters

The fabrication parameters of unimorphs (Set-1) are listed in the Table 4.1 below. The PMN – PT discs were cored from wafers from the P150 ingot for all the unimorphs below. The thickness of the PMN-PT wafers, h_p, was 0.19 ± 0.01 mm. The substrate for backplate was brass with the exception of U-14I and U-14J, where a more compliant graphite substrate was used. The thickness of the brass substrate, h_m, was varied in order to change the thickness ratio. The non-metallic graphite substrate for U-14I and U-14J was formed by bonding 2 single ply graphite sheets in a cross-ply pattern and heat treating in a furnace at 100 ºC for 1 hour with approximately 6.0 lbs of compressive weight. The thickness ratio and the area ratio are defined as in Equations 4.1 and 4.2.

$$\text{Thickness Ratio} = \frac{\text{Thickness of Piezoelectric disc} \quad (h_p)}{\text{Thickness of Substrate or Brass} \quad (h_m)} \tag{4.1}$$

$$\text{Area Ratio} = \frac{\text{Area of Piezoelectric disc} \quad (\pi.D_p^2/4)}{\text{Area of Substrate or Brass} \quad (\pi.D_m^2/4)} \tag{4.2}$$

where,

D_p = Diameter of PMN-PT disc

D_m = Diameter of substrate

The area ratio was kept constant for all the fabricated PMN-PT unimorphs and is presented below.

Area Ratio for PMN-PT Unimorphs = 0.444

Area Ratio for the PZT disc = 0.55

Table 4.1: Specification of Unimorphs Fabricated for Center Mount Excitation

Sample Name	Ingot	Substrate	Thickness of Substrate h_m (mm)	Thickness Ratio h_p/h_m	Diameter of Substrate D_m (mm)	Diameter of Piezo D_p (mm)
U-14B	P150	Brass	0.15	1.26	38.1	25.4
U-14C U-14D	P150	Brass	0.10	1.9	38.1	25.4
U-14E U-14F	P150	Brass	0.25	0.76	38.1	25.4
U-14G U-14H	P150	Brass	0.30	0.63	38.1	25.4
U-14I U-14J	P150	Graphite	0.40	0.475	38.1	25.4
PZT-Uni		Brass	0.25	~ 2.0	27.0	20.0

As mentioned above the unimorph samples were prepared from a single *(1-x)*PMN – *x*PT ingot with starting composition x = 0.3 or 30% PT. The dielectric constant for these PMN-PT samples after poling was calculated at 1.0 kHz from the admittance phase angle plots. The excitation signal was 0.5 V a.c. signal sweep from an Agilent HP4194 impedance analyzer. The dielectric constant for each unimorph is shown in Table 4.2. The diameter of the disc was 25.4 mm and the average thickness of all the samples was 0.19 ± 0.01 mm. The poling field required for poling a single crystal unimorph depends on its composition and hence a variation in poling field and the poling current is observed for each sample. The peak in the current vs. voltage plots indicates the completion of poling of the sample, as shown in Figure 4.6.

Table 4.2: Properties of PMN-PT Unimorphs Epoxied to Brass in Table 4.1

(Composition of PMN-PT unimorphs varied from 28 – 32% PT, Figure 4.5)

Sample Name	**Dielectric constant after poling (1kHz @ RT)**	**Poling Field (V/mm)**	**Applied Poling Field (V/mm)**	**Current when poled (μA)**
U-14B	1617	235	526	10.1
U-14C	1314	263	526	8.99
U-14D	1040	289	789	8.16
U-14E	1731	578	789	7.89
U-14F	1202	263	789	18.12
U-14G	1394	421	789	89.1
U-14H	1237	263	526	14.3

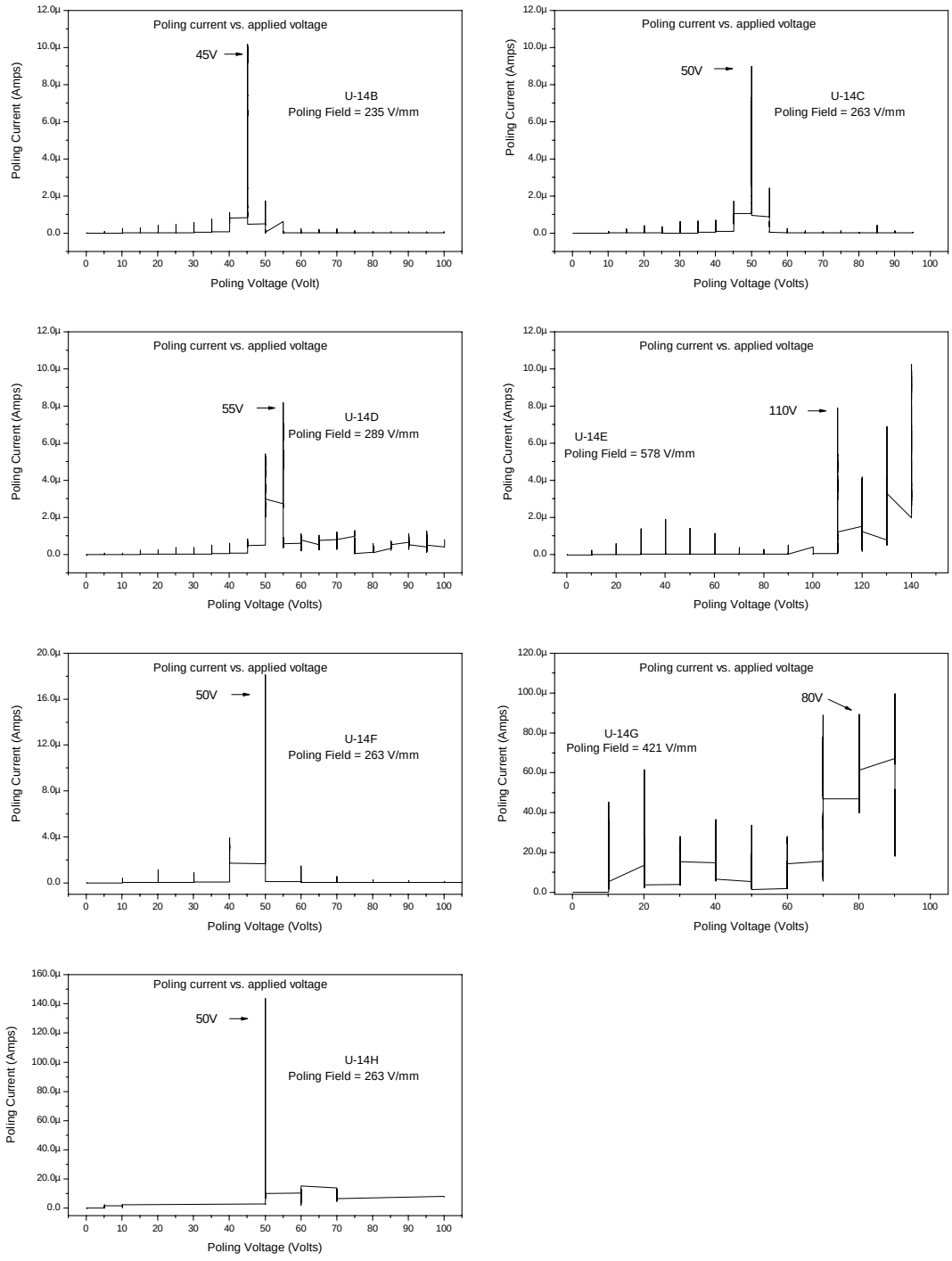

Figure 4.6: Poling graphs for the unimorphs of Set-1

(U-14B, U-14C, U-14D, U-14E, U-14F, U-14G and U-14H)

4.2.2.3 Orientation of PMN-PT discs of P150 ingot

The orientation of the wafers from P150 was studied by EBSD technique as discussed earlier in Chapter-3. A square sample was chosen from a wafer and mounted on a SEM stub. A reference sample of <111> single crystal Silicon (Si) was mounted on the same platter. A kikuchi pattern was obtained and indexed for Si which generated the pole figure as shown in Figure 4.7a. Each mark on TD and RD axis on the plot is of 1 degree. It was seen that the pattern was ~1.8 degrees off the TD axis for Si. Hence the Si pole figure was corrected for +1.8 degrees in TD, Figure 4.7b.

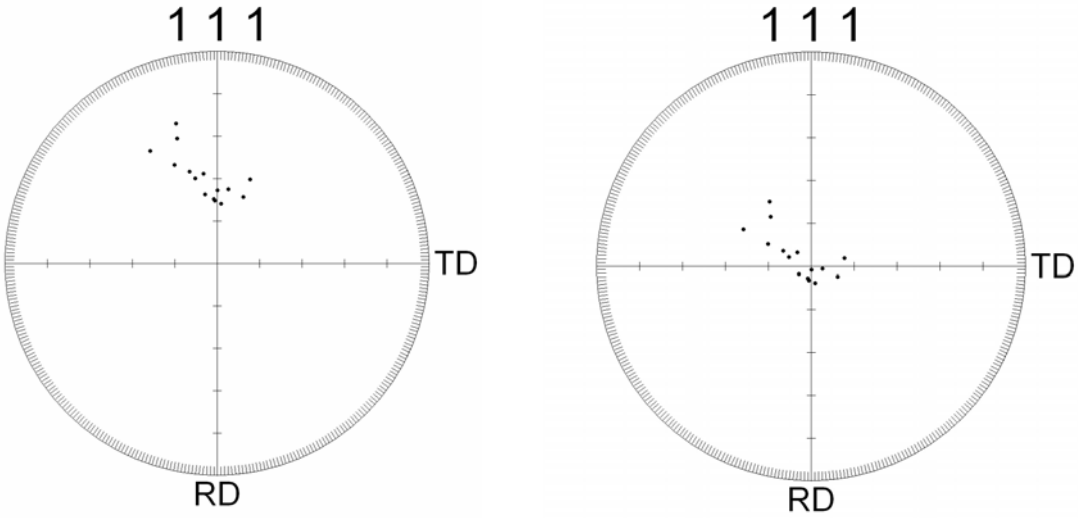

Original Data
(a)

After correction +1.8 deg TD
(b)

Figure 4.7: 10 degree <111> Pole figure of the reference <111> Silicon sample. The figure is zoomed in to see only 10 degrees on TD and RD axis near the center. Each mark on the TD and RD axis is 1 degree.

The orientation of the P150 PMN-PT wafer was measured at different spots on the wafer by indexing the Kikuchi patterns. After the correction for Silicon was done the following <001> pole figures were obtained, Figure 4.8. In this pole figure each scale on the axis is 10 degrees. The normal direction from the wafer was not in a major crystallographic direction. It was found to be closer to the <011> than <111>.

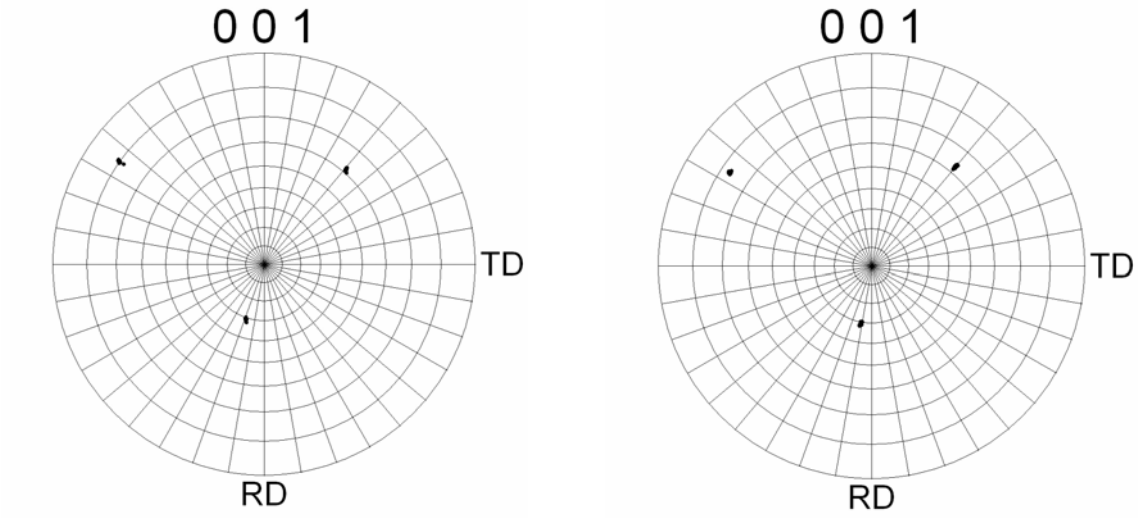

Pattern - 1 Pattern - 2

Figure 4.8: 180 degree <001> Pole figure plots of P150 wafer after the Si correction of +1.8 degrees. The polar scale is 10 degrees per division on each axis.

The pole figure of pattern-1 was matched and compared to a cubic (Pm3m) Wulff Net to find the closest pole to the center, Figure 4.9. It was observed that the surface normal of the wafer sample was <2 -1 4> direction.

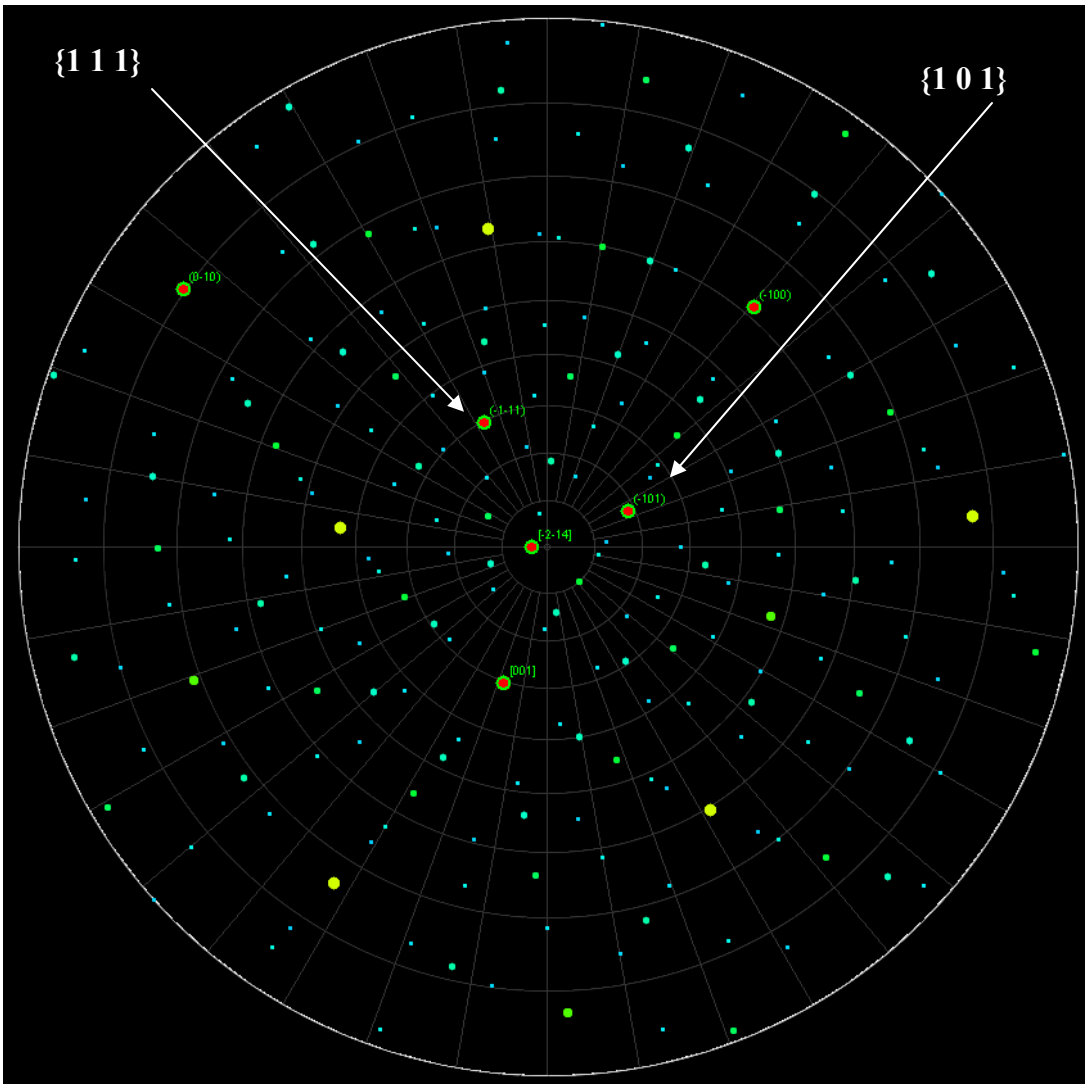

Figure 4.9: Wulff Net of pseudo-cubic crystal matched with Pattern-1 of Figure 4.8

The angular distance of the normal of (2 -1 4) plane from the (-1 0 1) plane was 18.1º while the (-1 -1 1) plane was 29.4º. The orientation of the crystal along <2 1 4> family during the growth was not expected and is still under investigation. The accuracy of the pole figure measurement can be stated within ± 2º due to sample mounting and the OIM pattern fitting. The PMN-PT discs for unimorphs were cored from the wafers and would have the <2 1 4> orientation.

4.2.3 Power Output Results

The maximum power transfer to the load resistance was at the resonant frequency of the coupled structure, i.e. unimorph with paper cone. The schematic passive circuit used for measuring continuous RMS output power is shown in Figure 4.10. The load resistance was 100 ohms. An inductor L_1 was connected in series to the load resistance R_L to tune the circuit. This increased the output power to the load resistor. The inductor coupled with the piezo element to form an electrical LC tuned circuit and hence there was an increase in RMS power. L_1 is also referred later as the tuning inductance and its value is dependent on the resonant frequency, the dielectric constant of the sample and thickness of the unimorphs. A 10 ohm shunt resistance, R_S, was used to determine the current through the circuit.

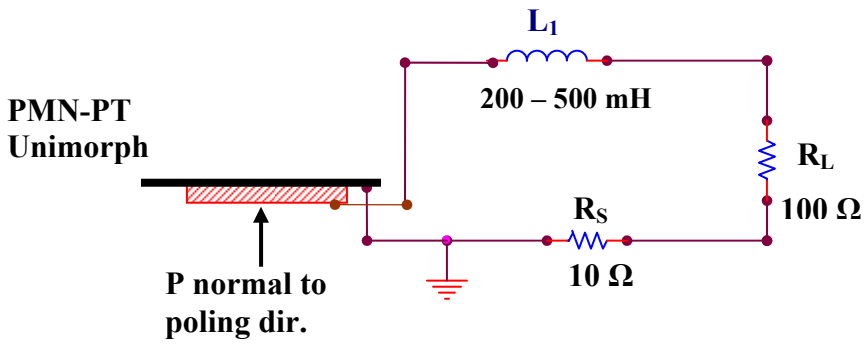

Figure 4.10: Schematic circuit used for measuring output power

The resonant frequency of the structure was determined by a frequency sweep to a 1 MΩ resistance. A typical output voltage with a frequency sweep is shown in Figure 4.11. Multiple peaks in the frequency sweep indicated the presence of harmonics in the resonating structure. The RMS output power was measured at the resonant frequency to a load resistance R_L of 100 ohms and a tuning inductor L_1 in a range 200 mH – 500 mH. Maximum RMS power from a unimorph was obtained at a certain impedance matched condition by changing the tuning inductor to an optimum value. The input from the function generator to the Kepco bi-polar amplifier was kept constant. A shunt circuit was also used in the input side to measure the electrical RMS power input to the speaker at the resonant frequency. The efficiency for this case, η_{elec}, was defined as overall efficiency of RMS power transduction from the input to the output of the harvester and as shown in Equation 4.3.

$$\text{Efficiency, } \eta_{elec} = \frac{\text{RMS power output from unimorph} \quad (P_{out})}{\text{RMS power input to speaker} \quad (P_{in})} \tag{4.3}$$

Figure 4.12 shows the RMS power output and the efficiency ratios for the unimorphs tested from Table 4.1 while Figure 4.13 shows the corresponding inductance L_1 in mH used for tuning at resonance. The PMN-PT unimorphs performed better than the PZT counterpart as seen from the efficiency plot. But due to the difference in dimension of the PZT unimorph tested a true metric for comparison would be power output per unit volume of the harvester. The power density calculation is shown in Table 4.3 below.

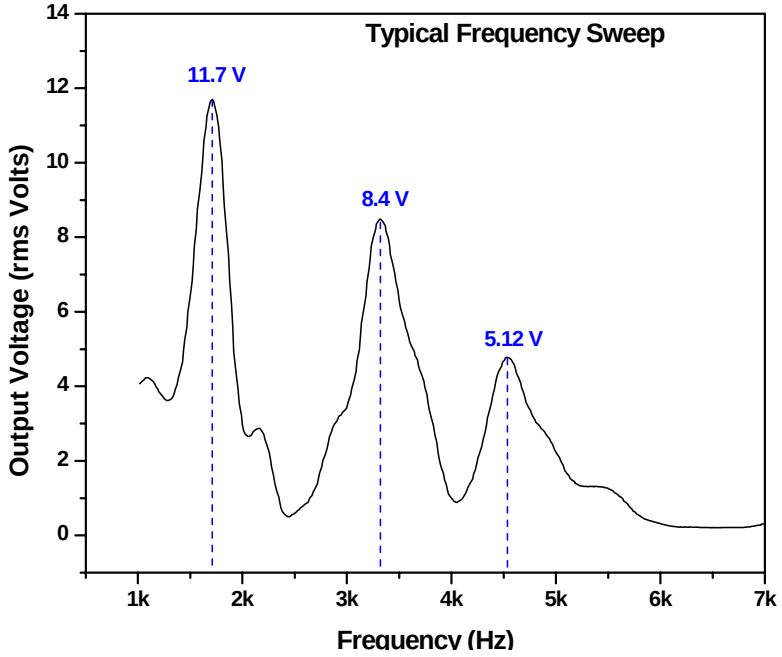

Figure 4.11: Frequency sweep for a typical unimorph showing resonances

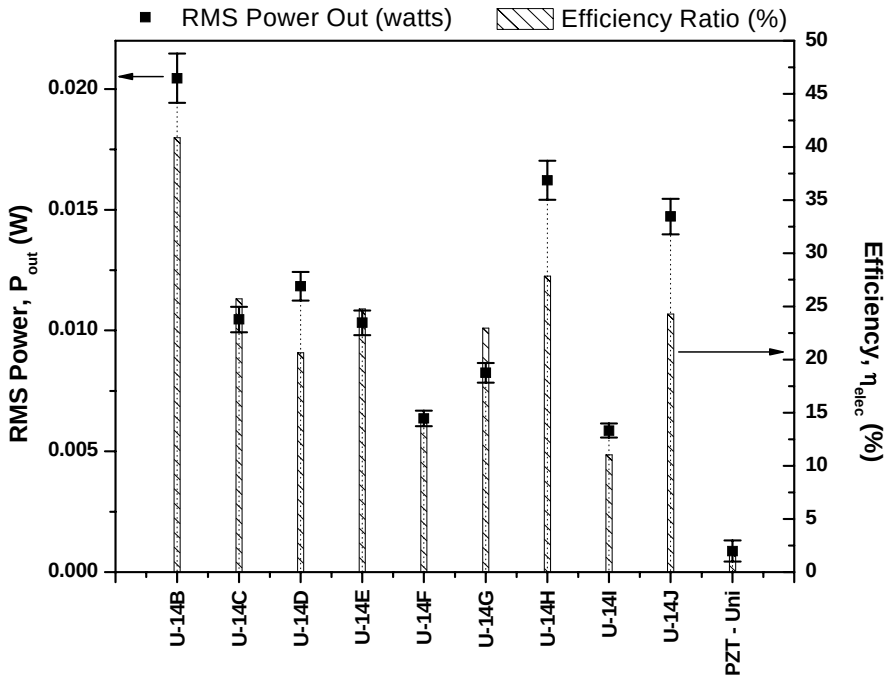

Figure 4.12: Power output and efficiency of center-mount unimorphs of Table 4.1

Table 4.3: Power Density Calculation for PMN-PT and PZT Unimorph for Center Mounting Setup (Composition varied from 28 – 32 % PT from Figure 4.5)

Unimorph No.	Resonant Frequency (kHz)	Volume (cm^3)	Power output (10^{-3} W)	Power Density (W/cm^3)
U-14B	1.71	0.0962 (Dia. = 2.54 cm thickness = 0.019 cm)	20.45	0.212
U-14C	1.63		10.46	0.108
U-14D	1.74		11.83	0.122
U-14E	1.53		10.32	0.107
U-14F	1.61		6.36	0.066
U-14G	1.66		8.25	0.085
U-14H	1.71		16.22	0.168
U-14I	1.73		5.86	0.061
U-14J	1.77		14.72	0.153
PZT-Uni	1.70	0.0392 (Dia. = 2.0 cm thickness = 0.0125 cm)	0.8702	0.022

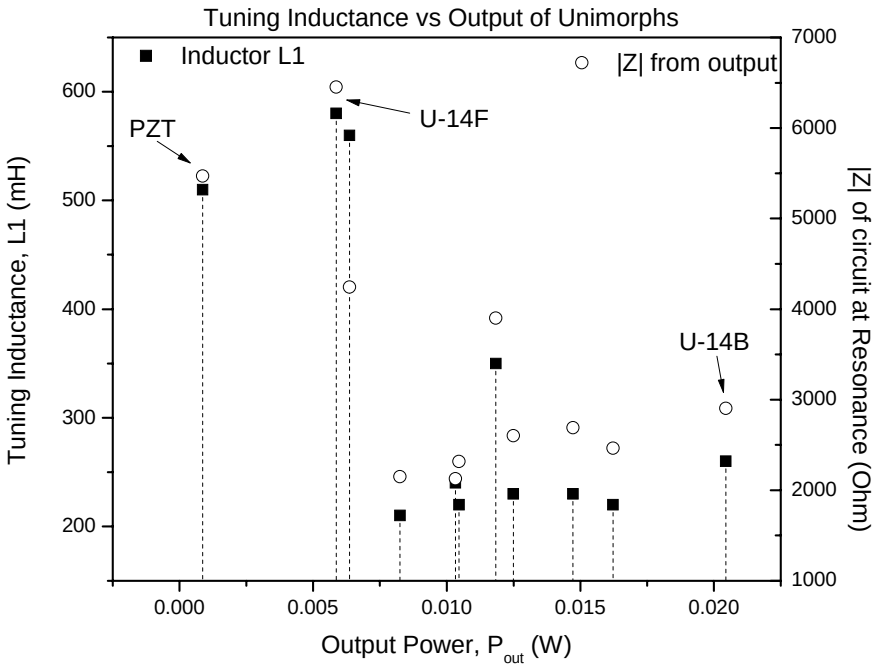

Figure 4.13: Tuning inductance for maximum power output for the center mount unimorphs of Table 4.1

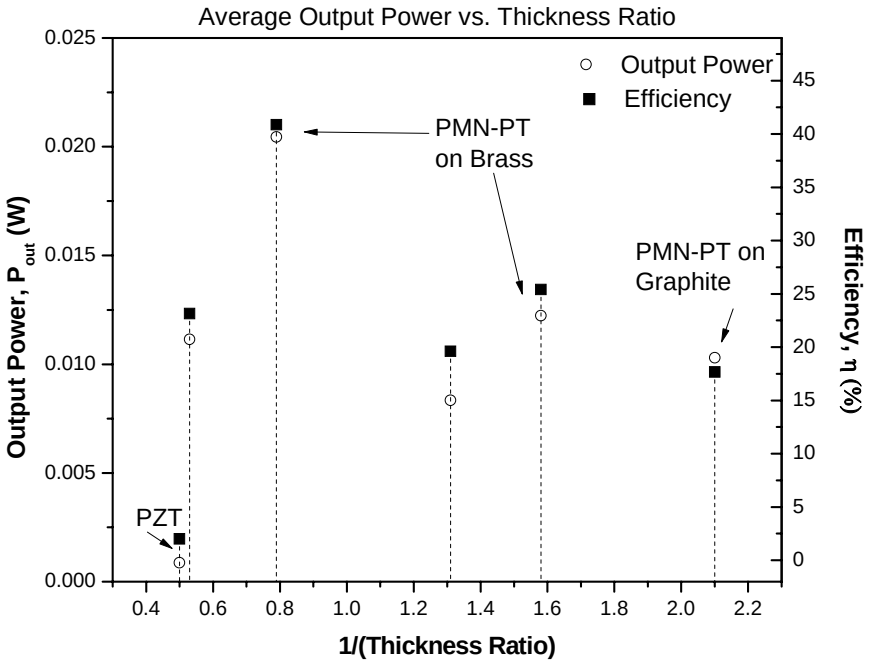

Figure 4.14: Efficiency and Power output of unimorphs with thickness ratio (Composition of PMN-PT unimorphs ranged from 28 - 32% PT, Figure 4.5)

The thickness ratio as defined in Equation 4.1 which gave the maximum output power was 1.26, Figure 4.14. For the best case, U-14B produced 20.45 mW and 40.8 % efficiency at resonant frequency of 1.71 kHz. A typical PZT unimorph (available commercially) produced 0.89 mW and 2 % efficiency at resonant frequency 1.7 kHz. The accuracy of the frequency measurement in the oscilloscope was within ±5Hz of the input from the function generator. From the power density calculations in Table 4.3, it can be seen that the best case performance was about 9 times that of the PZT while for the worst case it was approximately 3 times better. It was observed that for the two worst cases, U-14F and U-14I, the required tuning inductance was high for the maximum output power.

4.2.4 SPL Measurement

The measurement of the sound pressure level (SPL) and the acoustic power is complex as the distance of the unimorph from the sound source is small and enters the near field region of the source. In the near field region the sound intensity is not inversely proportional to the square of the distance [5]. Also the sensitivity of the compression driver with frequency has to be taken into account. Upon the assumption of the speaker as a point source, the near field distance r_o can be calculated from equation 4.4.

$$r_o = \frac{1}{k} = \frac{c}{2\pi f} \tag{4.4}$$

where, r_o = Distance from source

k = Wave number

c = Velocity of sound in air at room temperature

f = Frequency of sound

Considering velocity of sound as 345 m/s at experimental conditions, the near field boundary for 1.7 kHz frequency is 32 mm. The distance of the center from the dome of the speaker was 25 mm which falls within the near field boundary. Hence the on-axis SPL was measured at 2.5 kHz and 43.9 mm from top of the speaker, while the input power to the speaker was doubled in steps. Although the conditions were not truly far-field where the point of measurement of sound pressure has to be several wavelengths from the source, the response was far field like with approximately 3dB linear increase on doubling the input power and is shown in Figure 4.15. The 2.5 kHz frequency for measurement was chosen due to the maximum sensitivity of the speaker and to reduce the effect of near field acoustics. The sound pressure was calculated at the actual resonant frequency of unimorph using the sensitivity of the speaker which was linearized, - 0.0026

dB/Hz till 1.6kHz. The acoustic power and the efficiency of the speaker ($\eta_{speaker}$) can be then calculated as equations 4.5 and 4.6 respectively shown below [4].

$$SPL = 20\log\left(\frac{\sqrt{\frac{P_{ac}.\rho.c}{2.\pi.r^2}}}{p_0}\right) \tag{4.5}$$

where, SPL = Sound pressure level in dB

P_{ac} = Acoustic power (W)

$\rho.c$ = Specific acoustic impedance of air ($kgm^{-2}s^{-1}$)

r = Distance on-axis from sound source

p_0 = Reference acoustic pressure (20 μPa)

Efficiency of Speaker , $$\eta_{Speaker} = \frac{P_{ac}}{P_{in}} \tag{4.6}$$

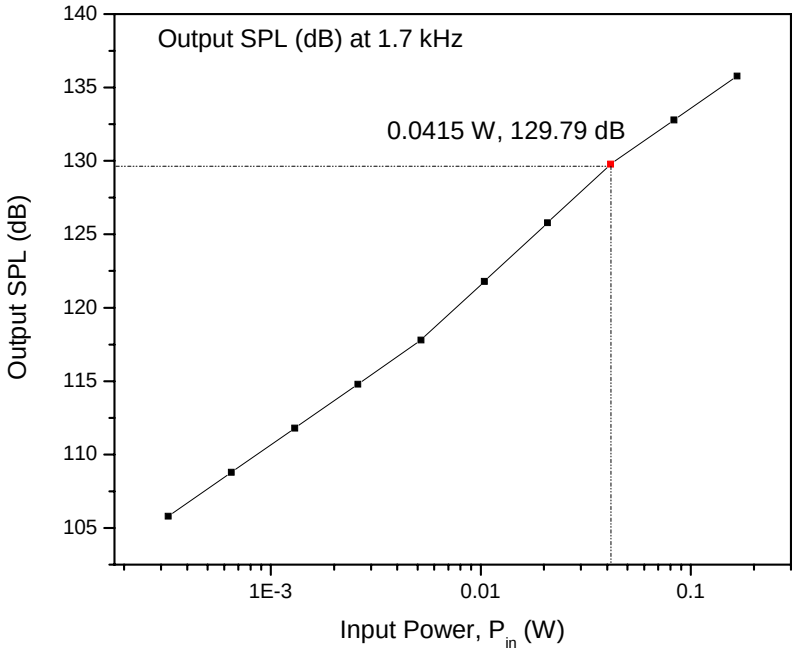

Figure 4.15: On-axis SPL with corresponding input electrical power at 1.7 kHz and 25 mm

The measurements were a good approximation of the far field condition as effects of energy loss within the near field was neglected. A more detailed measurement needs to be done for calculating the exact sound intensity in near field, where pressure and particle velocity are not in-phase, and is beyond the scope of this work. Table 4.4 shows the approximate acoustic power from the speaker calculated for the PMN-PT and PZT unimorphs tested. It can be seen that the calculated efficiency of the speaker is between 85 – 87% on-axis neglecting near field effects. The efficiency presented earlier in Figure 4.14 is the actual measured efficiency with respect to the input power.

Table 4.4: Power Output Comparison for the PMN-PT and PZT Unimorph

Unimorph No.	Measured SPL [1] (dB)	Input Power [1] (10^{-3} W)	Acoustic Power [2] (10^{-3} W)	Output Power [1] (10^{-3} W)	Power Density (W/cm^3)
U-14B	130.44	50.02	42.4	20.45	0.212
PZT-Uni	129.95	43.5	37.87	0.8702	0.022

[1] Measured Quantity; [2] Calculated Quantity

4.2.5 Summary

The findings of the above experiment in section 4.2 are summarized below.

1. The maximum output power was realized when ratio of thickness of PMN-PT to thickness of brass was 1.26 and ratio of area of piezo to area of brass was 0.44.
2. The bonding layer or thickness of epoxy adds to the stiffness of the bender structure and was also important for making a functional device with a

significant power output. Typically, the bonding layer thickness varied within 70 - 100 microns for all samples. This was achieved after developing a technique over multiple samples. The variation in epoxy thickness and gluing add a smaller degree of variation in performance due to the alteration of the effective stiffness.

3. It was observed that a higher value of tuning inductance, L_1 at resonance yielded less output power. This corresponds to the unimorphs U-14F and U-14I which had higher impedance at resonance. This results mainly from the variation of material properties of PMN-PT element and to some extent fabrication defects. The PZT unimorph tested also had higher impedance and hence required a larger tuning inductance at resonance.
4. The piezoelectric properties of *(1-x)*PMN – *x*PT single crystal vary with composition variation or %PT which results during the growth of the crystal from melt. Thus samples rendered from different parts of the ingot had different dielectric and piezoelectric properties.
5. OIM results revealed that the above tested single crystals samples were cut close to [214] direction which is 18º±2.5º off the preferred <011> direction.
6. The interpolated SPL measurements showed an acoustic excitation of approximately 129-131 dB for the unimorphs tested in this experimental setup. Near field effects were neglected.

4.3 Node Mounting Experiment

A different setup was built for the unimorphs with node mounting as shown in Figure 4.1. A cylindrical tube was used as an acoustic resonator cavity upon which the unimorphs were mounted. The following sections discuss the experimental setup and the energy harvesting results. It should be mentioned here that a different set of PMN-PT unimorphs were fabricated and characterized. However, the fabrication technique and characterization steps followed are similar to the process developed in Chapter 3 and discussed earlier in section 4.2. The effect of different parameters was also studied and will be presented in detail in Chapter-5.

4.3.1 Setup with Tube

The *(1-x)*PMN – *x*PT unimorphs were fabricated with the single crystal discs epoxied onto brass shims. The unimorphs were then mounted on brass washers with raised inner lips for node mounting. Figure 4.16a shows a fabricated brass washer while the sketch in Figure 4.16b shows the dimensions. A thin coating of DAP Silicone© sealant was used on the lips of the brass washer to glue the unimorphs. After the unimorph was centered, a weight of about 100 gms was placed above the unimorph and was kept at room temperature for 24 hours. A stainless steel O-ring with two notches for the electrical leads was placed on top of the unimorph and acted as a spacer. It fitted into a groove on the washer which kept it centered and prevented any lateral motion due to vibration. Finally, a stainless steel flange was kept on top of the steel ring as a cap, and a 1500 g dead weight was placed on top of the flange to effectively clamp the system. The whole assembly is described schematically in Figure 4.17.

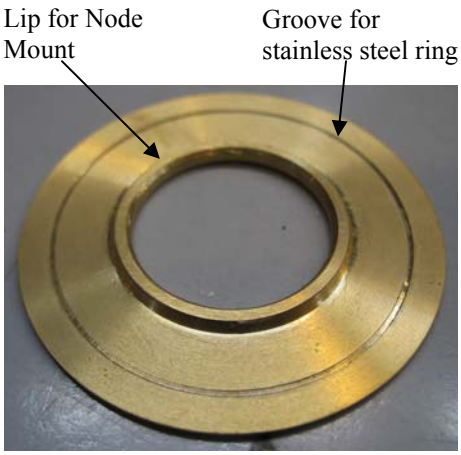

Figure 4.16a: Brass washer used for node mounting

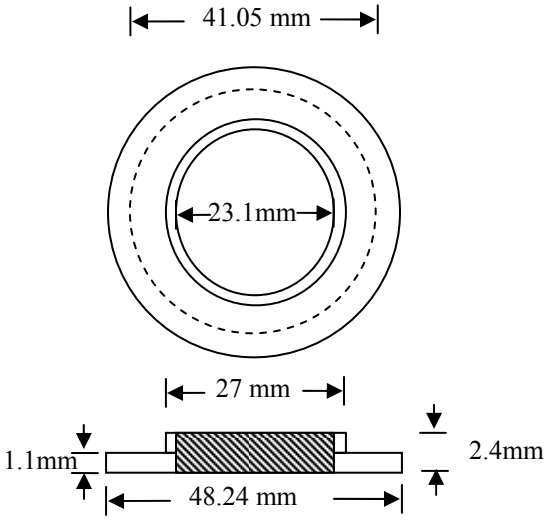

Figure 4.16b: Specifications of the Brass washer

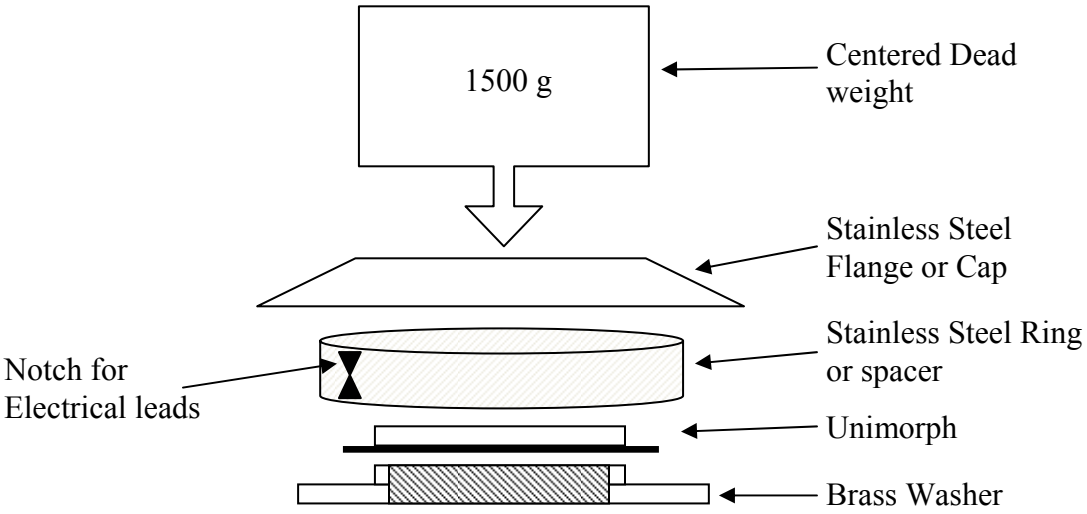

Figure 4.17: Schematic of unimorph node mount assembly (not to scale)

The same JBL 2426H speaker was used for acoustic excitation. However, the tube resonator was clamped to the speaker using a base plate and Teflon bolts. On the top side of the tube, another grooved plate was added to hold the unimorph-brass washer assembly centered with respect to the tube opening. Figure 4.18 shows the acoustic tube setup and the respective parts while Figure 4.19 shows a schematic with the input and output circuits for the experiment.

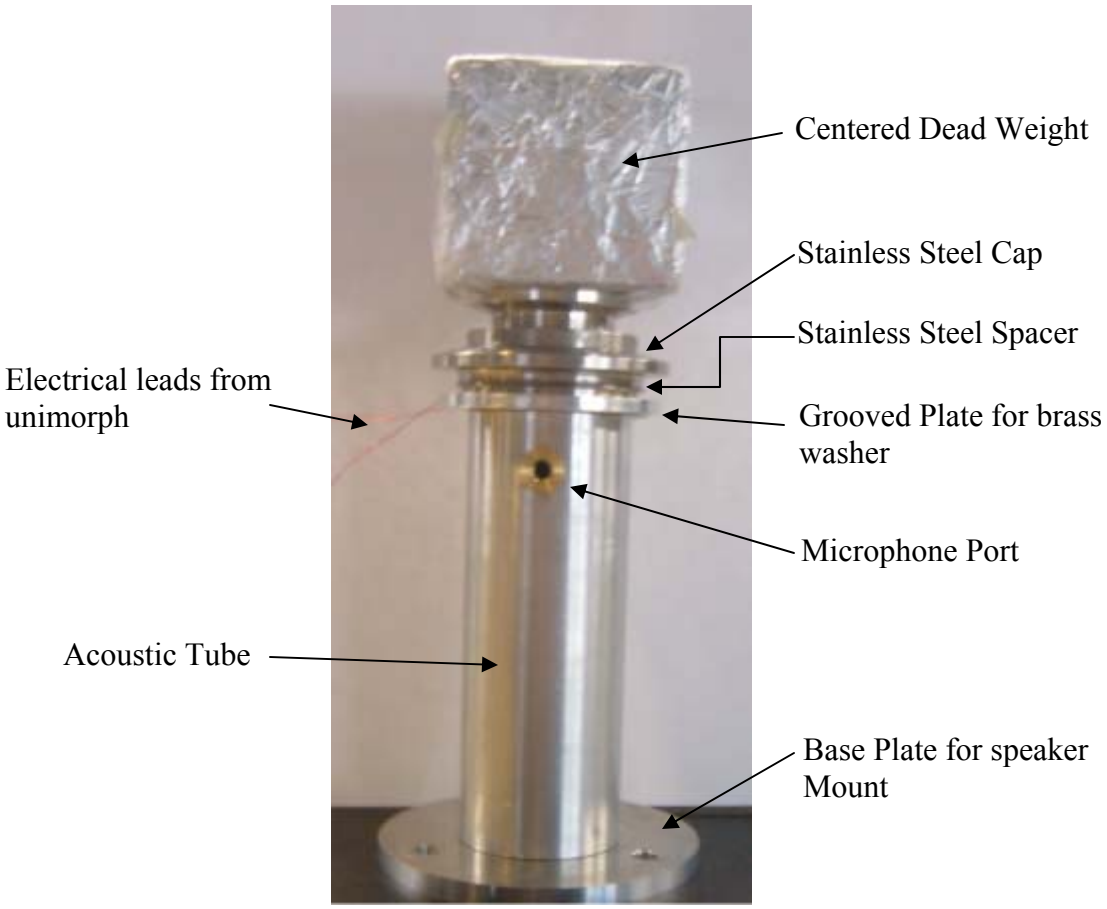

Figure 4.18: Acoustic tube setup for unimorph testing

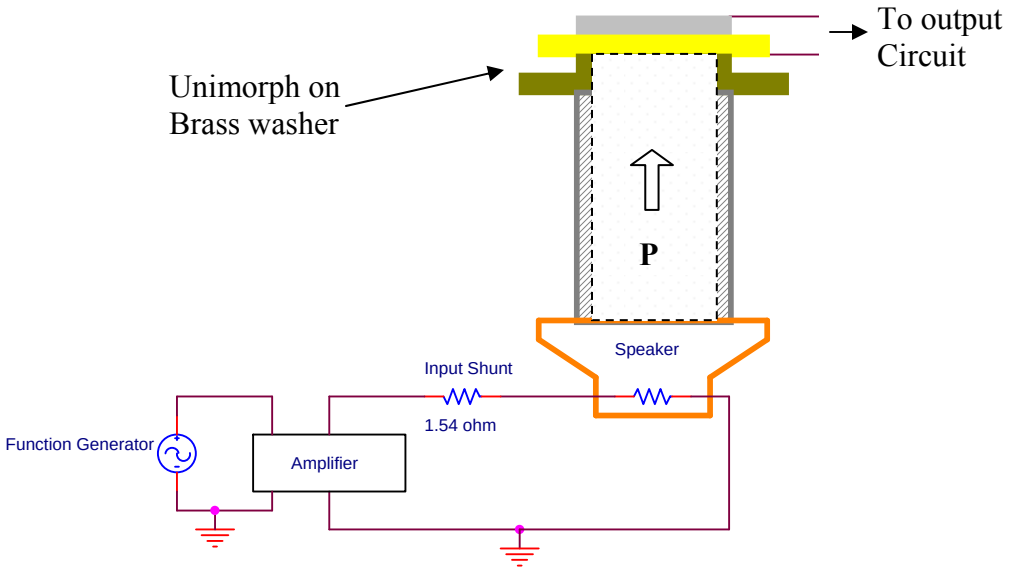

Figure 4.19: Schematic of node mounted unimorph on acoustic tube with input circuit and output, P is acoustic pressure

(A Kepco bi-polar amplifier was used for input to speaker in current control mode)

4.3.2 Unimorphs for Node Mounting – Set-2

A number of unimorphs were fabricated from a different *(1-x)*PMN – *x*PT ingot for these set of experiments. The unimorph identifier would be similar as before with the notation of U-x, where 'x' is an alpha-numeric character.

4.3.2.1 PMN-PT Ingot – X28

The specific *(1-x)*PMN – *x*PT ingot was also grown using the HPB method, with starting x = 0.32 or 32% PT concentration. This ingot was used for fabricating the set of unimorphs and will be referred as X28 hence forth. The ingot was semi-round in shape: the diameter towards the top was 115 ± 1 mm and weighing 1818 grams. Figure 4.20 shows the picture of the X28 ingot from top illuminated with white light on the back.

The X28 ingot was sliced into thin wafers of 0.19 ± 0.01 mm thickness perpendicular to the growth direction as shown in Figure 4.21, using a multi-wire saw. Figure 4.22 shows a single PMN-PT wafer. It cracked through the center on a pre-existing crack from growth during the slicing process. The red circular marks on the wafer are the regions where discs were cut via the UV Laser as described in Chapter 3. Discs of different diameter were cored from the wafer. The 25.4 mm diameter discs were used for fabricating the unimorphs while the 6.35 mm smaller discs were used as coupons for dielectric testing. The green marks on the wafer shows regions with some cracks or defects and was avoided during machining of discs. The wafers were numbered from top to the bottom of the ingot in an increasing order in order to keep a track of the position where each sample was derived from the ingot and subsequently its composition.

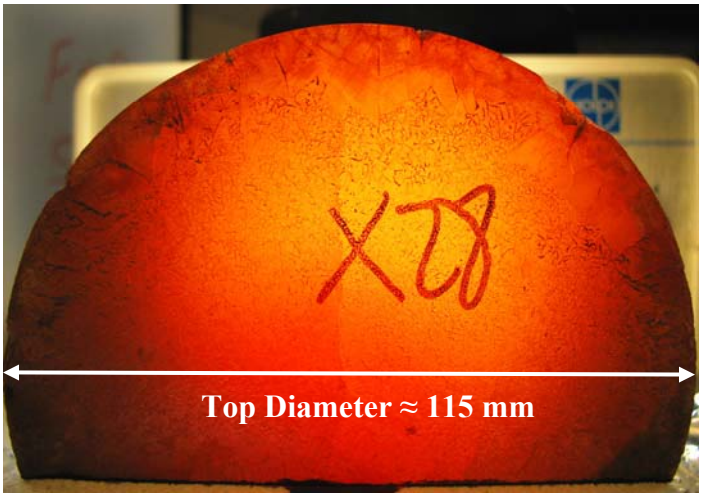

Figure 4.20: Top view of X28 ingot when held against white light

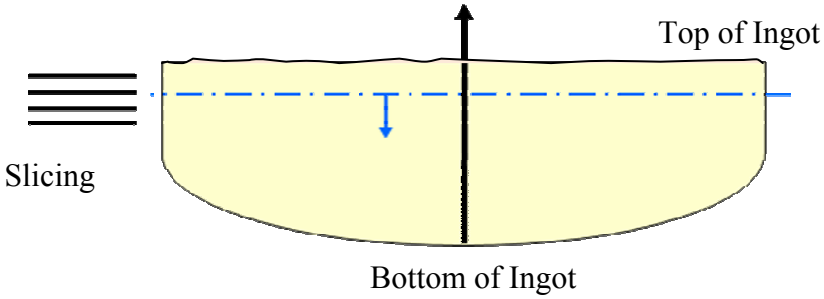

Figure 4.21: Schematic of slicing direction of X28 ingot

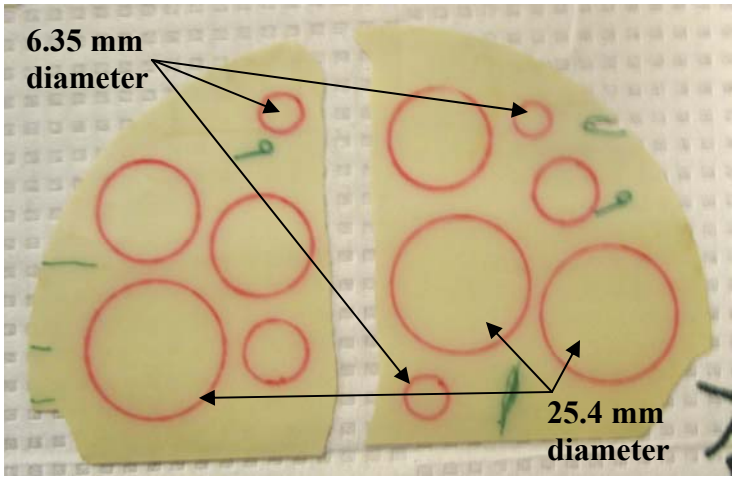

Figure 4.22: Sliced wafer from X28 ingot cracked through the center

Three 6.35 mm PMN-PT discs or coupons from a single wafer were sputtered with gold contacts and the dielectric measurement was studied with temperature. The composition variation across the X28 ingot was determined and it was seen that the variation increased exponentially towards the top of the ingot. Figure 4.23 shows the composition variation across the wafers for X28 ingot. The Curie temperature, T_C, was measured for each coupon from the wafer and then the average T_C was deduced and hence the corresponding average %PT composition of the wafer as mentioned in Section 3.4.1. The unpoled dielectric constant is measured at room temperature with a 1.0 kHz a.c. signal.

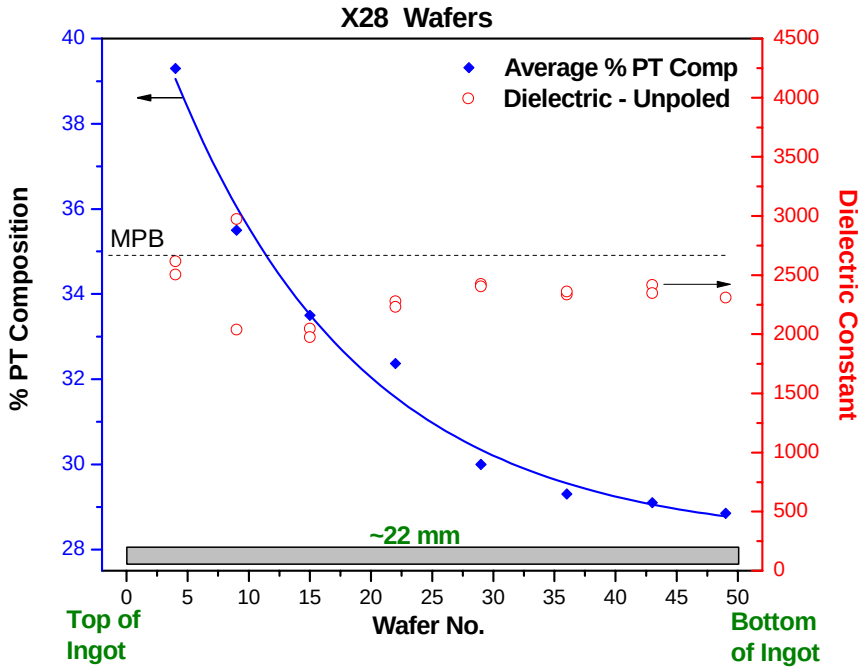

Figure 4.23: Composition variation of PMN-PT wafers across the X28 ingot from Curie temperature measurement and phase diagram

4.3.2.2 Unimorph Parameters

The unimorphs were fabricated following the similar steps described in earlier sections. The area ratio of the PMN-PT disc to that of the Brass was 0.44 while the thickness ratio was 1.26 except for two samples, U-22C* and U-22D*. The approximate composition of the samples along with their specifications is mentioned in Table 4.5 below. The area ratio of the PMN-PT to the brass substrate was 0.44 for all the samples fabricated.

Table 4.5: Specifications of Fabricated PMN-PT Unimorphs for Node Mounting

(Composition is derived from Curie temperature and the phase diagram, Section 3.4.1)

Sample Name	Ingot	Wafer No.	Composition (% PT)	Thickness of PMN-PT h_p (mm)	Thickness of Brass Substrate h_m (mm)	Thickness Ratio h_p/h_m
U-22A	X28	4	39.3±1.4	0.19	0.15	1.26
U-22B	X28	4	39.3±1.4	0.19	0.15	1.26
U-22C	X28	9	35.5±0.7	0.29	0.15	1.93*
U-22D	X28	9	35.5±0.7	0.33	0.15	2.2*
U-22E	X28	15	33.5±0.5	0.19	0.15	1.26
U-22F	X28	15	33.5±0.5	0.19	0.15	1.26
U-22G	X28	22	32.4±0.7	0.19	0.15	1.26
U-22H	X28	22	32.4±0.7	0.19	0.15	1.26
U-22I	X28	29	30.0±0.4	0.19	0.15	1.26
U-22J	X28	29	30.0±0.4	0.19	0.15	1.26
U-22K	X28	36	29.6±0.4	0.20	0.15	1.33
U-22L	X28	36	29.6±0.4	0.19	0.15	1.26
U-22M	X28	43	29.1±0.4	0.19	0.15	1.26
U-22O	X28	49	28.8±0.4	0.19	0.15	1.26

Table 4.6 shows the dielectric constant (D.C.) and the poling data for the 14 unimorphs. It was observed that the dielectric constant of samples with composition less than 34% PT, i.e. less than the MPB, decreased upon poling from their unpoled state. Small variation of properties was also observed between unimorphs fabricated from PMN-PT discs from the same wafer. Unimorphs below the MPB was initially poled to 100 V or 526 V/mm while the unimorphs closer to or higher than the MPB was poled at a larger field of 789 V/mm. Two poling peaks were observed for unimorphs below the phase boundary when poled higher than 526 V/mm, as in U-22H shown in Figure 4.24.

Table 4.6: Properties of Unimorphs from Table 4.5 after Epoxied to Brass

Sample Name	D. C. Before Poling (1kHz @ RT)	D. C. After Poling (1kHz @ RT)	Dielectric Loss (1kHz @ RT)	Poling Field (V/mm)	Applied Poling Field (V/mm)
U-22A	2619	4770	0.03	631	789
U-22B	2506	4858	0.01	552	789
U-22C	2039	3735	0.01	362	789
U-22D	2976	2885	0.01	287	789
U-22E	2047	2642	0.27	315	789
U-22F	1975	1889	0.01	236	526
U-22G	2291	1688	0.01	315	526
U-22H	2230	1448	0.02	263	526
U-22I	2425	1341	0.01	236	526
U-22J	2404	1294	0.01	315	526
U-22K	2336	1413	0.01	250	526
U-22L	2361	1644	0.04	236	526
U-22M	2417	1392	0.01	263	526
U-22O	2312	1566	0.43	236	526

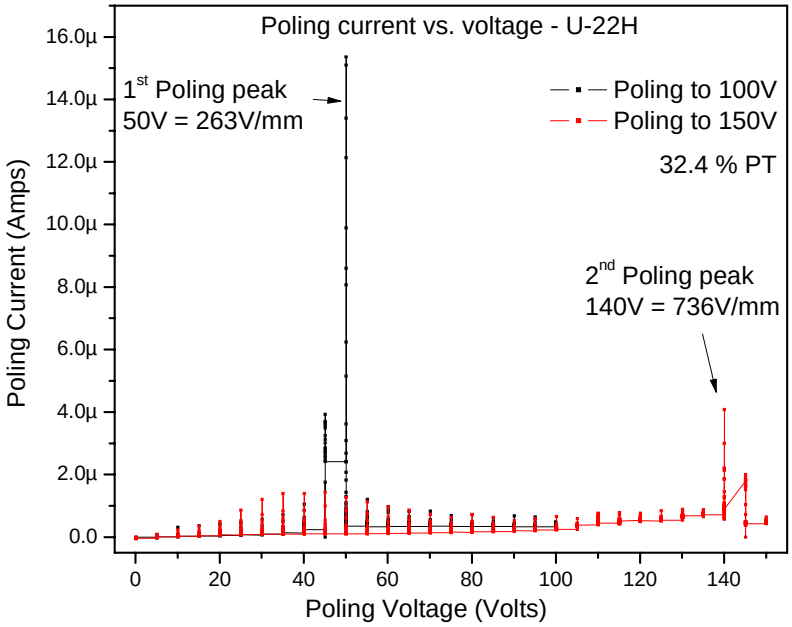

(a) U-22H – 32.4% PT

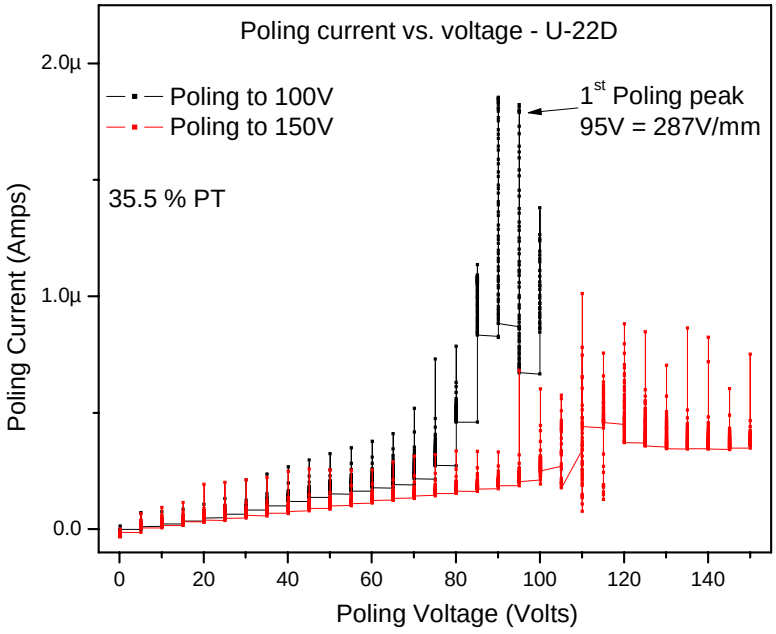

(b) U-22D – 35.5% PT

Figure 4.24: Poling current vs. Poling voltage for two unimorphs with different PT composition

4.3.2.3 Orientation of PMN-PT discs of X28 Ingot

The orientation of PMN-PT discs cut from X28 was also investigated as mentioned earlier in Section 4.2.2.3. The <001> pole figures obtained from a typical pattern is shown in Figure 4.25 and it can be noted that it was very similar to the wafers obtained from P150 ingot and Figure 4.8. A similar Wulff Net was generated and compared with the pole figure and the closest major pole was observed to be <-1 -2 3>, Figure 4.26. The <-1 -2 3> direction was at an angular distance of 6º from the center of the Wulff net. The (0 -1 1) plane was 13.1º while the (-1 -1 1) plane was 26.4º from center of the net.

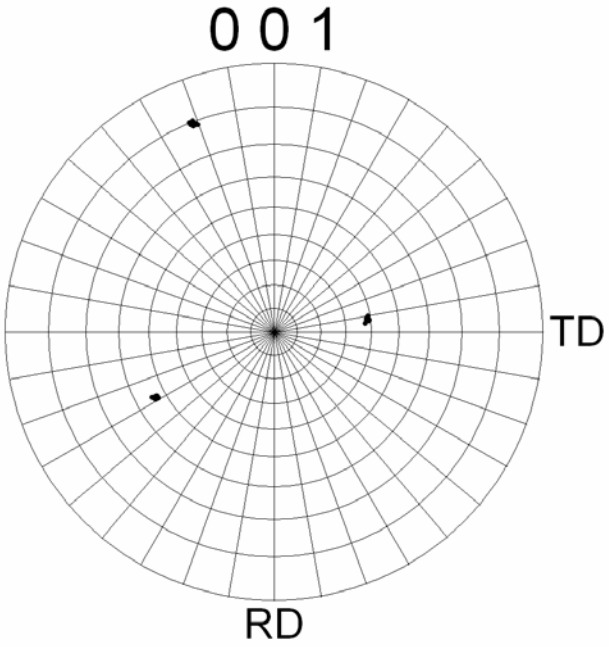

Figure 4.25: 180º <001> Pole figure of PMN-PT wafer from X28 ingot. Each grid on the TD and RD axis is 10 degrees.

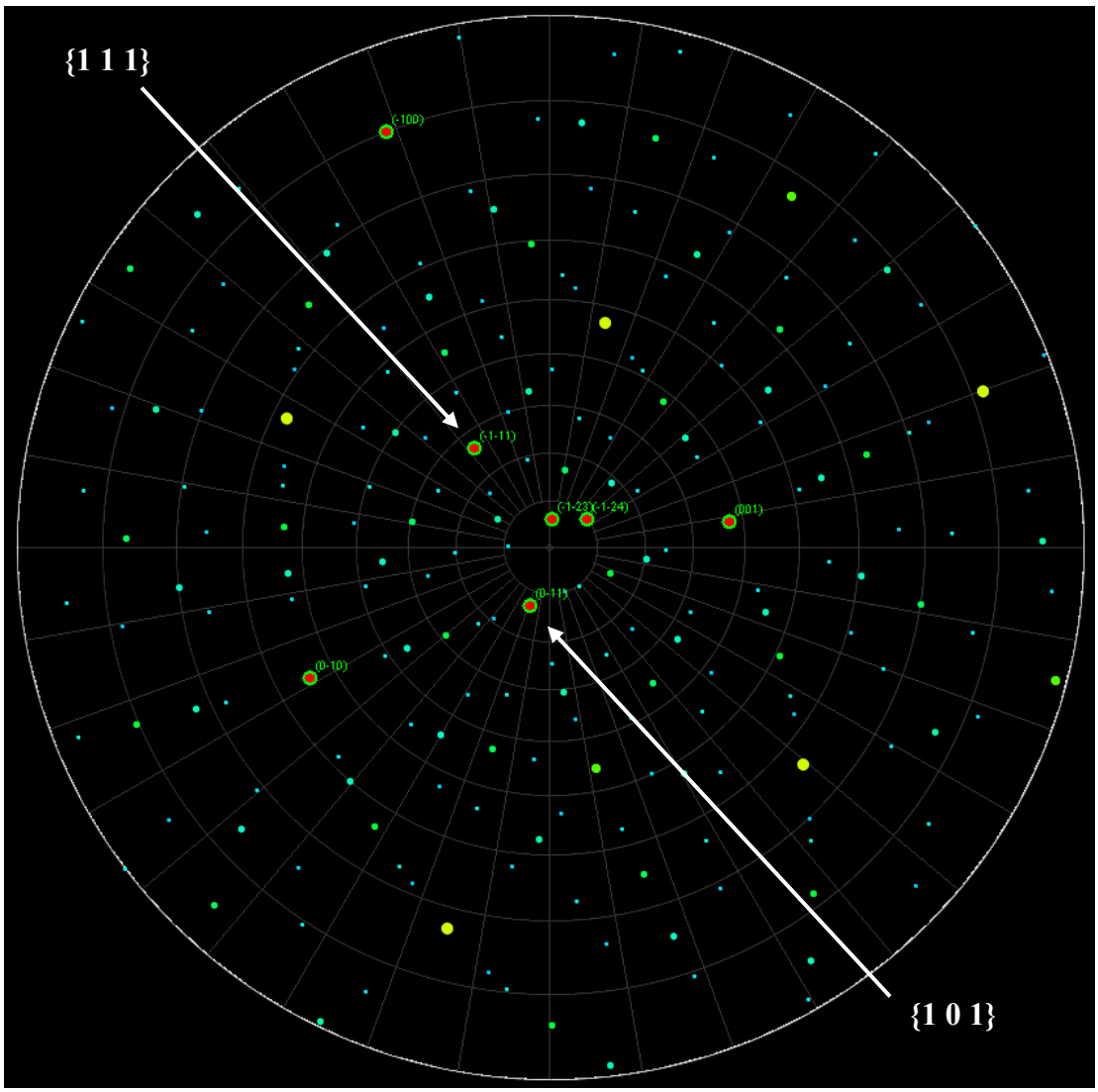

Figure 4.26: Wulff Net of pseudo-cubic crystal matched with pattern in Figure 4.25

It was observed that similar to P150 the normal direction of the wafer was a higher order of (1 2 3} family of planes. The wafer orientation is however closer to the {0 1 1} family of planes than to {1 1 1} family of planes. Hence, the unimorphs fabricated and tested from wafers of X28 would have an orientation of <1 2 3>.

4.3.3 Power Output Results

Once the unimorphs have been glued to the brass washers, they are placed on a 25.4 mm diameter aluminum tube mounted on the JBL speaker using Teflon screws as shown earlier in Figure 4.19. The total vertical distance of the mounted unimorph from the speaker was 58.3 mm. Passive circuit components were used for the output circuit in the three different configurations shown below in Figure 4.27 as Case-I, Case-II and Case-III. Case-I is similar to that of the circuit used for center mount while Case-II and Case-III has an additional passive capacitor, C_0, in order to match the impedance of the unimorph. The output circuit cases were conceived to emulate a resonator in order to match the active piezoelectric device at near resonant mode operation.

The resonant frequency was determined as before using a frequency sweep in the desired range. The resonant frequencies of the unimorphs coupled to the tube were determined to be 2700 ± 50 Hz. The resolution of the function generator was ±5 Hz and hence the resolution of the reading in the oscilloscope was within an accuracy of 10Hz. The excitation voltage from the function generator to the Kepco bi-polar amplifier was kept constant throughout the experiments. The output circuit was connected to the oscilloscope ground after the shunt resistance which prevented depoling of the piezoelectric unimorphs. The output resistance, R_L, was 10 Ω while the shunt resistance R_S was 1 Ω.

Case-1:

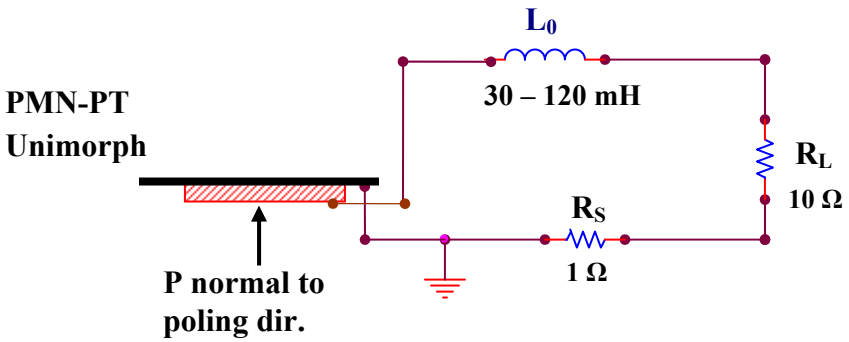

Case-II:

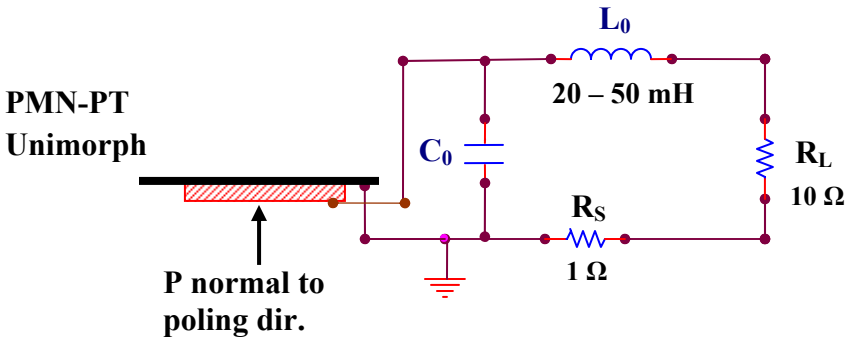

Case-III:

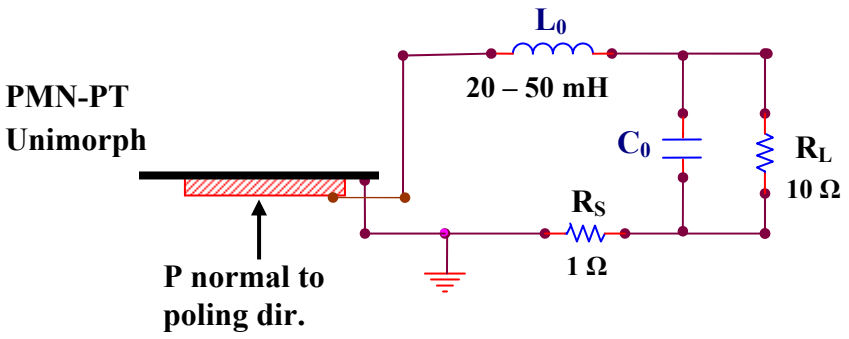

Figure 4.27: Schematic of circuit configurations used for output

The unimorphs of Table 4.5 were tested for all three output circuit cases. All the three output circuit performed reasonably with Case-II being better for most of the unimorphs tested. The parallel capacitor increased the power output of the unimorphs with a higher effective capacitance near resonant frequency. Figure 4.28 shows the output power for each of the circuits Case-I, Case-II and Case-III. The red points on the graph show the power of each unimorph averaged over the three cases. It can be seen that the difference between the power output for each of the cases for a given unimorph varied less than between unimorphs having different compositions and hence dielectric constant. U-22A, U-22B, U-22F and U-22M would have the highest output power with Case-2 and for same thickness ratio. It should be noted that U-22C and U-22D had a higher thickness ratio than 1.26 and hence their low output power can be justified.

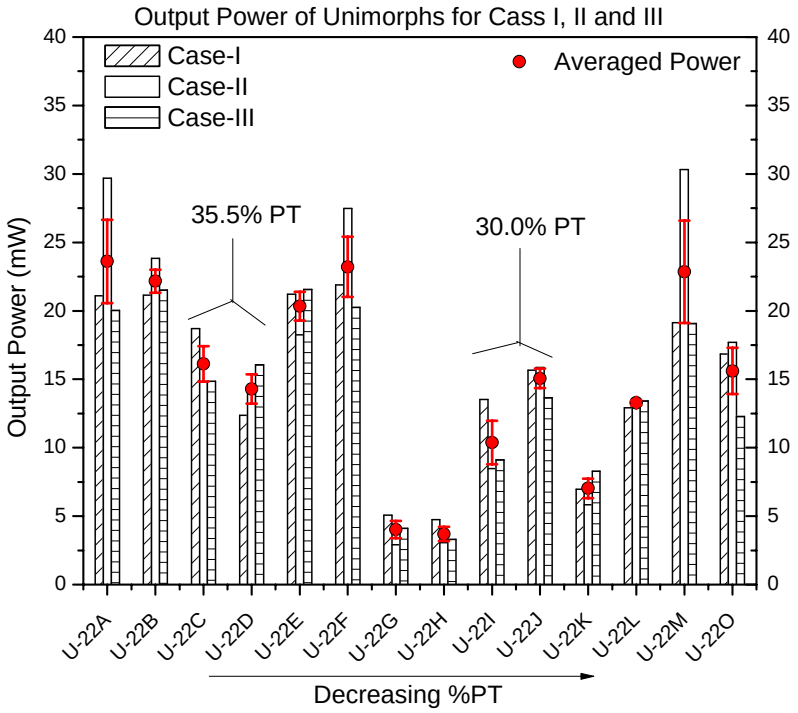

Figure 4.28: Power output of the unimorphs for three output circuit cases

(Composition of each PMN-PT unimorph is listed in Table 4.5)

The resonant frequency of the node mounted unimorphs is presented in Table 4.7 along with corresponding values of the inductor, L_0, and the capacitor, C_0, for cases II and III. The resonant frequency varied from 2660 Hz to 2690 Hz and showed no dependence on the type of the circuit. The parallel capacitor C_0 in Case-II and Case III reduced the value of L_0. This is beneficial as large inductors are expensive and have implementation issues for a miniaturized circuit application. However, Case-III is not promising both in terms of output power and because of the low value of C_0 at resonance.

Table 4.7: Resonant Frequency and Circuit Parameters Used for Maximum Output Power in Cases I, II and III (Composition of PMN-PT is presented in Table 4.5)

Unimorph Name	**% PT**	**Case-I**		**Case-II**			**Case-III**		
		Resonant Frequency (Hz)	L_0 (mH)	Resonant Frequency (Hz)	L_0 (mH)	C_0 (nF)	Resonant Frequency (Hz)	L_0 (mH)	C_0 (nF)
U-22A	39.3	2660	31	2660	18	74.8	2670	27	19
U-22B	39.3	2680	31	2670	25	25.9	2680	29	5.5
U-22C	35.5	2680	63	2670	63	1	2680	60	2.5
U-22D	35.5	2670	60	2670	59	0.3	2680	55	3.2
U-22E	33.5	2670	52	2670	53	1.3	2680	47	6.3
U-22F	33.5	2670	57	2660	49	11	2690	53	3.4
U-22G	32.4	2670	85	2700	77	3	2670	75	3.7
U-22H	32.4	2670	99	2690	87	4.1	2680	85	5.1
U-22I	30.0	2680	99	2680	90	3.4	2680	87	4.2
U-22J	30.0	2670	114	2670	75	16.3	2690	105	1.7
U-22K	29.6	2670	122	2680	110	2.4	2680	115	1.7
U-22L	29.6	2670	105	2690	85	7.5	2680	95	2.5
U-22M	29.1	2680	94	2680	39	51	2680	85	1.9
U-22O	28.8	2680	97	2690	46	40	2700	86	3.1

4.3.4 SPL Measurements

Two piezoresistive pressure transducers, Endevco® 8510-C15, were used for measuring sound pressure level inside the tube resonator. The two microphones had slightly different sensitivity of 13.36 mV/psi and 15.7 mV/psi respectively. An Endevco® Model 136 three channel DC amplifier was used to supply the excitation to the pressure transducers and pressure readout. The output scaling for each of the microphones was chosen so that the gain of the amplifier is 200, which falls within the range specified by the manufacturer. The RMS voltage output from the microphones was read through a 2-channel scope. The SPL (dB) can be calculated from Equation 4.7.

$$SPL = 20\log\left(\frac{\frac{V_{RMS}}{Sensitivity * Gain}}{P_0}\right) \tag{4.7}$$

where, P_0 is the reference sound pressure in air 20 x 10^{-6} Pa

The acoustic setup with the speaker was placed inside a Plexiglas box whose inside walls were lined with foam pads in order to minimize the effect of the reflection of sound waves from the walls of the box. One microphone was inserted on the side of the aluminum tube flush with the inner wall while the second microphone was placed on top of the brass mount and placed on top of the resonator. The second microphone was placed such that it was flush with the brass of a unimorph. Figure 4.29 shows in detail the microphone setup and the resonator tube. The microphones are named M_{1S} and M_{2T} for microphone-1 on side and microphone-2 on top. The microphones were later switched to test the relative sensitivity and Figure 4.30 shows the SPL level with frequency.

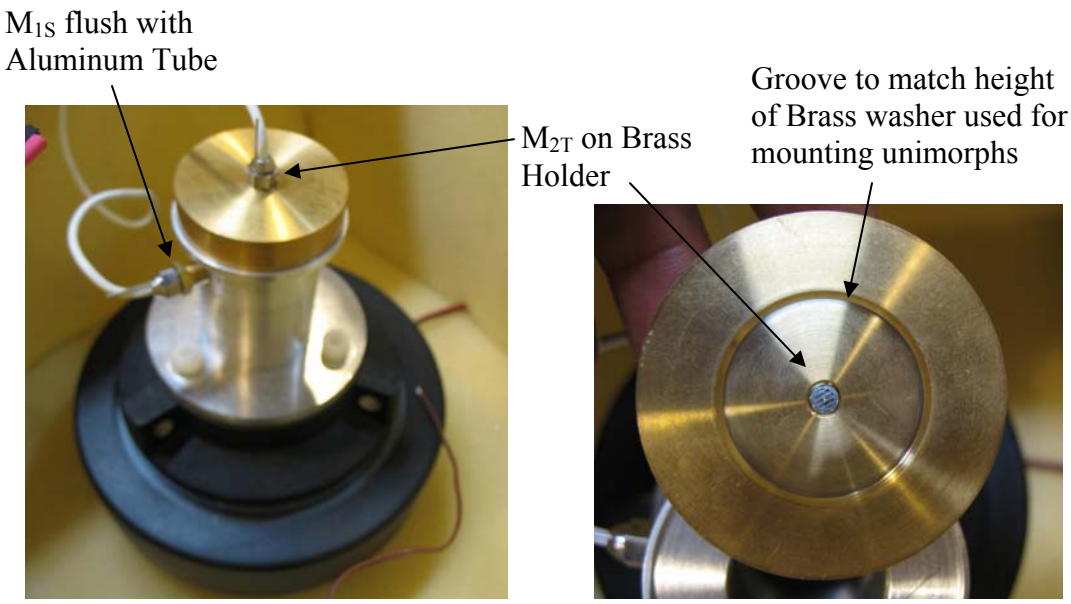

Figure 4.29: Microphone setup on the side and top of the resonator tube

(Distance of M_{1S} from Speaker = 44.5 mm; Distance of M_{2T} from Speaker = 58.3 mm)

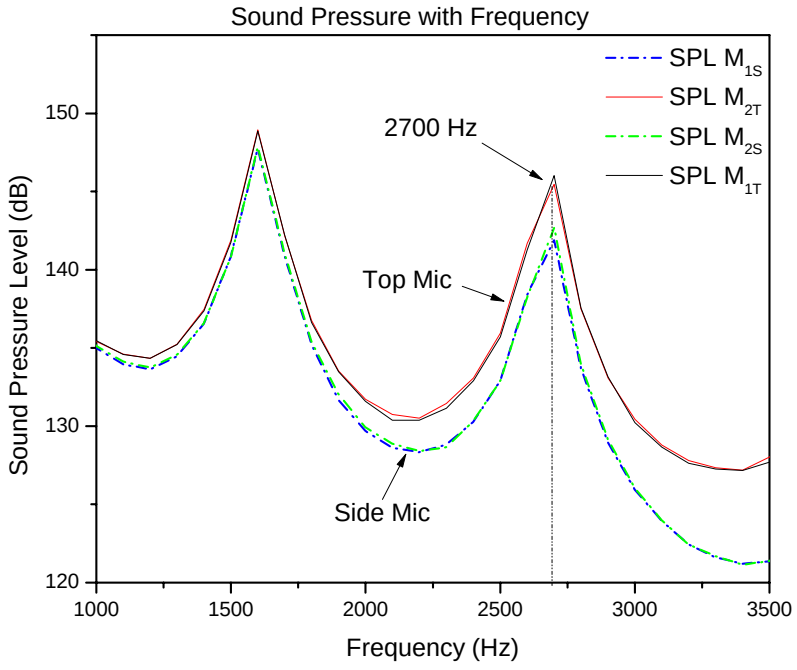

Figure 4.30: Sound pressure level with frequency sweep with two microphones

The magnitude of the sound reached local maxima near 2700 Hz and was detected by both microphones. Also it was noted that there was a negligible phase difference in the response from the top microphone and the side microphone. However, there was a notable difference in the magnitude of the sound pressure because of the near field effect. The SPL was measured as a function of input power to the speaker from the amplifier for several cases and it was observed that the SPL was more sensitive to the input power than in the far field. The rate of increase of sound pressure was more than the 3dB limit upon doubling the input power. It is shown in Figure 4.31 below.

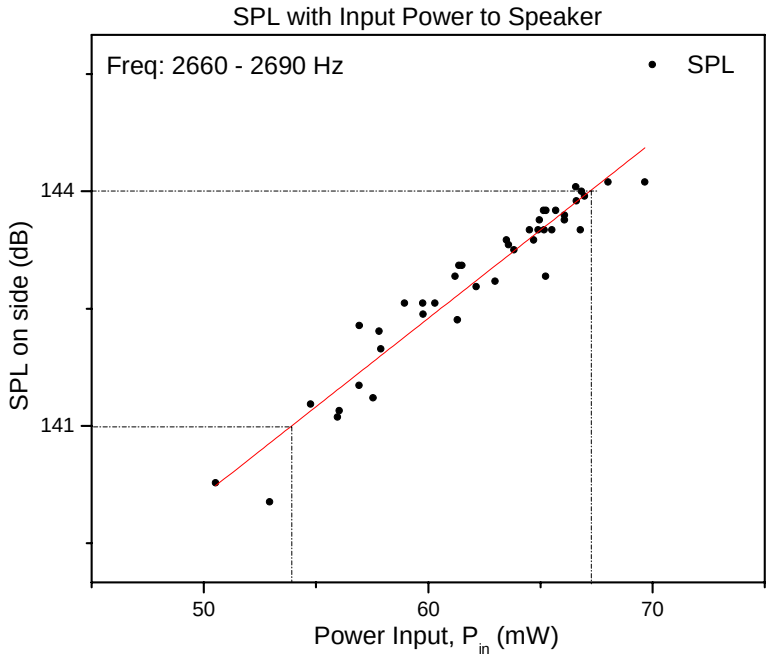

Figure 4.31: SPL measurement at 2660 – 2690 Hz with input power, P_{in}

The exact calculation of sound power in the near-field of the resonator is beyond the scope of the work presented in this thesis. However, the input power to the speaker was normalized over the on-axis SPL and frequency. The sound pressure level and efficiency of the speaker on-axis in the near field of a speaker can be very high. Figure 4.32 shows the power output and efficiency for the unimorphs tested in Case-II with SPL. It was observed that a low power output resulted from less absorption of incident sound by the unimorph and hence resulted in a high sound pressure inside the tube due to the reverberation from reflected sound field.

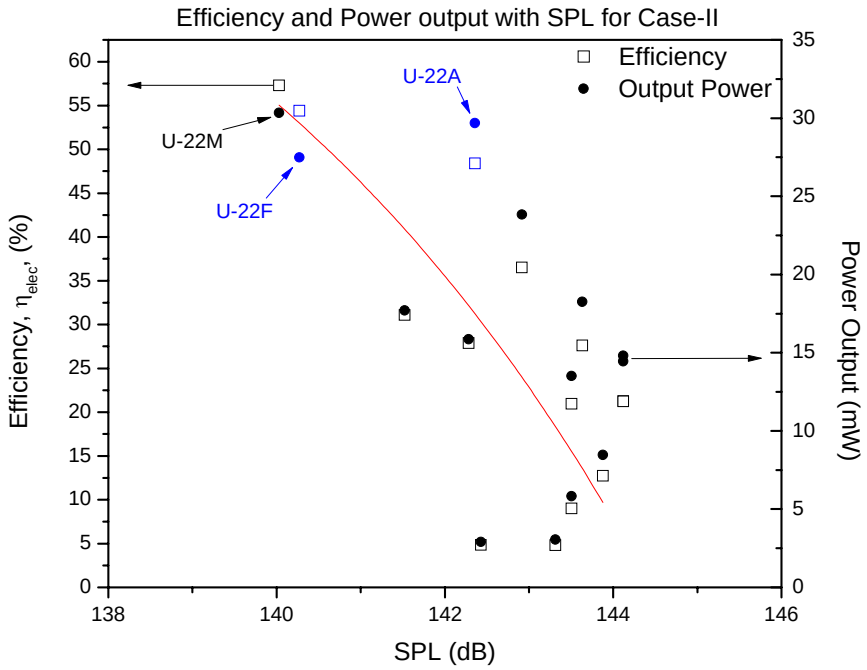

Figure 4.32: Output power variation with SPL measurement

(U-22A and U-22F shown in blue are 33% and above PT while U-22M is below 30% PT)

4.3.5 Summary

The findings of the above node mounted experiments on single crystal PMN-PT are summarized below.

1. It was demonstrated that significant power can be harvested by the PMN-PT unimorphs in node mounted setup near the resonant frequency which also depended on the resonator tube used.
2. The unimorphs were fabricated around the critical thickness ratio of 1.26 with the exception of U-22C and U-22D, which had thicker PMN-PT disc, and hence their lower power output can be justified.
3. Composition variation of single crystal PMN-PT is critical for making unimorph samples and it was observed that the unimorphs fabricated with composition between 30% PT and 32.5% PT had inferior performance.
4. The three output circuit cases used revealed insights for matching the active impedance of the unimorph using passive LCR circuits in continuous operation mode. In general, Case-II, with a capacitor element parallel to the unimorph performed the best. It also reduced the value of the tuning inductance used which is beneficial for circuit design.
5. OIM results revealed that the above tested single crystal PMN-PT discs were cut close to [1 2 3] direction which is 13.1º ± 3º from [0 1 1] direction.
6. The SPL measurements were done using a microphone and were found to be non-linear in the near field. The SPL measured is the coupled SPL of the incident and reflected wave. It is concluded that a lower SPL equals to better coupling of incident sound and the unimorph and hence a better performance.

References

[1] Uchino K., "Ferroelectric Devices", Vol. 16, 1999, ISBN-13: 9780824781330.

[2] Feldman S., "Piezoelectric transducer supporting and contacting means", United States Patent, No. 4429247.

[3] Murata Electronics, "Piezoelectric Application Guide for Buzzer", Murata Electronics North America Inc., GA, USA.

[4] Aarts R.M., "High-Efficiency Low-*Bl* Loudspeakers", Journal of Audio Engineering Society, 53(7/8), 2005, pp. 579-592.

[5] Colloms Martin, "High Performance Loudspeakers", 6th Edition, John Wiley & Sons, Ltd., pp. 28, 200.

CHAPTER – 5

PARAMETRIC STUDY OF PMN-PT UNIMORPHS

The power output from a single crystal *(1-x)*PMN – *x*PT unimorph device depends on a lot of factors. They affect the performance of the device in a cumulative way and an effort was made to determine and optimize them for higher output power. Being a coupled problem, with performance dependence ranging from material to experimental factors, the major parameters contributing to the output power can be broadly categorized as:

1) Experimental Factors
2) Resonator Tube
3) Output Circuit
4) Material Characteristics
5) Ambient Parameters

5.1 Experimental Factors

Before investigating the effects of different circuits or the inherent material properties of the unimorphs, it was important to identify external influences on power output and minimize human error in experiment and measurement. Consistency in the experimental set up was important. Placement of the unimorph, spacer, cap, and weight on the tube, Figure 4.15, adds to the degree of consistency. It is important that the electrical leads from the unimorphs are not restricted in any way by the cap and spacer. The output power dropped significantly when the electrical leads were pinched by the spacer as shown in Table 5.1a. The brass layer of the unimorphs should not be constrained at any place other than the boundary conditions imposed

which would dampen its vibration and hence output power. The effect of the brass shim put in contact with spacer in the node mounting setup is shown in Table 5.1b.

The block used as dead weight and placed over the steel cap also needs to be perfectly centered or 50% power output can be reduced as shown in Table 5.1c. To reduce the likelihood of the block being placed off-center, a ring and interlocking cylinder were glued to the top of the cap and bottom of the block respectively. All of these steps enhanced the repeatability of the experiments.

Table 5.1a: Variation of power output due to pinching of the electrical leads from unimorphs

Unimorph No.	Composition (% PT)	Power Output (mW)	
		Electrical leads pinched at spacer	Electrical leads not pinched
U-22A	39.3	21.65	24.00
U-22G	32.4	5.722	8.000

Table 5.1b: Variation of power output due to brass shim of unimorph in contact to spacer

Unimorph No.	Composition (% PT)	Power Output (mW)	
		Brass shim in contact with something	Brass shim free vibration
U-22F	33.5	8.34	13.44
U-22E	33.5	1.56	15.40

Table 5.1c: Variation of power output due to off-centering the 1500g dead weight clamping

Unimorph No.	Composition (% PT)	Power Output (mW)	
		Weight off-centered	Weight centered
U-22A	39.3	12.3	24.00
U-22E	33.5	15.4	22.00

5.2 Resonator Tube

The length of the resonator tube was critical for determining the operating resonant frequency. Different length tubes were tested to find the maximum power output at different resonant frequencies. These unimorphs were clamped to the tube using the node mounting setup and Case-I circuit with a variable tuning inductor L_0 was used. The load resistance R_L was 100Ω while the shunt R_S was 10Ω. When the tube length was increased the frequency of the acoustic harmonic decreased as shown in Figure 5.1 below. Variation of resonator tube length can be used to design effectively to an energy harvesting scheme based on the sound source. For understanding of the effect of tube length three single crystal PMN-PT unimorphs of different sizes were tested. The description of the unimorphs is listed below in Table 5.2. The unimorphs U-14G, U-17D and U-18G were fabricated from P150 ingot and their composition was between 28 – 32% PT, Figures 4.4 and 4.5. The unimorphs were tested over 5 different tubes (Tube-1 → Tube-5) with an increasing length as listed in Table 5.3. The coupled resonant frequency varied with length of the tube from 2000 – 3000 Hz.

Table 5.2: Specifications of Unimorphs of Different Diameter PMN-PT Disc

Unimorph Name	PMN-PT Ingot	Diameter of PMN-PT disc (mm)	Diameter of Brass (mm)	Area Ratio of PMN-PT to Brass	Thickness Ratio of PMN-PT to Brass
U-14G	P150	25.4	38.1	0.44	1.26
U-17D	P150	22.2	32.0	0.48	1.26
U-18G	P150	19.0	28.5	0.44	1.26

It was observed that the output power decreased rapidly beyond 2800 Hz. Simultaneously, the input power to the speaker decreased as the length of the tube decreased. Hence the efficiency with respect to the input power was calculated for each unimorph and

shown in Figure 5.2. The admittance (S) of the unimorphs mounted on the brass washer is plotted on the right Y-axis. It was observed that the tube with frequency closest to the anti-resonant frequency of the unimorphs had the maximum output power as shown in Figure 5.2.

Table 5.3: Description of the Different Steel Acoustic Tubes Used

Steel Tube No.	Length of the Tube (mm)	Diameter of the tube (mm)
Tube-1	41.73	25.4
Tube-2	52.12	25.4
Tube-3	57.25	25.4
Tube-4	64.61	25.4
Tube-5	107.03	25.4

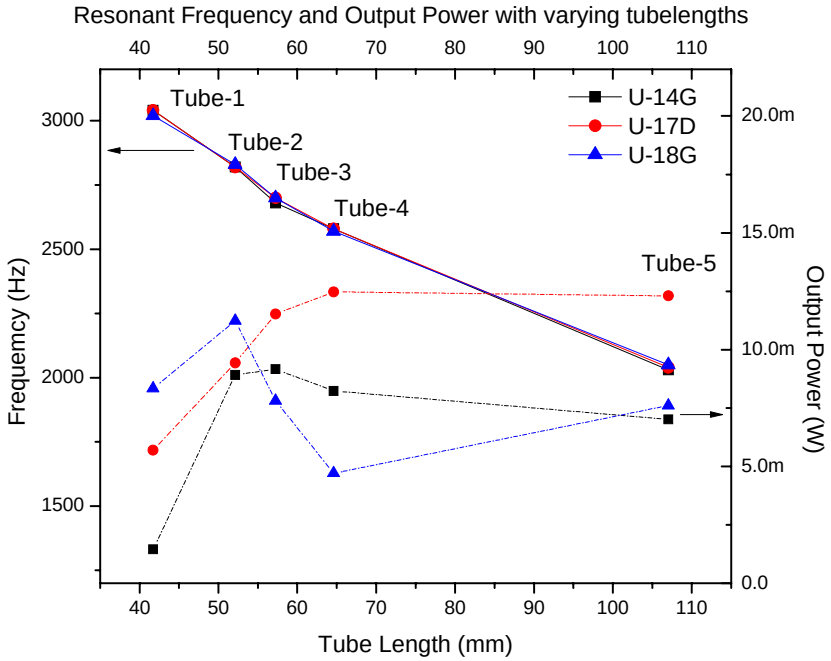

Figure 5.1: Effect of variation of tube length on resonant frequency and output power

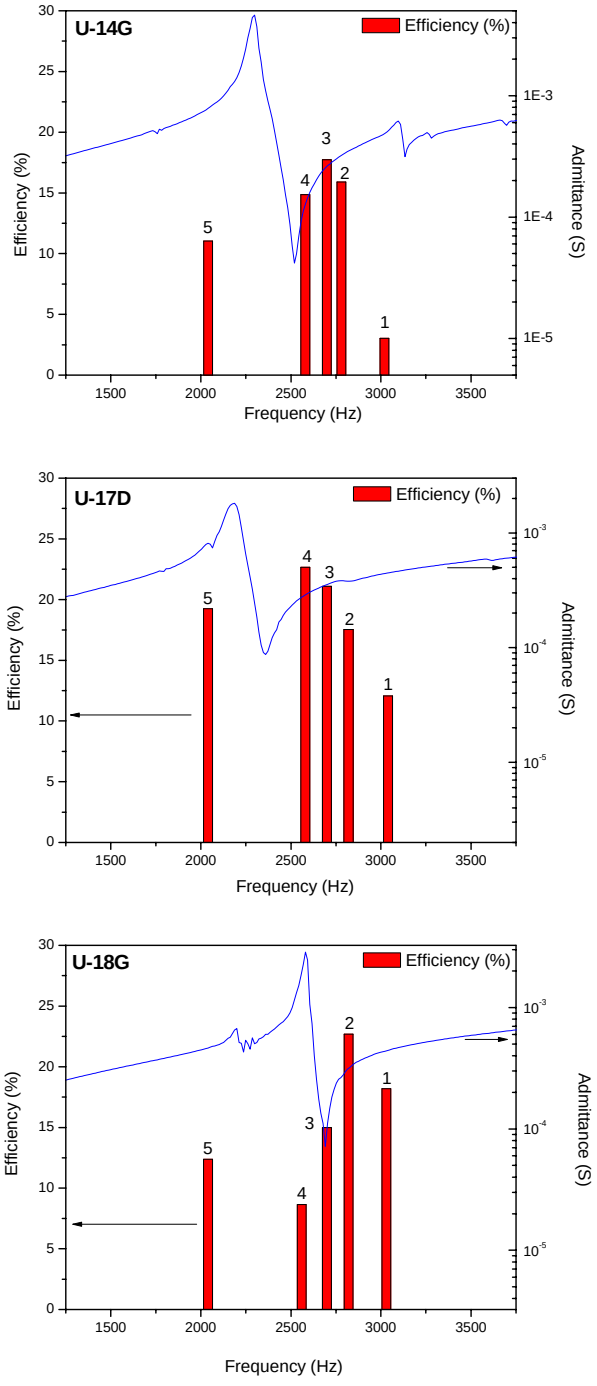

Figure 5.2: Characteristics of the unimorphs U-14G, U-17D and U-18G with different tubes

(Composition of U-14G, U-17D and U-18 G lies between 28 – 32% PT, Figure 4.5)

5.3 Output Circuit Parameters

The effect of output circuit using passive components was studied for the U-22A → U22O set of unimorphs on the tube setup mentioned in section 4.3.1. The fourteen unimorphs were tested with the three circuit cases (Case-I, Case-II and Case-III) as mentioned in section 4.3.3.

For the Case-I where, only a tuning inductor L_0 was connected in series with the load resistor R_L and shunt resistor R_S, the free capacitance of the unimorph in the unloaded state was inversely proportional to the optimized inductance L_0 of the output circuit as shown in Figure 5.3. Generally, the unimorphs with higher free capacitances, and thus lower optimized inductances, produced more power as shown in Figure 5.4. However, there are exceptions too as in the case of U-22M and U-22O below 30% PT and highlighted in the figure below.

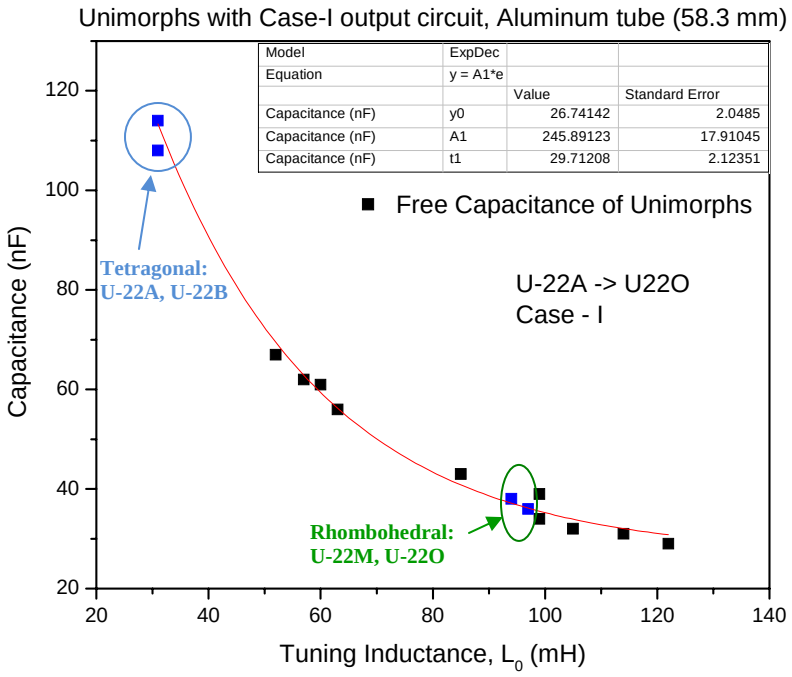

Figure 5.3: Free capacitance of the unimorphs with tuning inductance L_0 (Samples in tetragonal phase required less L_0 than in rhombohedral phase)

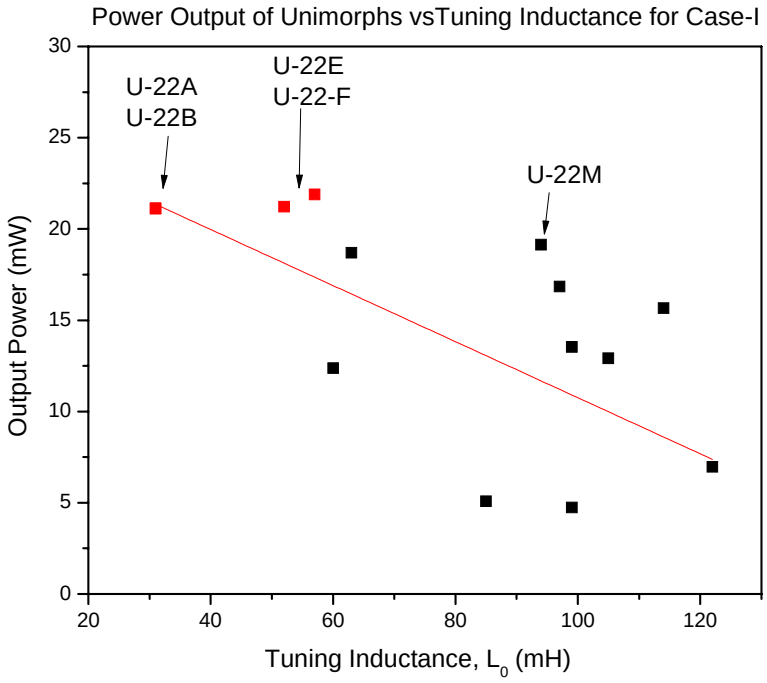

Figure 5.4: Output power with tuning inductance for Case-I

(U-22A, U-22B, U-22E and U-22F all have same thickness ratio and are above 33%PT)

This suggests that for a given energy harvesting application the voltage produced across a device is dependent on the free capacitance and is critical for realizing a high output power. However, the unimorphs with exception, i.e. U-22M and U-22O have lower composition and hence a different phase and polarization.

For the Case-II and Case-III tests, the output circuit included both an inductor and a capacitor which had to be optimized for each unimorph. After determining the resonant frequency, the L_0 and C_0 was optimized for maximum power. The inductance L_0 was incremented in 10 mH steps and the capacitance was varied at each inductance value to give the most power for that inductance value. This sequence was performed until the maximum power was achieved for a given set. The resulting pairs of capacitance and inductance, when plotted revealed an exponential relationship as shown in Figure 5.5 for the unimorph U-22F (33.5% PT). The dependence between L_0 and C_0 can be expressed in a simple exponential form as:

$$C_0 = A_1 * \exp(-L_0/t_1) + y_0 \qquad (5.1)$$

where, A_1, t_1 and y_0 are arbitrary constants.

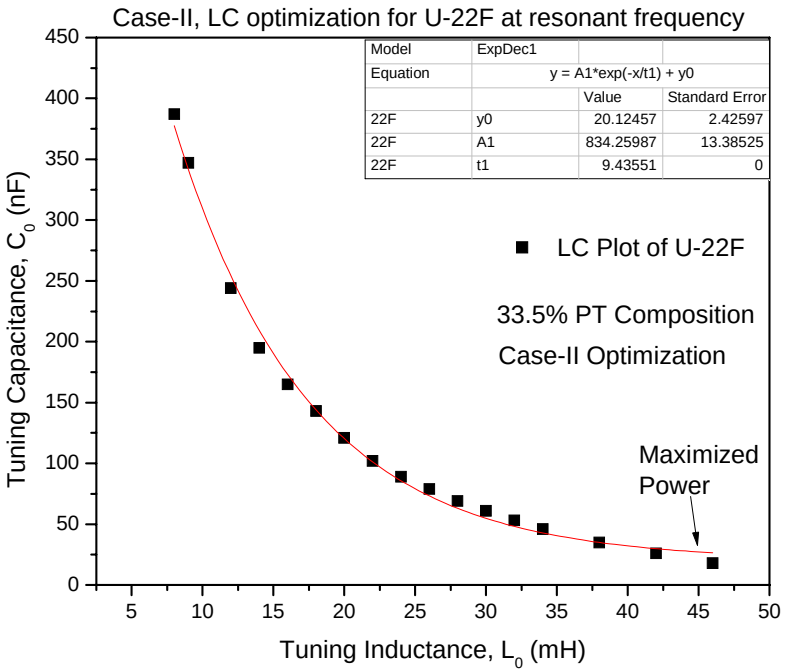

Figure 5.5: LC tuning at resonant frequency for a typical unimorph with Case-II circuit

The typical power output during the optimization routine at the resonant frequency is shown in Figure 5.6 for both Case-II and Case-III. The projection of the 3-d plot on X-Y axis is the LC plot shown in the Figure 5.5. A 10 x 10 bin wire mesh is simulated and fitted on the data. This was constructed to view the relationship of output power with the passive circuit tuning components.

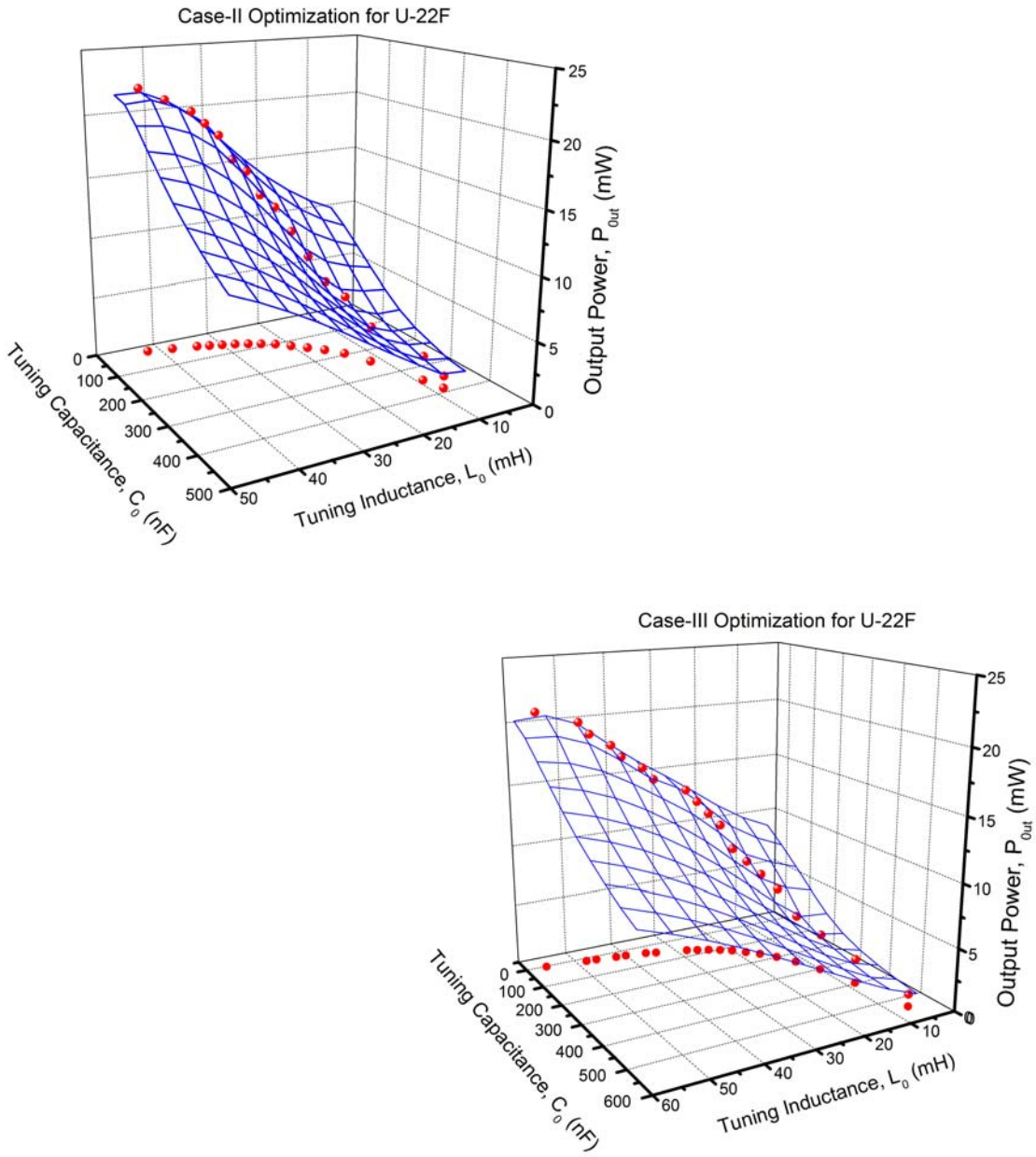

Figure 5.6: Output power with LC optimization at resonant frequency for U-22F, 33.5% PT

5.4 Material Properties

The properties of single crystal *(1-x)*PMN – *x*PT have a strong dependence on the composition of the sample. The variation of the composition results in a variation of local morphotropy and domain structure of the crystal [1, 2]. The spontaneous polarization direction below the Curie temperature hence depends on the crystal structure. In this section the variation of output power with the composition is studied. Dielectric-Curie temperature studies enabled us to study the local composition within the single crystal wafer from which the samples (U-22A → U-22O) were fabricated, as presented in Table 4.5 earlier. The variation within a wafer was approximately within ± 0.7% PT for most part of the ingot. The variation increased towards the top of the ingot in the tetragonal phase. Figure 5.7 shows the averaged power for Case-II optimization with composition.

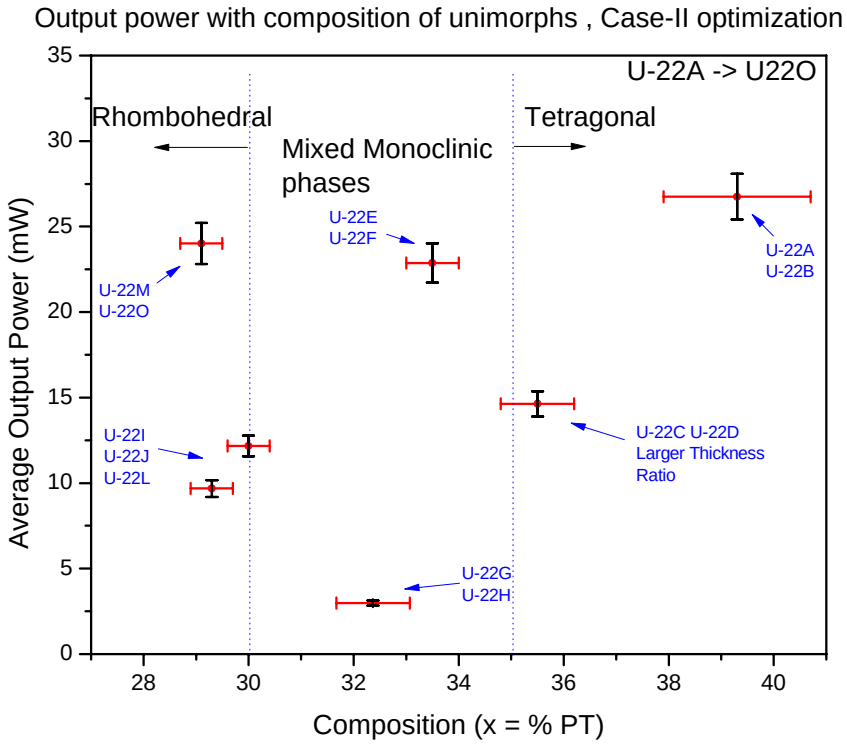

Figure 5.7: Variation of output power for single crystal PMN-PT with composition

It was observed that the output power of the unimorphs was less when the composition was close to 32% PT. The power output for a specified geometry is directly proportional to the square of the piezoelectric coefficient (d_{31}^2) and inversely proportional to the dielectric constant (□). The output power increased once the unimorphs were fabricated close to the MPB or 35% PT. It should be noted that the properties are also correlated with the orientation and hence is more complicated. However, with the exception of U-22C and U-22D which had a higher thickness ratio ~2 than the rest, there is an increasing trend for samples close to or higher than MPB. This is due to the higher d_{31} coefficient for the tetragonal phase upon poling as the spontaneous polarization is along <111> symmetry. However, for the rhombohedral symmetry the reduced dielectric constant upon poling, counters the drop in the d_{31} piezoelectric coefficient and hence results in more power output.

The dependence of poling field on the unimorphs was also studied. Two unimorphs, one from above the 35% PT phase boundary of the ingot (U-22C) and one from below the phase boundary of composition 29% PT (U-22L) was selected for the study. Electric field was applied to the unimorphs opposite to the original poling direction. This was to see if there was a preferential dependence on the direction of poling of the samples based on composition and orientation. The results are shown in Table 5.4a and 5.4b for the U-22C and U-22L respectively and the negative sign in the electric field implies the reverse direction of the poling. The output of both unimorphs decreased initially, but eventually returned to original power output achieved previously for each output circuit case. The only difference between the two unimorphs was that 22C, from above the phase boundary, had to be poled to a higher electric field in the reverse direction to reach its original power output. Hence, it can be concluded that the direction of poling didn't influence the output power of the unimorphs.

Table 5.4: Effect of Poling on Power Output of Unimorphs

(a) U-22C (~ 35.5% PT)

U-22C	Output Power (mW)		
	Case I	Case II	Case III
Before Repoling (+ 360 V/mm)	18.69	14.81	14.85
-200 V/mm	13.00	13.42	13.33
-250 V/mm	10.87	10.90	10.84
-300 V/mm	9.138	9.403	9.355
-400 V/mm	11.24	11.78	11.44
-500 V/mm	13.35	13.41	13.30
-550 V/mm	15.17	15.24	15.18

(b) U-22L (~ 29.6% PT)

U-22L	Output Power (mW)		
	Case I	Case II	Case III
Before Repoling (+ 236 V/mm)	12.91	13.52	13.41
Poled to – 200 V/mm	10.86	10.94	10.03
Poled to – 250 V/mm	15.60	16.61	15.56

5.5 Ambient Parameters

In addition to all the parameters discussed in previous sections ambient parameters, e.g. temperature, humidity and surrounding interference also affect the performance of the piezoelectric device. Due to the low frequency operation of the energy harvesting application interference from high frequency radio waves is minimal. Furthermore, use of coaxial cables and shielding of the box chamber that encloses the setup reduces the noise interference. Of all the ambient factors, temperature can affect the performance of the device in a significant proportion. Temperature changes cause a voltage to appear across the electrodes of a ferroelectric transducer due to the adjoint pyroelectric properties. Temperature also affects the properties of single crystal piezoelectric (elastic, dielectric and piezoelectric coupling) below their phase transition. Literature review suggested no general trend and the dependence must be measured in the context of the experiment. All tests for power output were performed at room temperature, which varied from day to day and throughout the day by 4-8 ºC.

To measure the effect of temperature on power output, temperature was varied for two unimorphs and power output was measured. The temperature of the setup was measured with a K-type thermocouple in contact with the outside of the spacer below the unimorph backplate. The tube was then heated slowly with a coil heater from room temperature (~ 23ºC) to 60ºC. Power output was measured at an interval of ~2ºC for the unimorph.

For the first test with U-22O (28.8% PT), the acoustic excitation frequency and optimized tuning inductance L_0 was fixed while the tuning capacitance C_0 was varied about its optimized value. The frequency was set at 2.69 kHz and L_0 was set at 44 mH. The optimal C_0 for this unimorph was 40.4 nF at room temperature. The power variation was measured at ± 10nF about 40.4 nF for each temperature measurement. The results from this test showed that as temperature

increases the power output decreases for the initial optimal C_0. However, the power increases with a peak around 37ºC ± 2ºC for C_0 = 30.4 nF, Figure 5.8. Upon cooling the unimorph back to room temperature the original power output was regained which indicates that the unimorph didn't get depoled substantially upon heating to 60ºC.

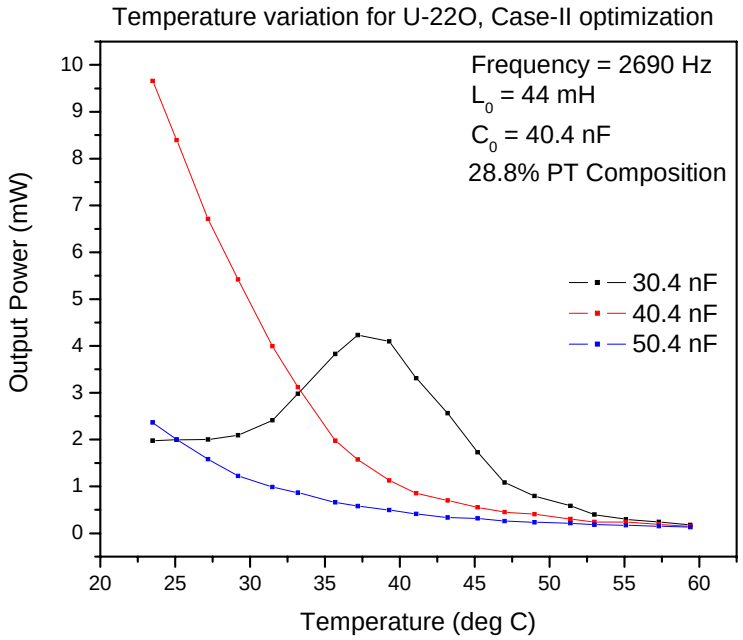

Figure 5.8: Output power with increasing temperature with varying tuning capacitance. (Resonant frequency and tuning inductance is fixed)

The increase of output power at a higher temperature for a lower value of C_0 was interesting and hence the variation with changing tuning inductance was studied. In the second test, the capacitance C_0 was kept constant at 32.4 nF along with the resonant frequency, 2.69 kHz, while the tuning inductance, L_0, was varied. The optimal L_0 was 49 mH at room temperature. Figure 5.9 shows the variation of inductance result and it can be seen that the power decreases with a ±1 mH change in the value. However, upon decreasing the tuning inductance

significantly a similar behavior can be seen as above. The power output peaks at a specific temperature.

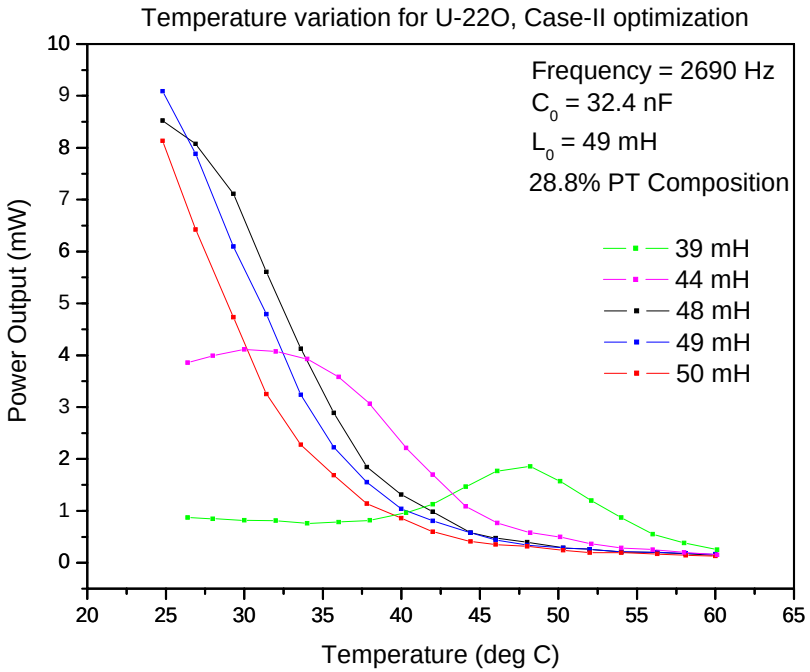

Figure 5.9: Output power with increasing temperature and varying tuning inductance. (Resonant frequency and tuning capacitance is fixed)

The effect of change in temperature is more complicated as the resonant frequency of the tube also changes simultaneously due to a decrease in the density of air. For example at a fixed atmospheric pressure a change of 10ºC results in resonance shift of 12 Hz for a standing wave tube. Hence, there was a need to measure the power output after the power was optimized on each temperature point, for taking the variation of resonant frequency into account. The resulting output power is plotted in Figure 5.10. There was a small error in temperature (±1ºC) measurement due to the time taken for determining the optimal operating parameters at any specified temperature.

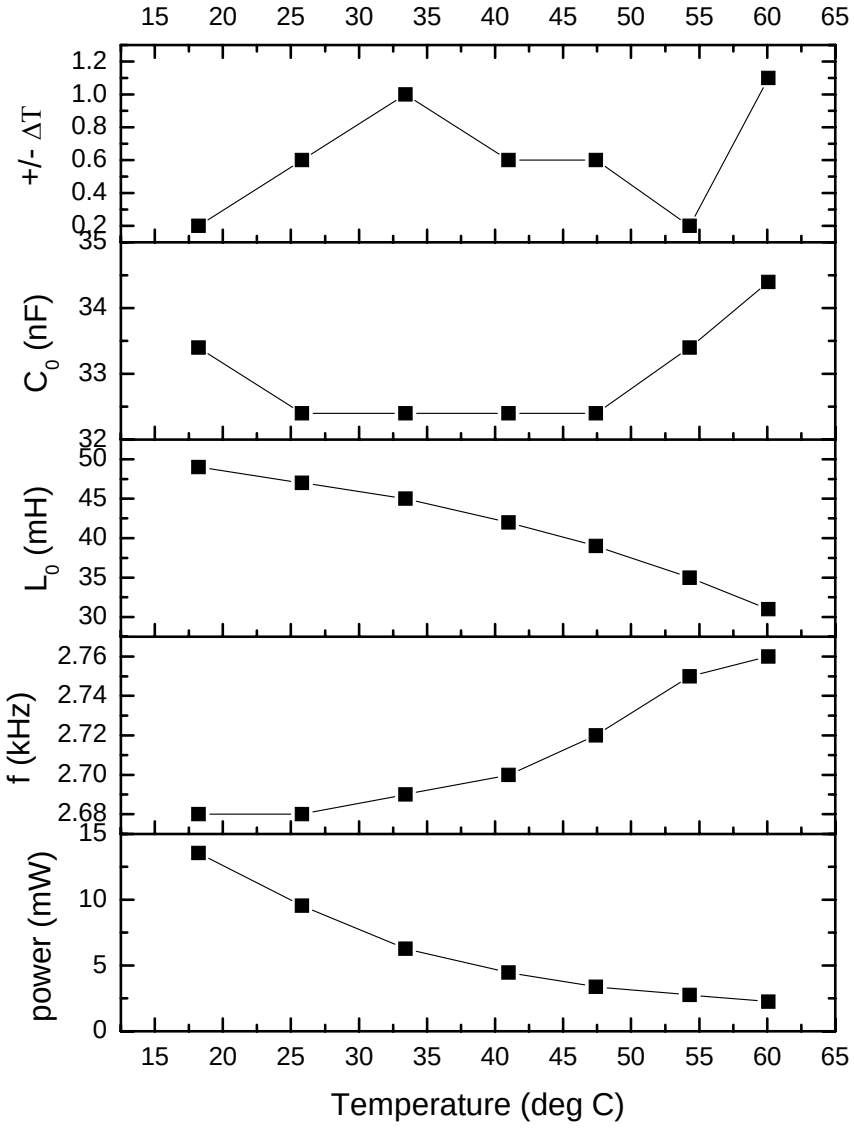

Figure 5.10: Optimization of parameters with temperature variation for U-22O (28.8% PT)

Case-II Optimization circuit was used

power – Output Power from the unimorph (mW)

f – Resonant frequency (kHz); L_0 – Tuned inductance (mH)

C_0 – Tuned capacitance (nF); +/-ΔT – error in temperature measurement (ºC)

It was observed that the output power decreased at a slower gradient when all the parameters were optimized. However, it was concluded that at high temperature the power output and hence the performance of the unimorph decreases in general. It was also seen that the parallel tuning capacitance C_0 didn't vary much upon tuning the other parameters and hence has a less significant impact on a temperature change. However the optimal tuning inductance reduced upon an increase in temperature. This might be due to counter the increase in the capacitance of the active unimorph device U-22O for impedance matching. The optimized resonant frequency changed by a maximum of 10 Hz. Care was taken not to exceed the lower temperature Curie of the single crystal device and hence depoling was not observed. Upon cooling to room temperature the output power again increased with the similar set of optimization parameters. It can be concluded that temperature is a critical ambient parameter and has to be taken into account while design and also can account for minute variation of power output on a daily fluctuation.

References

[1] Ye Z.-G., "Relaxor Ferroelectric Complex Perovskies: Structures, Properties and Phase Transitions", in "Oxides: Phase Transitions, Non Stoichiometry and Superconductors", Key Engineering Materials, 155-156, Trans Tech Publication, 1998, pp. 81-122.

[2] Yin Z.W., Luo H., Wang P.C. and Xu G.S., "Growth, characterization and properties of relaxor ferroelectric PMN-PT single crystals", Ferroelectrics, 229 (1), 1999, pp. 207-216.

CHAPTER – 6

PMN-PT CRYSTAL GROWTH

The *(1-x)*PMN – *x*PT single crystals used for fabricating the unimorph devices was grown and characterized fully in our laboratories at Center for Materials Research, WSU. This chapter provides an insight into the furnace description and crystal growth process. Efforts were made to increase both the quality and the yield of single crystal PMN-PT ingots and were met with moderate success.

6.1 Background of Single Crystal PMN-PT Growth

In the past couple of decades a lot of research was carried on growth and development of single crystal relaxor ferroelectrics with perovskite structure. Due to the better piezoelectric coefficients of *(1-x)*PMN – *x*PT over conventional PZT ceramics it is a prime candidate for high performance devices, such as medical ultrasound, Sonar, actuators and sensors [1 -3]. In the past, several research groups across the globe ventured into growing this novel material using different growth techniques. In this section a brief synopsis of different growth techniques is presented.

In 1982 Kuwata, Uchina and Nomora reported that Lead Zinc Niobate – Lead Titanate (PZN-0.09PT), a relaxor ferroelectric material of the same family as PMN-PT, had large electromechanical coupling and piezoelectric activity when poled in the <001> orientation [4]. Continued work in the 1990's by the research group of Yamashita, Park and Shrout on the flux growth of single crystals of PZN-PT and PMN-PT resulted in crystals of moderate size to be used in numerous applications [5, 6]. A PbO – B_2O_3 flux was used for growing PMN-PT single crystal from melt. Several other research groups also pursued flux growth approach

simultaneously [7, 8]. Despite attaining good piezoelectric properties with the flux growth PMN-PT crystals, it was not pursued aggressively for producing single crystals in bulk due to restrictions in the size and uniformity of crystals.

The subsequent application of conventional vertical Bridgman crystal growth technique using sealed Platinum crucibles put forth the possibility of large scale commercial production of PZN-PT and PMN-PT crystals [9]. Bridgman growth enabled the growth of single crystal PMN-PT ingots directly from the melt and the use of a seed crystal. Large size single crystal boules of 50 - 75 mm diameter and 100 mm length have been grown by researchers and crystal growers [10]. PMN-PT crystal growth in equilibrium conditions from melt suffers from compositional uniformity due to segregation of PT in the ingot. Along with the compositional variation, a long growth time required by the traditional Bridgman technique has led to a relatively low yield and hence the price remains prohibitively high for several applications.

Another alternate technique of solid state growth was also recently developed and pursued for growing single crystal PMN-PT [11, 12]. In this technique, a seed crystal is either diffusion bonded or embedded into a dense polycrystalline matrix. Upon suitable application of temperature and pressure grain growth of the seed crystal into the polycrystalline matrix occurs. Although a better compositional uniformity can be achieved, the solid state crystal growth technique has voids and inclusion defects in the PMN-PT crystals.

A different technique from those discussed above was developed by the collaboration of PiezoPartners Inc. and II-VI Inc., and further modified at Washington State University in growing single crystal PMN-PT using a modified High Pressure Bridgman (HPB) technique, [13, 14]. HPB affords a number of advantages over conventional vertical Bridgman. This technique allows the possibility of growing PMN-PT in thin wall Pt crucibles without sealing the lid. The

overpressure during the melt suppresses the formation of free Pb from melt to a large extent. A detailed analysis of the growth principles is presented in the following section.

In general, growth of single crystal PMN-PT ingots from melt has thrown a lot of challenges due to the underlying reasons:

1) Existence of multiple and mixed phases at room temperature as shown in the phase diagram in Chapter-2.
2) Compositional segregation of constituents from stoichiometry during growth from melt.
3) Presence of free lead after melt in an oxygen deficient atmosphere makes the choice and design of crucible critical.
4) Large heat capacity and poor thermal conductivity of the crystals makes it prone to cracking even in moderate thermal gradients.
5) Finally, the yield of single crystals is low both due to cracking and variation of piezoelectric properties within a region based on composition.

6.2 High Pressure Bridgman (HPB) Technique for PMN-PT

In this section the modified high pressure Bridgman growth technique used for growing the PMN-PT single crystals is presented. One of the major concerns in growing lead based crystals and hence PMN-PT is the presence of PbO above ~1100 ºC. The loss of PbO over the period of time required to grow a single crystal is significant and leads to Pb vacancies and deterioration of the piezoelectric properties of the resulting crystal. A typical solution to the problem of lead oxide loss is to grow the crystal in a sealed or nearly sealed Pt crucible; and while this is practiced by some crystal growers it increases the cost and complexity of crucible fabrication using welded platinum lids. This would increase the cost of the PMN-PT with respect to the yield of usable single crystals [15]. In the case of HPB the crucible can be an open design as the overpressure of 70 to 80 atmospheres of gas is effective in suppressing the loss PbO from the melt and maintain stoichiometry of the melt.

Another ubiquitous problem is the decomposition of PbO into Pb at growth temperatures. Free Pb atoms can flux with platinum crucible at growth temperatures of 1300 ºC. This occurs as free lead atoms in the melt diffuse through the grain boundaries of the platinum resulting in leaking of the crucible and the loss of the melt inside the furnace [16]. The solution to this problem is to have an Oxygen rich atmosphere around the crucible and melt, which converts free Pb to PbO and hence reducing the formation of the Lead Platinum eutectic. The overpressure of gas in the HPB furnace allows the achievement of partial pressures of O_2 around 0.6 – 0.7 atm which suppresses the decomposition kinetics of PbO. This is critical in avoiding the Pb/Pt leaking problem and is a major advantage to the HPB technique. This enables us to grow the single crystal PMN-PT in a thin wall platinum crucible in a simpler and cost effective manner. Also, the HPB furnaces are equipped to use graphite heating element and are capable of

achieving high temperature well in excess of 1400 ºC. The graphite heater used is very robust and requires less maintenance during and after growth or a crucible leak.

The HPB crystal growth process has been divided into the following categories and each of them is described briefly:

1) Charge Preparation: A two step columbite process is used to prepare the PMN-PT charge from the oxides [17, 18]. First magnesium oxide (MgO, Alfa Aesar – 99.998%) and niobium pentoxide (Nb_2O_5, H.C. Stark – LNA grade) is mixed and calcined in a box furnace at 1050 ºC for 9 hours. The reacted compound is a single phase magniobate ($MgNb_2O_6$). An excess of MgO of 1.5 – 3.5 % is added to account for the weight loss due to absorbed water in MgO.

$$MgO + Nb_2O_5 \xrightarrow{1050°C,9hours} MgNb_2O_6 \qquad (6.1)$$

Then lead (II) oxide (PbO, Noah Technologies) and titanium dioxide (TiO_2, Alfa Aesar – 99.995%) is mixed in stoichiometric proportions with magniobate and calcined in a furnace at 1050 ºC for 9 hours to form PMN-PT compound. The prepared PMN-PT charge is pulverized using a mortar and pressed in an isostatic press to prepare its final form, Figure 6.1.

$$PbO + (1-x)MgNb_2O_6 + xTiO_2 \xrightarrow{1050°C,9hours} Pb(Mg_{1/3}Nb_{2/3})_{1-x}Ti_xO_3 \qquad (6.2)$$

2) Crucible Preparation: A thin wall, 400ml, 99.99 % pure platinum crucible of semi-round shape is used for growing PMN-PT. The charge prepared above is placed in the crucible. The platinum crucibles weigh typically 130 – 135 g and can contain close to 1900 g of PMN-PT charge. A thin platinum foil is placed over the crucible as a lid but is not welded. Figure 6.2 shows the crucible with PMN-PT charge.

3) Furnace Build: The crucible with charge is placed in the HPB furnace pressure vessel over a circular alumina pedestal. Four type-R thermocouples are in contact with the crucible bottom for temperature readout. A 99.8% dense alumina tube, closed on one end, is then used to partition the furnace into two chambers. This is done in order to independently control the atmosphere of the two chambers. The outer chamber containing the graphite heater is pressurized with pure argon gas while the inner chamber is pressurized with 1.0 – 1.5 % O_2/balance Ar mixed gas. The seal between the two chambers is maintained using a negative differential pressure on the alumina tube. Figure 6.3 shows the build with the crucible on top of the pedestal.

4) Growth: After the build is complete the furnace chamber is closed. The chamber is then pressurized to 1050 psi (~72 atm) and heated to ~ 1350 ºC. At this point the crucible is slowly inserted into the hot zone using a translation stage. Once the entire charge is melted and soaked, the crucible is pulled to an appropriate place in the furnace. The furnace is then cooled down slowly with the imposed thermal gradients till the melt nucleates and the crystal growth is completed. The entire growth takes 11-12 days till the furnace reaches the room temperature and the pressure vessel is depressurized. The hardware control is automated and uses a program to control all the parameters to the selected setpoints.

5) Post Growth: The HPB chamber is opened and the crucible with the crystal is taken out. The platinum crucible is cut to take the crystal out. Due to the grain growth at high temperature, the platinum crucibles cannot be reused after a crystal growth. The crystal is then sent for inspection and slicing in a wire saw and characterized. Figure 6.4 shows an as grown PMN-PT ingot inside the crucible.

Figure 6.1: Calcined PMN-PT charge after being pressed in isostatic press

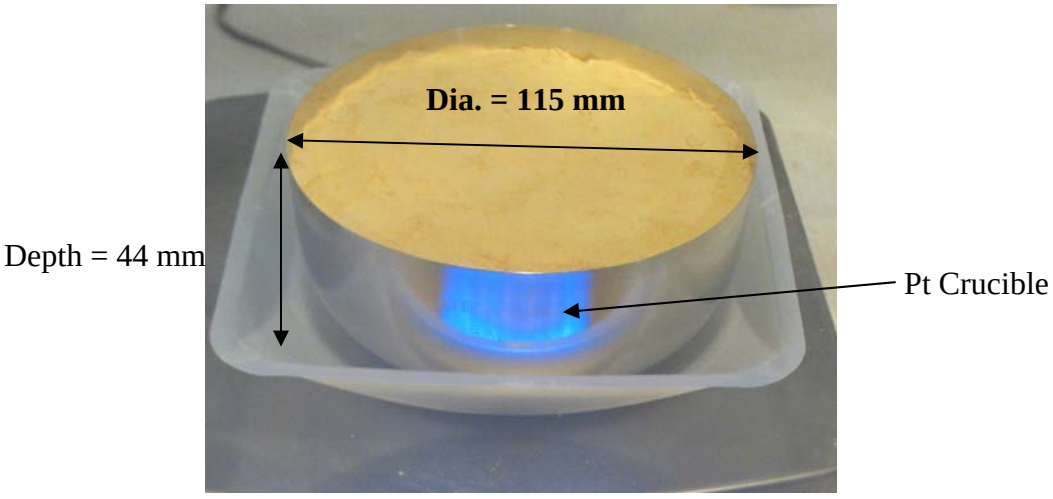

Figure 6.2: Platinum crucible with PMN-PT charge

(Weight of Crucible + Charge = 2036 g)

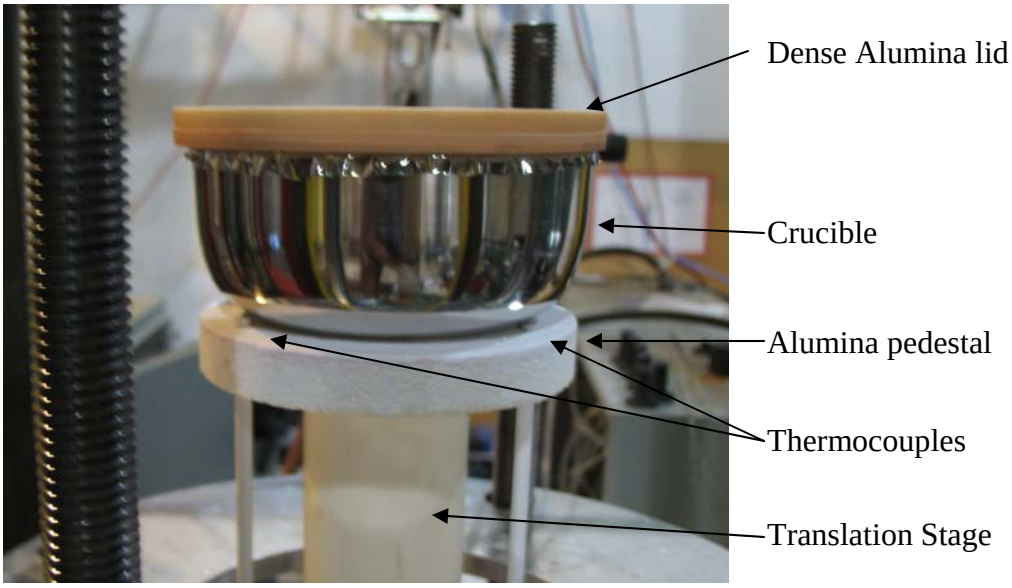

Figure 6.3: Crucible on top of alumina pedestal in the HPB furnace

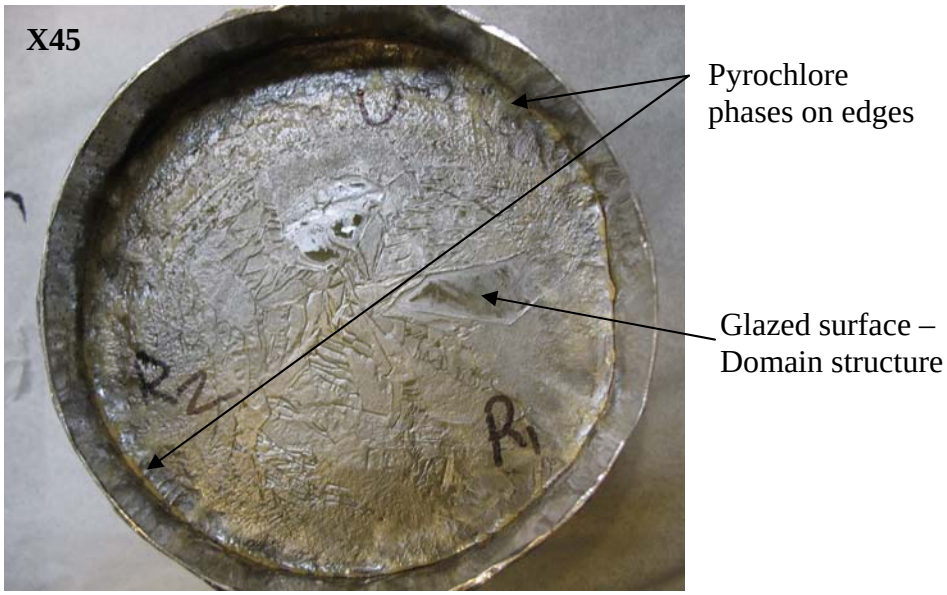

Figure 6.4: PMN-PT single crystal after growth

The total time from start to finish for each crystal growth in the HPB furnace varies between 12 to 14 days depending on the imposed growth rate. The time is considerably shorter than the typical vertical Bridgman growth practiced by commercial crystal growers. Figure 6.5 shows a typical temperature profile with time for a crystal growth. The major parts of the growth includes 1) melting of the charge, 2) soaking, 3) growth, 4) high temperature cooldown and 5) Curie temperature cooldown and are shown distinctively in the figure below. The time for each segments can vary depending on each experiment and other parameters. The melting point of PMN-PT is also depends on the composition or % PT of the starting charge. For 32% PT, the melting point is around 1290 – 1300 ºC.

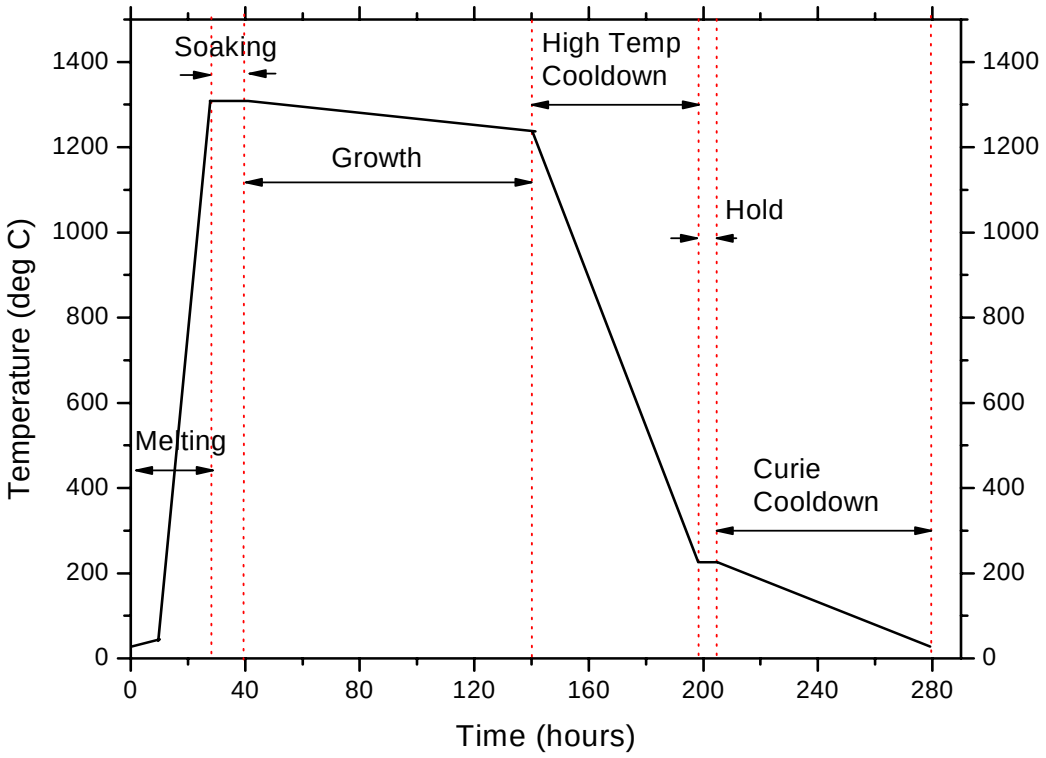

Figure 6.5: Typical temperature profile used for growing PMN-PT in HPB furnace

6.3 Composition Variation in PMN-PT

After the ingot is grown and taken out a vertical slice is cut in an arbitrary orientation across the ingot using a wire saw. The thickness of the slice is between 1.0 – 2.0 mm and samples are cut from this slice to determine the Curie temperature and hence the composition across the ingot. The segregation of PT in the ingot is primarily dependent on the growth rate or the imposed cooling rate of the furnace during growth segment via the control thermocouple placed adjacent to the heater. The growth rate is calculated from the temperature read by the thermocouple which is in contact with the tip of the crucible. Table 6.1 shows a comparative study of 4 different crystals grown in HPB furnace. Also mentioned are the starting composition and the oxygen amount in parts per million (ppm) during the crystal growth. The oxygen partial pressure surrounding the melt also has a role in the growth kinetics as increase in O_2 increases the viscosity of the melt.

Table 6.1: Growth Parameters for *(1-x)*PMN - *x*PT Crystal Growths in HPB Furnace

Ingot Name	Starting Composition of PMN- *x*PT (*x* = %PT)	Furnace Cooling Rate (ºC / hour)	Duration of Growth Segment (hours)	Growth rate at Tip of the crucible (ºC / hour)	Oxygen Partial pressure (ppm)	Pressure in Furnace (psi)
X21	32	2.0	96	1.678	11400	1050
X26	32	1.5	104	1.101	9600	1050
X43	29	1.2*	125*	0.939	8500	1050
X46	29	0.75	108	0.562	8600	1050

* - Was divided in two segments with a hold after 75 hours

Small square samples were taken from a vertical slice through these ingots for studying the local composition. Figure 6.6 shows the schematic of the relative position of the slice and the samples taken for composition studies. The vertical variation can be defined as the difference in composition between samples at top-center, TC and bottom-center, BC of ingot while the maximum composition variation would be seen from the BC to the top-edge, TE samples. This was due to the convex shave growth interface as it progresses to the top of the ingot. Table 6.2 shows the composition variation across the ingots with different growth rates.

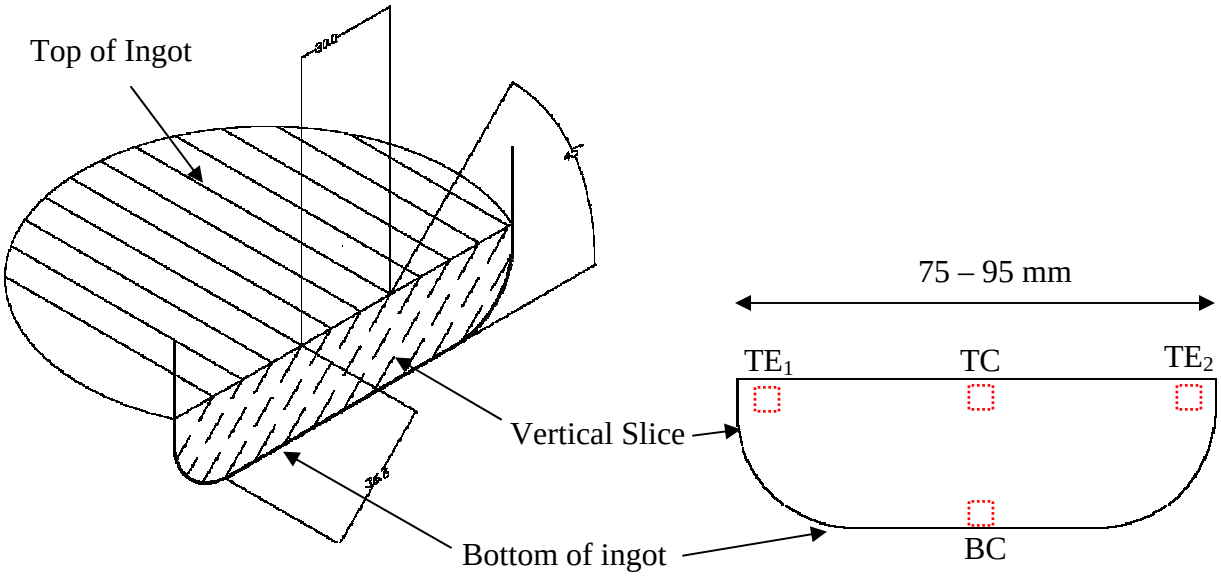

BC – Bottom Center of Ingot

TC – Top Center of Ingot

TE_1 and TE_2 – Top edge of the Ingot

Figure 6.6: Schematic of the position of samples for composition variation

Table 6.2: Composition Variation for the Crystals in Table 6.1

Ingot Name	Growth Rate (ºC /hour)	TE Comp. (x = % PT)	TC Comp. (x = %PT)	BC Comp. (x = %PT)	Shape of the MPB interface
X21	1.67	39.4	38.9	30.65	Linear
X26	1.01	38.1	38.9	29.5	Mostly Linear with curved towards edge
X43	0.93	41.2	34.1	25.7	Curved convex
X46	0.56	42.1	35.2	26.0	Curved convex

It was seen that as the growth rate decreased the growth interface became more curved with a convex shape. This was reflected in the less PT composition variation from bottom to top at the center of the ingot as compared to the top-edge of the ingot. Figure 6.7 below shows the MPB interface in the slice for two ingots which can be seen as the boundary between the lighter region and the darker region.

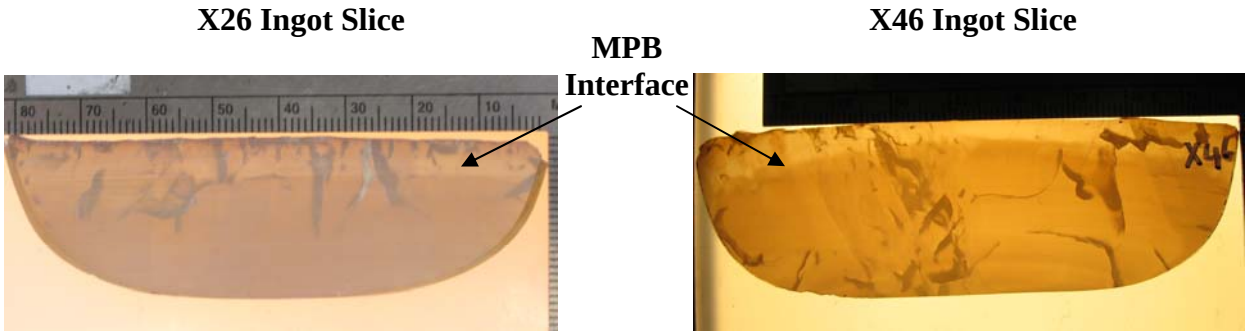

Figure 6.7: Shape of MPB interface on a vertical cross-section of X26 and X46 ingot (Mostly linear in X26 while convex curvature can be seen in X46)

6.4 Crystal Growth Attributes

In this section, other attributes PMN-PT growth from the HPB technique is discussed briefly. It was important to study the various phenomena associated with crystal growth and their effect on the PMN-PT single crystal system.

1) Pyrochlore: It is known that the presence of pyrochlore phases is detrimental to the properties of the PMN-PT single crystal [19]. Metastable and stable phases of Lead pyrochlore are formed due to the presence of unreacted Nb_2O_5. Hence, the two step columbite method used ensures the formation of mostly single phase PMN-PT. The presence of oxygen around the melt in the HPB furnace also favors the formation of various pyrochlore phases. The following steps were taken to reduce amount of pyrochlore phase in the single crystal:

a) Preparing the columbite or magniobate ($MgNb_2O_6$) at a higher temperature of 1050 ºC drives the reaction kinetics to completion and hence removes unreacted Nb_2O_5. Moreover, the particle size of the MgO and Nb_2O_5 powders should be comparable to each other for uniform reaction throughout.

b) During melting, the platinum crucible containing the pre-compounded PMN-PT charge is heated rapidly towards the melting point, i.e. from 900C – 1300C. This is achieved by translating the crucible into the hot zone of the furnace at 100 mm/hr which is equivalent of an average heating rate of 250 C/hr.

Due to the lower density and lower freezing point of pyrochlore it solidifies at the very end of growth near the top edge of the ingot. Also pyrochlore residues were observed in the grain boundaries as reddish lines. Figure 6.8 shows some pyrochlore on the edge of a typical ingot.

The oxygen control in the furnace coupled with fast melting of the charge enabled to reduce pyrochlore significantly.

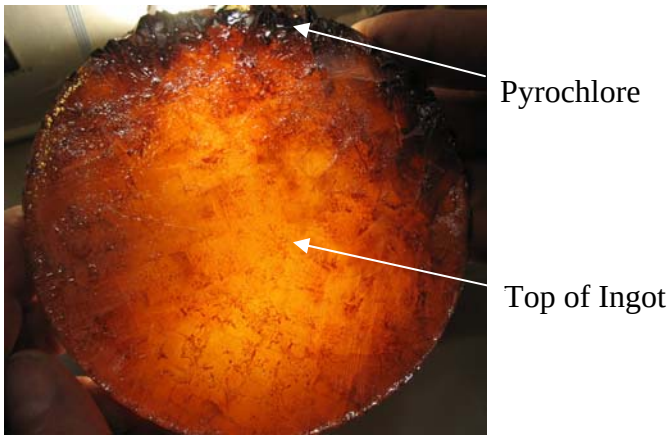

Top surface of a PMN-PT ingot gorwn by HPB technique

Figure 6.8: PMN-PT ingot with small amount of pyrochlore in top of ingot

2**) Cracking:** The single crystal ingots of PMN-PT grown via HPB technique have a fair amount of cracking. There are two types of cracks: 1) deep cracks that run across the cross-section of the ingot and 2) micro-cracks that are present in small regions within the ingot. The non-homogeneous morphotropic phase transition near the Curie temperature causes stress in the single crystal and can cause or propagate cracks. Also high temperature thermal instabilities during the cooling down of the ingot after growth can be the reason for deep cracks. It should be noted that as a material PMN-PT has a very large heat capacity and poor thermal conductivity. In the crystal growths at WSU, the appropriate cause of cracking is still being investigated. However, the following steps/measures were taken to reduce cracking.

a) The cooling rate of the ingot from 200 ºC – 20 ºC had to be 3 ºC/hour or less in order to reduce the effect of stress from Curie temperature phase transition effect.

b) During high temperature cool down of the PMN-PT ingot the pressure inside the vessel was reduced from 1050 psi to 400 psi simultaneously.

c) Care was taken to remove the platinum crucible after the crystal growth. The ingot sticks to the crucible due to the grain growth of the platinum into the single crystal at high temperatures.

Figure 6.9 below shows an ingot with deep cracks on the edges and some micro-cracks in the center. The picture was taken against a bright white light.

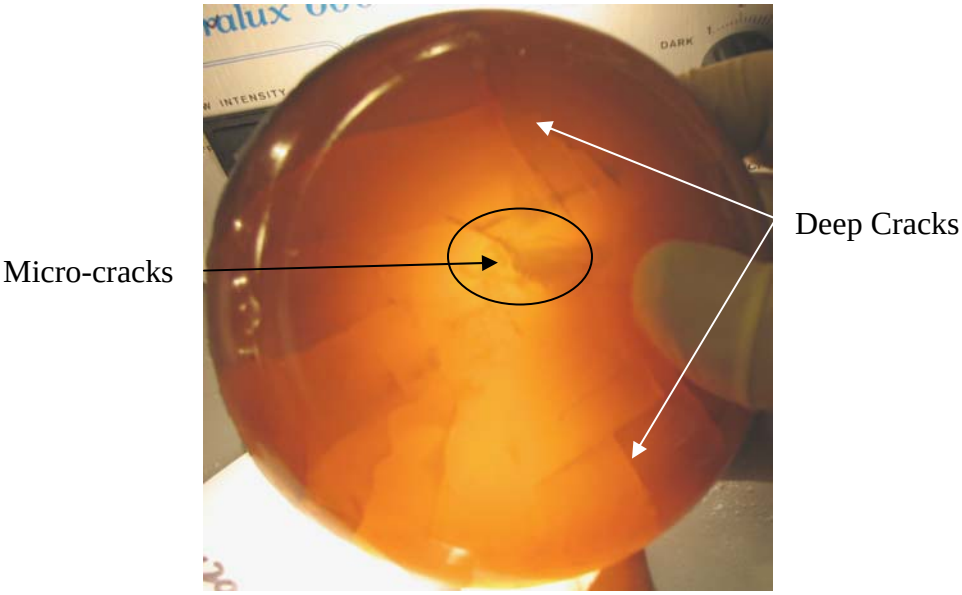

Figure 6.9: Cracking in an as grown PMN-PT ingot in HPB furnace

3) Nucleation: The high temperature phase diagram of PMN-PT was proposed in recent past [20 – 22]. The melting point of *(1-x)*PMN – *x*PT depends on the starting composition 'x' of PT. The melting point of PMN – 0.3PT and PMN – 0.35PT was determined to be 1296 ºC and 1288 ºC respectively [22]. A detailed high temperature phase diagram was developed by J. Guo based on DTA studies on various mole percentages [21]. The melting point was found to be not congruent and the presence of constitutional supercooling was demonstrated by the difference of solidus and liquidus line for x = 0.25 – 0.4, which is the region of interest for applications of single crystal PMN-PT. The spontaneous nucleation always occurs at a lower supercooled melt and hence the control of thermal gradients is critical for minimizing multiple nucleation sites across the melt. Figure 6.10 below shows a schematic of high temperature phase diagram of PMN-PT solid solution, [22].

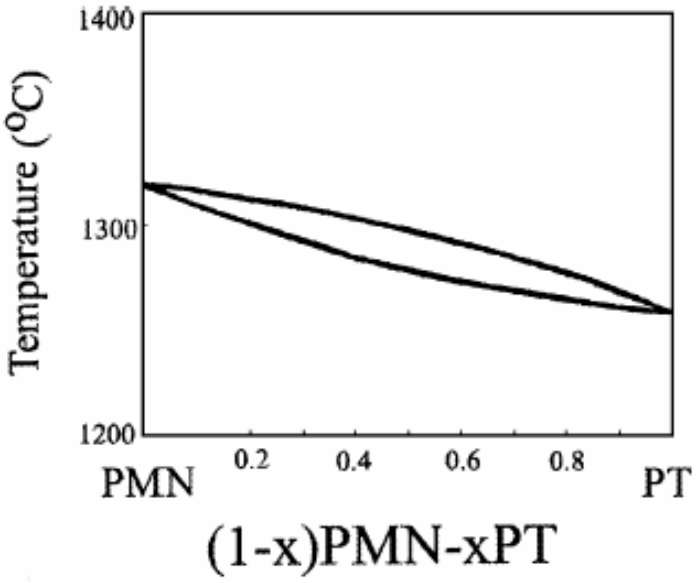

Figure 6.10: Schematic of high temperature phase diagram of PMN-PT

(Adapted from work of Luo et al, [22])

For a single heterogeneous nucleation at the tip of the crucible, both the radial and the vertical gradient across the melt have to be sufficiently large. The constitutional supercooling can be aggravated by the absence of a large radial gradient, which reduces diffusion of particles across the nucleation interface. This results in multiple nucleation sites of a bulk of liquid across the bottom of the crucible and can be seen as a large exothermic event and a dendritic growth pattern. The alumina insulator pedestal used to support the platinum crucible plays an important role in controlling the thermal gradients across the crucible. Several crystal growths were performed with varying alumina insulator properties (both physical and material). The properties of the insulators used are summarized in a tabular format in Table 6.3. The exact reason and the recipe for controlling constitutional supercooling of ingots grown from melt in the absence of a seed crystal using HPB technique is still under investigation.

Table 6.3: Properties of Insulators Used as Pedestals for Crucible

Type	Material name	Chemical Constituent	Dimensions (mm)	Thermal conductivity (W/m-K)	Density (g/cc)	Comments
A	DAHP – Zircar Ceramics	99.55% Al_2O_3	Dia. = 101 mm Thickness = 19mm	2.3 (1200 ºC)	3.2	Dense, M. of Rupture[1] – 19.3 MPa
B	Gemcolite - 3000	65% SiO_2; 32% Al_2O_3	Dia. = 111 mm Thickness = 19mm	0.28 (1093 ºC)	0.25	Porous, M. of Rigidity - 0.51 MPa
C*	BNZ – 32 Armil CFS	20.7% SiO_2; 78.3% Al_2O_3	Dia. = 101 – 111mm Thickness = 10 – 19 mm	0.62 (1093 ºC)	1.2	Porous, M. of Rupture[1] – 2.1 MPa

[1] – Room temperature cold crushing, ASTM C 133; * - Different diameters and thicknesses used

Type A material was dense alumina plate and had the highest thermal conductivity and was also difficult to machine. Growths using this insulating pedestal didn't result in good single crystals and a softer material with a lower thermal conductivity, Type B was used. Although this material produced good crystals, the flexural strength of this material was very low at high temperature and the material got deformed during growth. Hence, a stiffer material, an insulating firebrick - Type C was used in recent growths. The thermal conductivity was slightly higher than Type B. When the thickness of the pedestal using Type C was reduced to 9.5 mm, repeated supercooling was observed with a dendritic growth, Figure 6.11. The graph on the right shows the thermocouple at the tip for the corresponding growth.

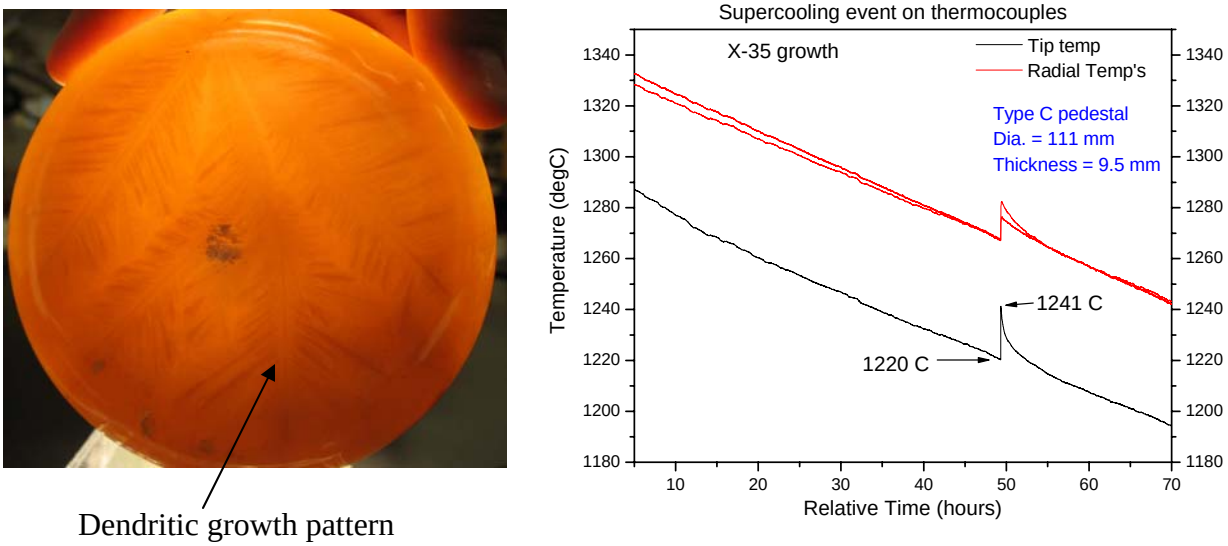

Figure 6.11: Dendritic growth at the bottom of PMN-PT ingot

(Use of thinner (9.5 mm) type C insulation material for pedestal,

21 ºC supercooling event at Tip of the crucible)

Although the exact cause and remedy of averting supercooling has not been ascertained completely the following findings were observed for growth of PMN-PT by HPB technique.

a) A low thermal conductivity material is desirable as an insulator for pedestal.

b) The thickness of the pedestal material should not be less than 12-13 mm on the extreme edge. A curved pedestal on the interior was proven to be useful.

c) The liquid melt of PMN-PT should not be overheated as it increases the liquid convection and hinders the formation of nucleation sites. Hence, a superheated melt has a higher probability of supercooling.

d) An exothermic event on a thermocouple indicates nucleation around the local region. A bigger radial gradient of more than 50-60 degrees from center to the edge of the melt (radial distance ~ 40 mm) would prevent nucleation throughout the entire bottom of the crucible and hence prevent dendritic growth.

6.5 Summary

Good quality large diameter PMN-PT single crystal have been grown using the seedless HPB growth technique. The process has been optimized with several process parameters over more than 65 crystal growth runs. The high pressure and oxygen control around the melt are two key attributes for enabling stoichiometric growth of PMN-PT in thin walled, off-the-shelf platinum crucibles. The yield can be increased further by resolving issues like deep-cracking in the as-grown ingot. As of now, the deep cracking is believed to be originating from high temperature growth instabilities or cooling the single crystal ingot in a thermal gradient. Figure 6.12 shows several rectangular bars from an x = 0.32, PMN-PT ingot and the longitudinal piezoelectric coefficient, k_{33}, of sample C3 after <001> orientation. The typical range of k_{33} values obtained from several samples ranged from 0.84 – 0.91.

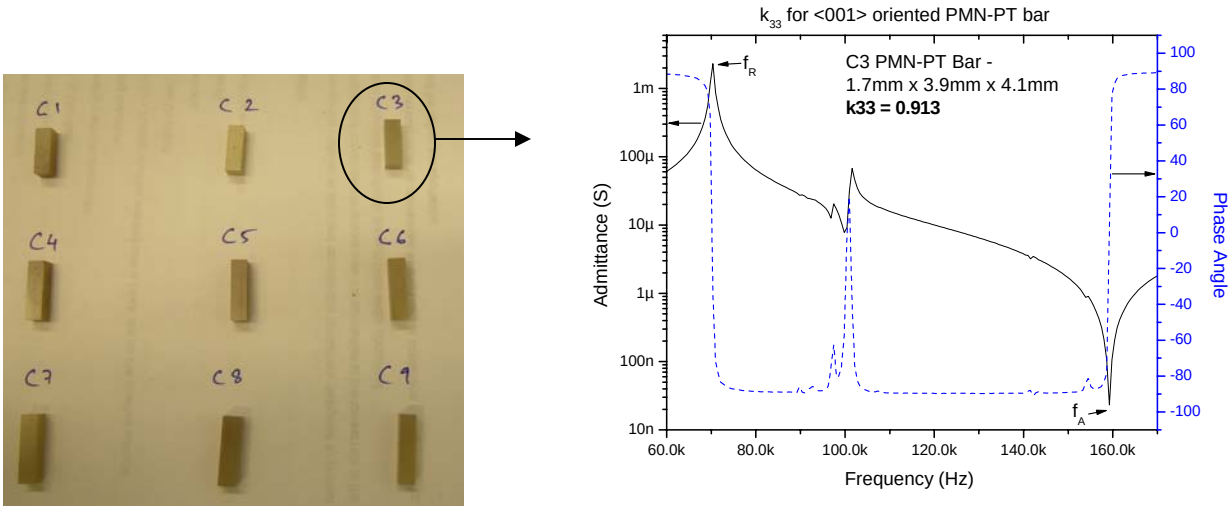

Figure 6.12: Longitudinal piezoelectric coefficient, k_{33} = 0.91, for a <001> oriented rectangular bar of PMN – 0.32 PT

References

[1] Li H., Li Y.C., Zhou D., Peng J., Luo H.S. and Dai J.Y., "Application of PMNPT single crystal in a 3.2 MHz phased-array ultrasonic medical imaging transducer", Applications of Ferroelectrics, 16th IEEE International Symposium on UFFC, ISAF-2007, pp. 572-574.

[2] Park S.E. and Shrout T.R., "Ultrahigh strain and piezoelectric behavior in relaxor based ferroelectric single crystals", Journal of Applied Physics, 82, 1997, pp. 1804-1811.

[3] Ewart L.M., McLaughlin E.A., Robinson H.C., Amin A. and Stace J.J., "Mechanical and Electromechanical Properties of PMN-PT Single Crystals for Naval Sonar Transducers", Applications of Ferroelectrics, 16th IEEE International Symposium on UFFC, ISAF-2007, pp. 553-556.

[4] Kuwata J., Uchino K. and Nomura S., "Dielectric and Piezoelectric Properties of $0.91Pb(Zn_{1/3}Nb_{2/3})O_3$-$0.09PbTiO_3$ Single Crystals", Japanese Journal of Applied Physics, 21, 1982, pp. 1298-1302.

[5] Yamashita Y., "Large electromechanical coupling factors in perovskite binary material system", Japanese Journal of Applied Physics, 33, 1994, pp. 5328-5331.

[6] Park S.E. and Shrout T.R., "Relaxor based ferroelectric single crystals for electro-mechanical actuators", Materials Research Innovations, 1 (1), 1997, pp. 20-25.

[7] Dong M. and Ye Z.-G., "High temperature solution growth and characterization of the piezo-/ferroelectric $(1-x)Pb(Mg_{1/3}Nb_{2/3})O_3$-$xPbTiO_3$ [PMNT] single crystals", Journal of Crystal Growth, 209, 2000, pp. 81-90.

[8] Lim L. C., Shanthi M., Rajan K. K. and Lim C. Y. H., "Flux growth of high-homogeneity PMN-PT single crystals and their property characterization", Journal of Crystal Growth, 282, 2005, pp. 330–342.

[9] Wang P.C., Luo H.S., Pan X., Li D.L. and Yin Z.W., “Dielectric and piezoelectric properties of PMN-PT single crystals grown by Bridgman method”, Applications of Ferroelectrics, 12th IEEE International Symposium on UFFC, ISAF-2000, pp. 537-540.

[10] Pengdi Han, “Hybrid stockbarger zone-leveling melting method for directed crystallization and growth of single crystals of lead magnesium niobate-lead titanate (PMN-PT) solid solutions and related piezocrystals”, United States Patent – 6942730.

[11] Brennan R.E., Allahverdi M. and Safari A., “Templated Grain Growth (TGG) of PMN-PT Textured Components using SrTiO3 Templates”, 2004 IEEE International Conference on Ultrasonics, Ferroelectrics and Frequency Control, 2004, pp. 270-273.

[12] Kim M.S., Fisher J.G., Kang S.J.L. and Lee H.Y., “Grain Growth Control and Solid-State Crystal Growth by Li_2O/PbO Addition and Dislocation Introduction in the PMN–35PT System”, Journal of American Ceramic Society, 89 (4), 2006, pp. 1237-1243.

[13] Soundararajan R., Das R.N., Tjossem R., Bandyopadhyay A., Lynn K.G., Eissler E.E. and Lazaroff J., “Growth and characterization of single-crystal PMN–PT via HPVB method”, Journal of Materials Research, 19(2), 2004, pp. 609-615.

[14] Eissler E.E., “Single crystals of lead magnesium niobate-lead titanate”, United States Patent – 6899761.

[15] Nicoara I., Nicoara D.T., Marin C. and Ostrogorsky A.G., “Directional solidification of $PMN_{0.65}$-$PT_{0.35}$ ferroelectric crystals at 1 and 7 atm”, Journal of Crystal Growth, 274, 2005, pp. 118–125.

[16] Xi Z., Yao X., Li Z. and Xu Z., “Reaction of platinum crucible and melt during PMN-PT crystal growth”, Ceramics International, 30, 2004, pp. 1691–1694.

[17] Deng J., Xing X., Yu R., Chen J., Xing Q., Luo J. and Liu G., “Preparation and characterization of PMN-PT relaxation ferroelectric powder by columbite precursor method”, Acta Metallrugica Sinica, 41(5), 2005, pp. 503-506.

[18] Yamada H., “Pressureless sintering of PMN-PT ceramics”, Journal of the European Ceramic Society, 19, 1999, pp. 1053-1056.

[19] Wan X., Luo H., Zhang X. and Zhao X., “Feasibility of growing and optical properties of ferroelectric (1-x)$Pb(Mg_{1/3}Nb_{2/3})O_3$-x$PbTiO_3$ single crystals”, Chapter 3 - Trends in Crystal Growth Research, ISBN: 1-59454-541-3, pp. 45-69.

[20] Li Z., Xi Z., Xu Z., Wang H and Yao X., “High Temperature Phase Diagram of PMN-PT Binary System”, Ferroelectrics, 326, 2005, pp. 31–35.

[21] Jingping Gao, “Synthesis and phase diagrams of lead magnesium niobate – lead titanate – lead oxide system”, Master’s Thesis, 2003, Simon Fraser University.

[22] Luo H., Xu G., Xu H., Wang P. and Yin Z., “Compositional homogeneity and electrical properties of lead magnesium niobate titanate single crystals grown by a modified Bridgman technique”, Japanese Journal of Applied Physics, 39, 2000, pp. 5581-5585.

CHAPTER – 7

CONCLUSION AND FUTURE WORK

The need of harvesting energy for low power electronics has grown in recent past. We demonstrated that substantial electrical energy can be generated from an acoustic excitation by using a tuned single crystal piezoelectric transducer in near resonant frequency operation. Single crystal PMN-PT was used to fabricate unimorph devices and thereby tested for power output in two experimental setups with an acoustic source. Passive circuit components were used in output circuit for impedance matching and maximum power transfer at resonance. The results have been summarized below.

1. The center mounting of unimorphs yielded a maximum output power of 20.45 mW and 0.212 W/cm^3. The resonant frequency of the unimorph and the cone structure was 1.7 ± 0.1 kHz and the excitation from sound source 129-131 dB. The power output was significantly more than a PZT unimorph tested in the same setup.

2. The node mounting of unimorphs on a steel resonator tube was evaluated where the resonant frequency of the coupled structure as 2.69 kHz. Clamping the brass shim on top of the tube yielded better output power and reproducibility of power harvesting results. A maximum power of 30 mW was achieved with a certain set of optimized circuit parameters at the resonant frequency. The acoustic excitation was at near field and was approximately measured at a close proximity to the device. The SPL was found to be 142 ± 2 dB. A lower SPL measurement for a given unimorph meant enhanced coupling and

more output power as more sound energy got absorbed at the unimorph backplate instead of reverberation in the resonant tube.

3. Three different circuit configurations using an inductor, capacitor and a load resistor was tested for tuning and optimal impedance matching. A capacitor connected in parallel to the piezoelectric element yielded better results. The value of the tuning capacitor and the tuning inductor required to optimize power output were inversely related. Hence, a lower value of tuning inductance, e.g. 30 mH, and higher value of tuning capacitance, e.g. 110 nF, resulted in a maximum power output. The power output of the unimorphs decreased upon increasing the tuning inductance.

4. *(1-x)*PMN - *x*PT single crystals were grown using a self-seeding high pressure Bridgman (HPB) technique and resulting ingots were wafered and characterized. The resulting samples were used in fabricating the unimorphs used for energy harvesting tests in acoustic field. Samples taken from different parts of the ingot were tested for the local composition and it was found that unimorphs fabricated with $x < 0.3\%$ PT and $x > 0.34$ % PT yielded better power output. For $0.3 < x < 0.34$, there is an existence of mixed phases of PMN-PT (orthorhombic and monoclinic) at room temperature which could explain the drop in power output.

5. The ingots were sliced perpendicular to the growth direction to minimize the PT variation across a wafer. However it was found that the orientation of the PMN-PT samples were not in the <011> direction. They had higher order orientation symmetry, family of [123] and [124] directions and 13 – 20 degrees off the <011> direction. An oriented <011> PMN-PT sample would yield even better power output performance due to improved transverse piezoelectric coefficients.

6. Temperature variation affects the unimorph properties and power output. It was seen that the power output of a unimorph (with the optimal settings at room temperature) decreased considerably with an increase in temperature to 60 ºC which was below the lower temperature phase transition of PMN-PT, T_R, and the unimorph returned to normal after it was cooled down. When the optimization of circuit parameters was performed at a higher temperature, it was observed that the parallel tuning capacitance C_0 did not vary upon tuning the other parameters and hence has a less significant impact on a temperature change. However, the optimal tuning inductance L_0 reduced upon an increase in temperature. This is due to the increase in the capacitance of the active unimorph device at an elevated temperature.

7. Good quality single crystal samples were produced by self seeded HPB growth. Final diameters of recent ingots were 89.0 - 120.0 mm in diameter, thicknesses ranging from 19.0 - 38.0 mm, and weighing up to 1.9 kg. There has been a significant development involved for growing large diameter PMN-PT ingots using HPB technique. Controlling the oxygen partial pressure around the PMN-PT melt was paramount to prevent leaking of the thin walled platinum crucibles. A perfectly oriented <001> bar of PMN-PT single crystal have a k_{33} of 0.91.

Discussion and Future Work

PMN-PT single crystal is a complex material system with the existence of various morphotropic phases due to composition variation at room temperature. The direction of spontaneous polarization of each of these phases depends on the macroscopic domain symmetry. Hence, it is pertinent to study the properties of the samples within a certain

range of composition and orientation axis, which can often lead to variation of performance in certain applications. Moreover, the resulting stress in the ingots during growth coupled with low thermal conductivity of the material makes it prone to cracking and hence reduce yield substantially. Although the piezoelectric properties of PMN-PT single crystals are much better than conventional piezoceramics, the performance of a device can be limited by the application and device fabrication parameters. We firmly believe our results as an indicator to a possible application of PMN-PT in low frequency energy harvesting application and conversely active noise cancellation devices. Owing to superior piezoelectric properties, single crystal PMN-PT devices holds high promise as a suitable material for energy harvesting.

1. Further work needs to be done in improving the performance of single crystal device for energy harvesting. This includes an analytical or modeling of the experiment with proper boundary conditions implementation.

2. In self-seeded HPB growth, further research needs to be directed towards studying the role of thermal gradients towards heterogeneous nucleation. Analysis also needs to be done in predicting the preferable growth direction, which could be a higher order direction of symmetry.

3. Also, we have observed considerable supercooling during growth of the material when the furnace is cooled at a very slow gradient. Further work, both modeling and experimental would enable us to understand the process of supercooling and thermal gradients better.

APPENDIX

APPENDIX – 1

DYNAMIC CONTROL

It has been demonstrated earlier that the PMN-PT unimorphs generate maximum power at the resonant frequency of the device. The power dropped significantly when operated off the resonant frequency owing to high Q nature of the device. Passive circuit components have been used for impedance matching on the output side. Hence, dynamically controlling the excitation frequency and the passive circuit components on the output side would enable us to ensure the device to operate at maximum output power. The setup uses the PZS series of instruments from IETlabs. There are three units of decade boxes, a capacitor, inductor and a resistance, which can be programmed using GPIB communication module set. The arbitrary function generator AFG-5101 provides the excitation to the speaker and a Tektronix TDS3000 series oscilloscope are also incorporated in the control system and connected via GPIB. A computer acts as a host for the control of the instruments and uses a single GPIB – PCI interface. Figure A1.1 below shows the schematic of the control setup. A LabVIEW program was used to implement the data acquisition and subsequent optimization routine to automate the tuning of the unimorph devices.

The LabVIEW program receives information for a digital oscilloscope (Tektronix TDS 3014B) calculates the power output and then selectively sends control signals to programmable decade boxes or the function generator. The optimization routine uses a variant of golden section search algorithm and details about the algorithm can be found elsewhere in the literature. The assumption made during the determination of extrema is that the power dependence is a unimodal function within a small interval of search and hence will lead to a local maximum.

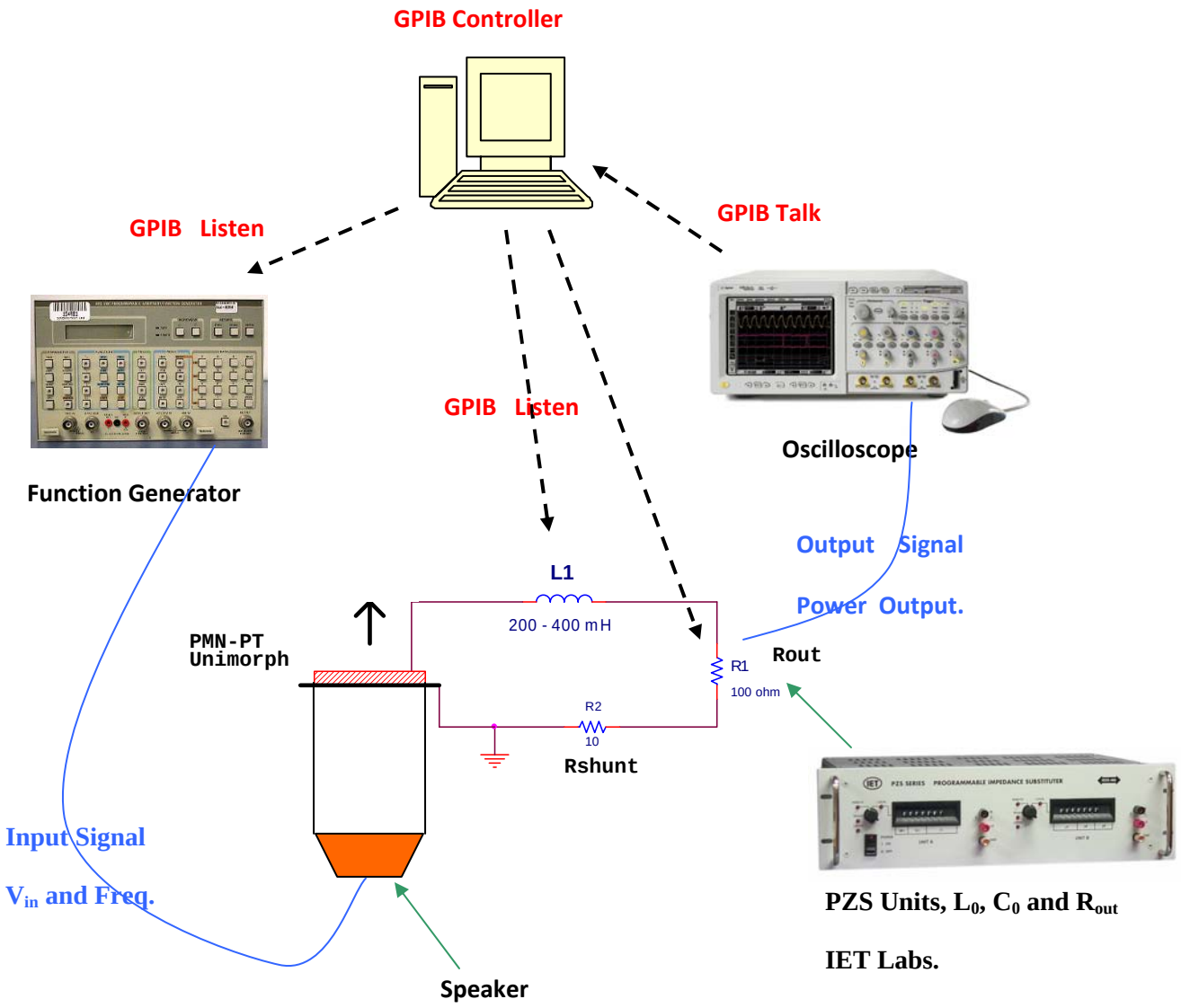

Figure A.1.1: Schematic of a dynamic control for maximizing output power from unimorphs

The program developed in LabVIEW had several modules and some of the key modules are listed below.

1) FRF_Main: This is the main block that contains all VI's and sub VI's. It basically consists of two parts. The first part of the program performs linear sweep of the frequency (both coarse and fine), then executes an algorithm do optimize the other three parameters in the circuit, based on the user defined range. It optimizes the unimorph, determining the optimal L_0, R_{OUT}, C_0 and *frequency* for a particular unimorph in the acoustic setup. After this, the program passes these parameters onto another part that does repetitive continuous sweeps over the unimorph, for a fixed number of iterations. Each time a sweep for a parameter is completed in the second part of the program, the optimal parameter is set, and the program sweeps the next parameter. This iteratively approaches the optimal parameters for the circuit. There is also a global stop command built into FRF_main that halts execution of the code via a user Boolean on the front panel. Time stamps are recorded for each step in the process in order to help improve efficiency.

2) FrequencySweep:

Inputs: Start and Stop frequencies, sweep steps, error cluster, and path

Output: Optimal frequency, error cluster

This is the VI used to run a sweep of the frequency from the start frequency to the stop frequency. It outputs an array of the output voltage of unimorph vs. the frequency and determines the optimal frequency. It is used twice in FRF_main, once for a coarse sweep, and once for a fine sweep. The VI is shown in Figure A1.2.

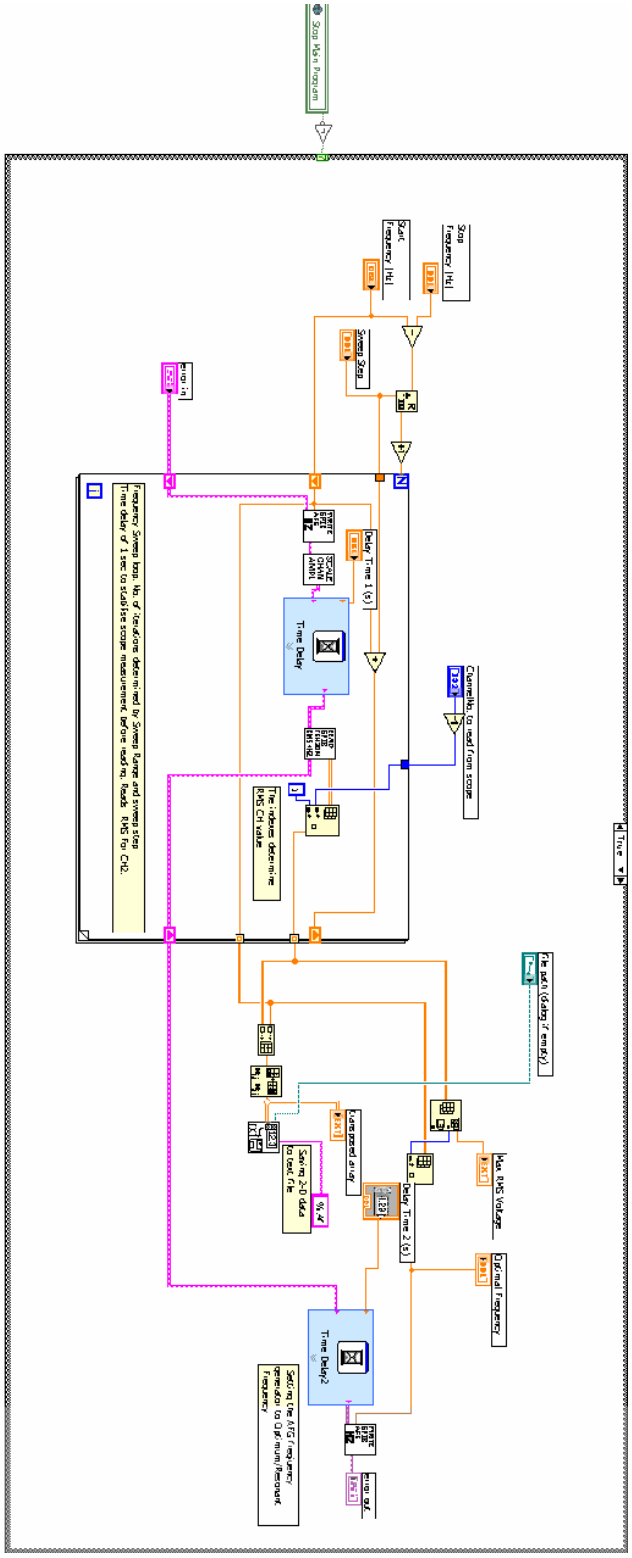

Figure A.1.2: Frequency sweep VI for determining optimal frequency

3) SetAFGHz, Set_IET_PCS_nF, Set_IET_PLS_mH, Set_IET_PRS_ohms:

These individual blocks of VI's set the frequency, capacitance, inductance and output resistance for the output circuits respectively. They are called after the execution of the optimization routine and individual values are input-ted to the circuit parameters.

APPENDIX – 2

SPECIFICATION SHEETS

A.2.1 JBL – 2426H Speaker

Specifications:

Throat Diameter:	25 mm (1 in)
Nominal Impedance:	2426H - 8 ohms 2426J - 16 ohms
Minimum Impedance:	5 ohms (H), 9 ohms (J) @ 5 kHz
D.C. Resistance:	3.3 ohms (H), 6.5 ohms (J) ± 10% @ 25°C
Power Capacity[1]:	70 W continuous program above 800 Hz 100 W continuous Program above 1.2 kHz
Sensitivity:	107 dB SPL, 1 W @ 1 m, JBL 2344A horn[2] 110 dB SPL, 1 W @ 1 m, JBL 2370A horn[2] 117 dB SPL, 1 mW on plane wave tubes
Nominal Efficiency:	25% (800 Hz to 2.5 kHz)
Frequency Range:	500 Hz to 20 kHz
Recommended Crossover[4]:	800 Hz or higher, 12 dB/octave slope minimun
Diaphragm:	0.05 mm (0.002 in) pure titanium
Voice Coil Diameter:	44 mm (1¾ in)
Voice Coil Material:	Edgewound aluminum ribbon
Flux Density:	1.8 T (18,000 gauss)
Bl Factor:	6.3 N/A(H) 9.3 N/A (J)
Positive voltage to black terminal gives diaphragm motion toward phasing plug	
MOUNTING INFORMATION:	
Mounting:	Three ¼-20 threaded holes, 120° apart on 57.2 mm (2¼ in) diameter Front snout may be removed (unscrewed) to expose standard 1 3/8 in -18 screw threads
Dimensions:	149 mm (5 7/8 in) diameter 104 mm (4 1/8 in) depth
Net Weight:	4.3 kg (9½ lb)

Response on Plane-Wave Terminated Tube

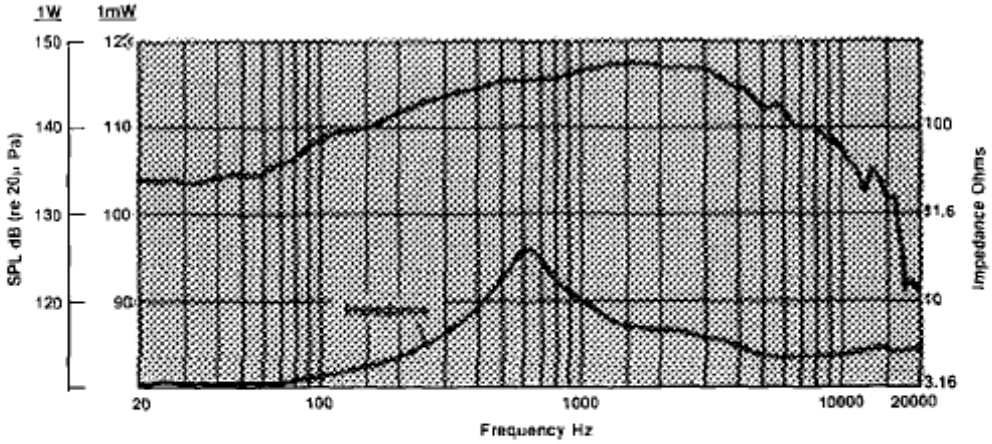

Frequency response and impedance modulus of Model 2426H coupled to a 25 mm (1 in) diameter terminated plane-wave tube. This is the power response of the transducer, and is the frequent) response that will be obtained on a true full-bandwidth constant-directivity horn design, such as JBL s 2360 series of Constant Coverage Bi-Radial®Horns.

A.2.2 H20E Epoxy from EpoTek

(To be used as a guideline only)

NUMBER OF COMPONENTS ..... Two

MIXING RATIO PARTS BY WEIGHT

- Part "A" (epoxy resin and silver powder) 1
- Part "B" (hardener and silver powder) 1
- NOTE: Mix contents of each container (A and B) thoroughly before mixing the two together.

CURE SCHEDULE (minimum)

- 175°C ..... 45 seconds
- 150°C ..... 5 minutes
- 120°C ..... 15 minutes
- 80°C ..... 90 minutes

PHYSICAL PROPERTIES

- Color ..... Bright Silver
- Consistency ..... Smooth, thixotropic paste
- Specific Gravity
  - Part "A" 2.03
  - Part "B" 3.07
- Viscosity (@ 100 rpm/23°C) ..... 2,200 - 3,200 cPs
- Glass Transition Temp. (Tg) ..... > 80°C
  - (cured 150°C/1 hour) ..... typically 100°C
- Coefficient of Thermal Expansion (CTE)
  - Below Tg ..... 31×10^{-6} in/in/°C
  - Above Tg ..... 120×10^{-6} in/in/°C
- Lap Shear Strength ..... 1,500 psi
- Die Shear Strength ..... > 10 Kg/ 3,400 psi
- Degradation Temperature (TGA) ..... 410°C
- Weight Loss @ 200°C 0.16%
- Operating Temperature
  - Continuous ..... 200°C
- Storage Modulus ..... 750,000 psi
- Volume Resistivity ..... < 0.0004 ohm-cm
- Thermal Resistance: (Junction to Case)
  - TO-18 package with nickel-gold metallized 20 x 20 mil chips and bonded with EPO-TEK H20E (2 mils thick)
  - EPO-TEK H20E ..... 6.7 to 7.0°C/watt

THERMAL CONDUCTIVITY ..... 29 W/m°K

Based on Thermal Resistance Data: $R = L \times K^{-1} \times A^{-1}$

SCHOTTKY DIODE

INITIAL	2 WEEKS @ 200°C
C_j 1pF (typical)	
V_b 5V @ 10 µa	4.8V @ 10 µa
V_f 0.4V @ 1 ma	0.32V @ 1 ma

POT LIFE ..... 4 days

SHELF LIFE

One year when stored at room temperature.

REFRIGERATION NOT REQUIRED

A.2.3 Programmable Decade Box from IET Labs

Resistance Box: Model No. PRS 200

Capacitance Box: Model no. PCS 301

Inductance Box: Model no. PLS 400A

STANDARD MODELS

Model	PRS-200	PRS-201	PRS-200W	PRS-201W	PRS-202	PRS-202W	PRTD	PCS-300	PCS-301	PLS-400	PLS400A
Type	Resistance	Precision Resistance	Wide Range Resistance	Wide Range Precision Resistance	High Precision Resistance	Wide Range High Precision Resistance	Precision Absolute Value Resistance	Precision Capacitance	Wide Range Capacitance	Range	Inductance
Accuracy	1% +70 mΩ	0.1%+ 30 mΩ	1%+ 70 mΩ	0.1%+ 30 mΩ	0.05% + 15 mΩ (0.01% available)		.02 -.05% + 10 mΩ	4% + 5 pF	1% + 3 pF		2%
Decades	7		9		7	9	6 or more	6		4	3
Range	0 - 9,999,999 Ω		0 - 99,999,999.9 Ω		0 - 9,999,999 Ω	0 - 99,999,999.9 Ω	4-10,003.99 Ω	0 - 99,999 9 µF		0 - 9.999 H	0 - 999 mH
Resolution	1 Ω		0.1 Ω		1 Ω	0.1 Ω	0.01 or 0.001 Ω	100 pF		1 mH	1 mH
Type of Components	Resistance wire for 0.1 Ω steps and under; metal film for 1 Ω steps and over.				Resistance wire for 0.1 Ω steps and under; wirewound, sealed non-inductive resistors for 1 Ω steps and over.			100-900 pF: Mica 0.001-0.009 µF: Polystyrene 0.01-0.9 µF: Polycarbonate 1-9 µF: Polyester 10-90 µF: Polarized tantalum		Toroidal inductors See inductance Substituters (page 9) for specifications	
Max. Load*	0.5 A, 200 V (dc + ac peak), 0.2 W/step, 2 W unit, whichever applies first.*				3 A, 200 V (dc + ac peak), 0.5 W/step, 4.5W/unit, whichever applies first.*			100 V (20 V for 10-100 µF)		See page 12	
Residual Impedance	<450 mΩ See page 12		<600 mΩ		<100 mΩ	<140 mΩ typically <100 mΩ	Absolute Value	7 pF typical; higher w/ Rear Output			

* These specifications are dynamic switching limits. The maximum voltage, power, or current which may be applied at any particular resistance setting may be higher as long as the setting is unchanged, or the unit is switched dry.